D. Geophysics

Deep Drilling KTB Oberpfalz VB – Results of the Geoscientific Proceedings in the KTB-Laboratory, Depth Interval: 1709 to 2500 m

E. Huenges
Ch. Bücker
K. E. Wolter
J. Wienand
A. Rauen
E. Lippmann

KTB-Report	89-2	D1-D83	59 Abb.	Hannover 1989

Deep Drilling KTB Oberpfalz VB
Results of the Geoscientific Proceedings in the KTB-Laboratory; Depth Interval: 1709 to 2500 m

D. Geophysics

Huenges, E., Bücker, Ch., Wolter, K.E., Wienand, J., Rauen, A. & E. Lippmann *)

Contents:

*) Address of the authors: KTB-Feldlabor
D-8486 Windischeschenbach

D.1 Density

D.1.1 Introduction

The density of 726 cores was measured between 1802 and 2500 m using the Archimedies principle (BÜCKER et al., 1988). From 1709 - 1802 m the density of cuttings was determined using a pycnometer. This method was described in KTB - Report 88-6 (RAUEN et al., 1988). Figure D.1.1 shows the density data core and cuttings as a function of depth.

D.1.2 Density of cuttings

Between 1709 and 1802 m, drillhole penetrated sillimanite - biotite - gneiss. The mean density, determined from cuttings, was 2.76 ± 0.03 g/cm^3 with density variations from 2.71 g/cm^3 at 1793 m to 2.81 g/cm^3 at 1715 m.

D.1.3 Density of cores

Between 1802 and 2500 m the drillhole penetrated mostly homogeneous gneiss. The average density was 2.75 ± 0.03 g/cm^3. The minimum density of 2.61 g/cm^3 measured on a lamprophyre at 2057.55 m; and the maximum density of 2.97 g/cm^3 was determined for an amphibolite from 1819.04 m. A second lamprophyre at 2106 m also had a significanty low density. At 2315.44 m and 2342.51 m, two aplite zones with relatively low densities were identified. Below 2469 m, the lithology changes from sillimanite-biotite-gneiss to hornblende-biotite-gneiss, as can easily be seen in the density data.

D.1.4 Correlation of density data of cuttings and cores from VB1 and VB1a (1709 - 1998 m)

The densities measured on cuttings from VB1a and on cores from VB1 correlate quite well (Fig. D.1.2). However, densities of cuttings from VB1 and of core from VB1a do not correlate as well. Above 1940 m, the density of cuttings is higher than of cores. Those cuttings may be contaminated by cavings of metagabbros. Between 1940 and 1980 m there is close correlation between the densities of cores and cuttings but below 1980 m, the density of the cores declines, whereas the density of the cuttings does not show any significant trend. A possible explanation for this may be that the cuttings samples represent mixtures of material from intervals of approximately 1...3 metres depending on drilling tool.

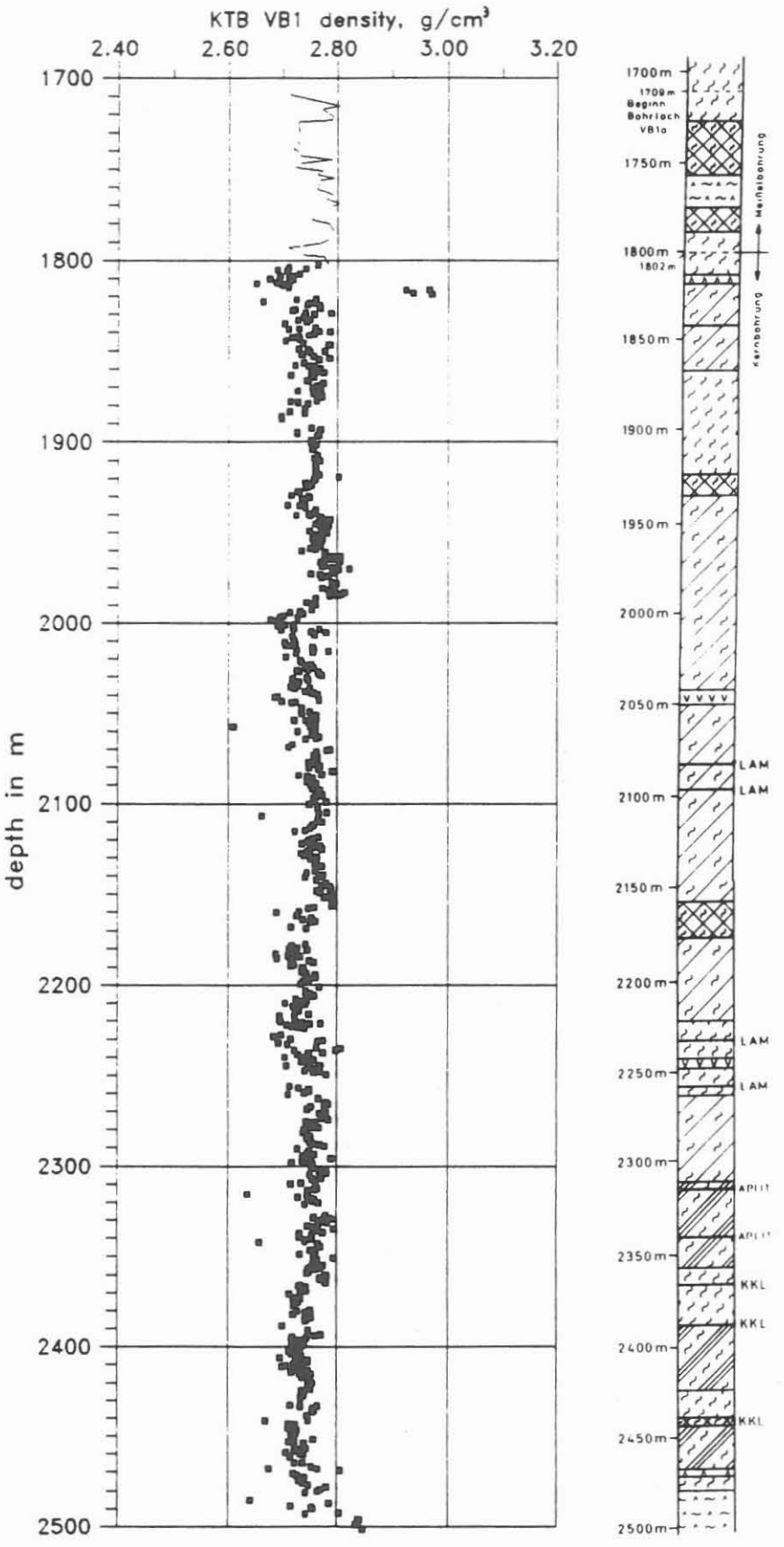

Fig. D.1.1 : Density log from 1709 to 2500 m.
Points: cores; solid line: cuttings.

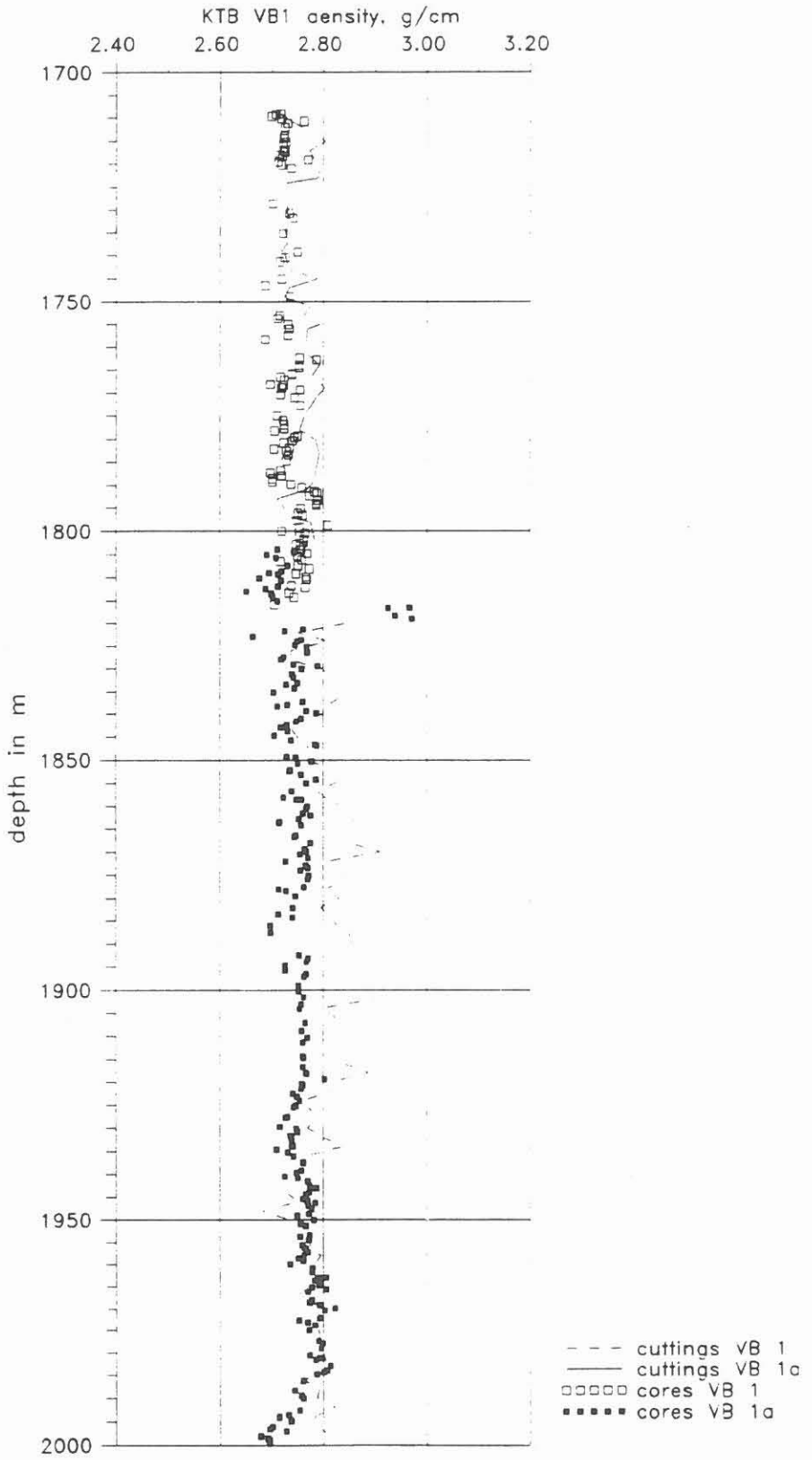

Fig. D.1.2: Correlation between the orginal hole (VB1) and the sidecrack hole (VB1a).

D.2 Natural Gamma Radiation

D.2.1 Introduction

Natural radioactivity of rocks is determined mainly by measuring the isotopes K-40, Th-232, U-238. K-40 decays into the stable isotopes Ca-40 and Ar-40. Uranium and thorium eventually decay into the stable lead isotopes, Pb-206 and Pb-208. An overview of the various decay sequences is given in Figure D.2.1.

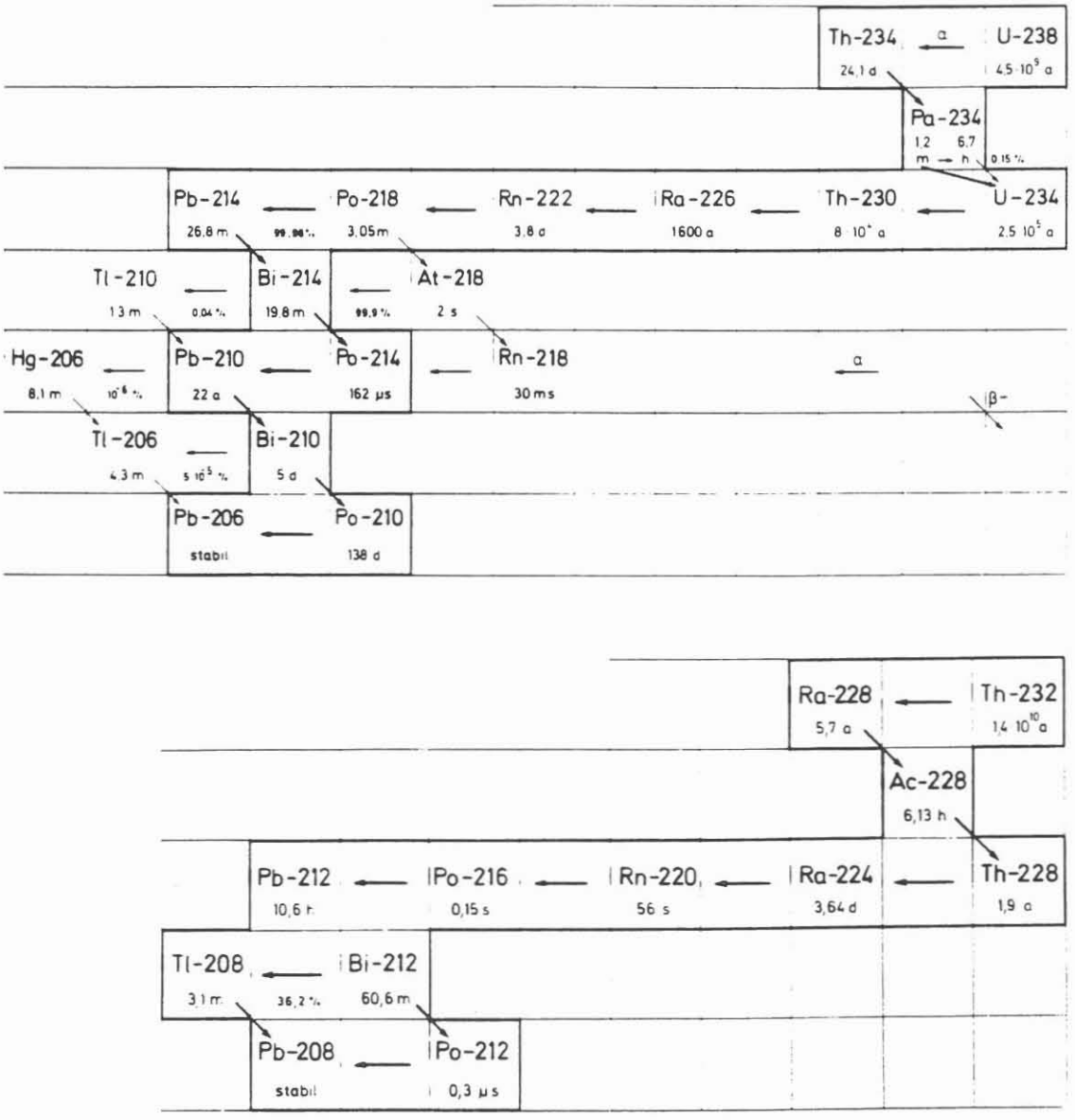

Fig. D.2.1: Uranium - Radium and Thorium - decay sequence (from: KIEFER & KOELZER, 1987).

Gamma radiation analysis allows various gamma emitters to be distinguished and the quantitative contents of potassium, uranium and thorium to be calculated. These raw data can then be used as a basis for further investigation. For example, they are used for determination of the radiogenic heat production rate, which is an important energy source for geodynamic processes, for geochemical research and for investigation on ore deposits. The heat production rate has to be taken into account for temperature predictions.

More than 99% of the heat production of crustal rocks is caused by the decay of the radioactive isotopes of potassium, uranium and thorium. The percentage of these isotopes is (HAACK, 1982):

K-40/K	0.0119	weight %
Th-232	100	weight %
U-238/U	99.29	weight %
U-235/U	0.71	weight %

From the concentrations of the radioactive elements, the specific heat production, A, of the rocks can be calculated using the following formula (RYBACH, 1976):

$$A\ [\mu W/m^3] = Rho * 0.01 * (9.52*U + 256*Th + 3.48*K) \quad [1]$$

where Rho is the density of the rock in g/cm^3; U and Th concentrations are in ppm; and the concentration of K is in %.

Mean values for the continental upper crust are (VAN SCHMUS, 1984; HAACK, 1982):

K [%]	U [ppm]	Th [ppm]	Th/U	A [$\mu W/m^3$]
2.7	2.5	10.5	≈ 4	1.6

Measurement of gamma radiation is a routine part of the logging program. It allows direct comparisons to be made between laboratory and downhole results.

D.2.2 Methods and equipment for determination of the K, U and Th contents of cuttings

Concentrations of K, U and Th are determined through spectrometry of the emitted gamma rays using a BICRON cylindrical 3"x3" NaJ scintillator. The detector is mounted inside a compartment with 10-cm-thick walls of a special low-activity lead in order to shield against natural background radiation. In addition, this compartment is lined with 2 mm of copper to absorb secondary radiation (Fig. D.2.2).

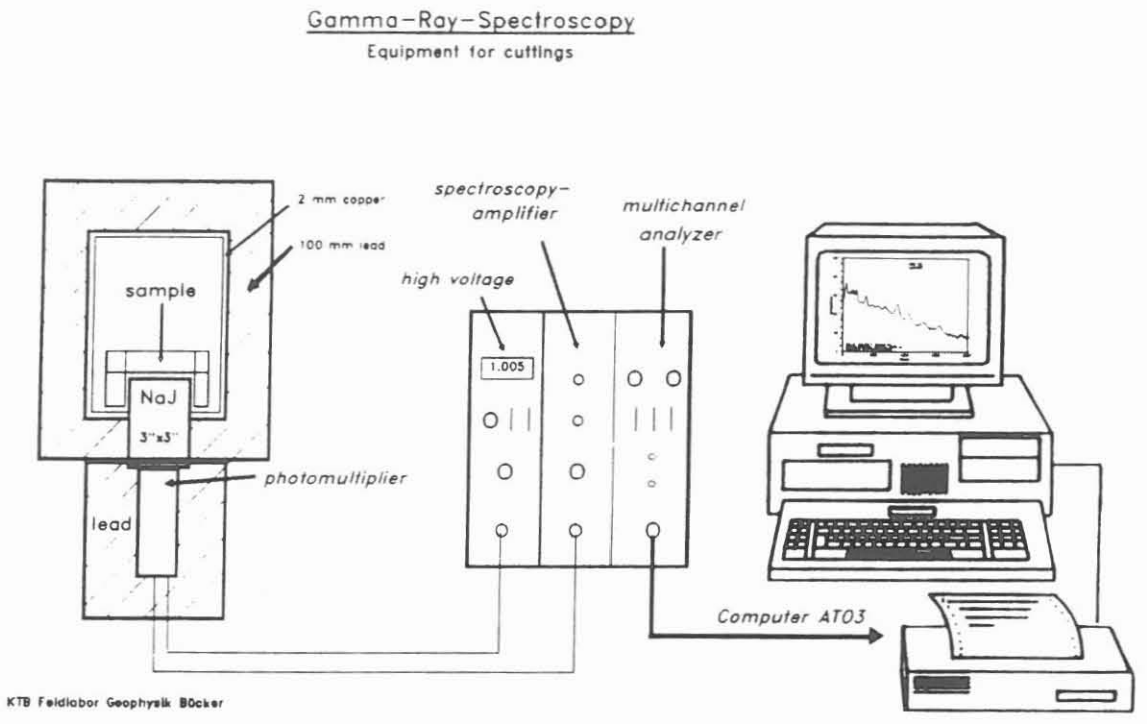

Fig. D.2.2: Sketch of the gamma spectroscopy apparatus for determination of the radioactivity of cuttings.

The samples are contained in air-tight, so-called "Marinelli-beakers". These cups, with a U-shaped cross-section, enclose the detector to a large degree, thus providing a wide angle over which the detector 'sees' the sample. The samples consist of either rinsed and dried cuttings or mud.

The gamma rays which interact with the scintillator are converted into quanta of visible light which can be detected with a photomultiplier. The photomultiplier produces voltage pulses with heights proportional to the energy of the gamma rays. These pulses are amplified and fed to an 8096-channel multichannel analyzer (MCA, made by EG&G ORTEC), segmented in four sections with 2048 channels each. With this equipment, gamma spectra in an energy range from $\approx$ 40 to 3000 keV can be recorded within a predetermined real-time interval. A software package called "MAESTRO" by EG&G ORTEC assists in displaying and storing the recorded spectra on an IBM-PC.

Figure D.2.3 is a plot of the channel number of the MCA as a function of the energy of the gamma rays. This relation is not stable over time, so energy readings are calibrated for each record. However, drift is negligible during measurement cycles from 2 hours to as much as 2 days.

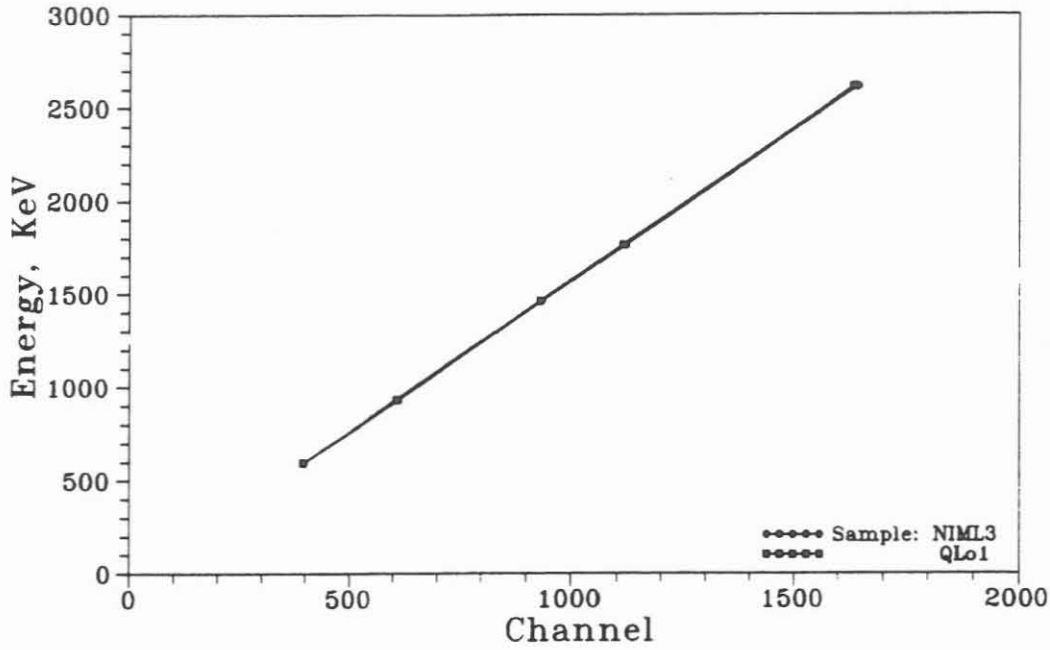

Fig. D.2.3: Relationship between energy [keV] and channel number of the multichannel analyzer measured on spectra of two calibration samples.

The efficiency and quantitative calibration of the apparatus was determined using calibration samples from the South African Bureau of Standards (SABS) and another sample with known contents of K, U, and Th. Figure D.2.4 is a plot of the spectrum of one calibration sample (NIM-L, powdered granite by SABS) and Figure D.2.5 shows the spectrum of the background radiation recorded with an empty Marinelli-beaker. Background radiation is repeatedly measured and taken into account when evaluating the spectra of the samples.

The SODIGAM program (WESTMEIER, 1988) is used to evaluate the spectra and calculate the radioactivity of particular gamma emitters. This program calculates radioactivity in Bq/kg (background radiation is accounted for) and these values are then converted into concentrations of potassium, uranium and thorium.

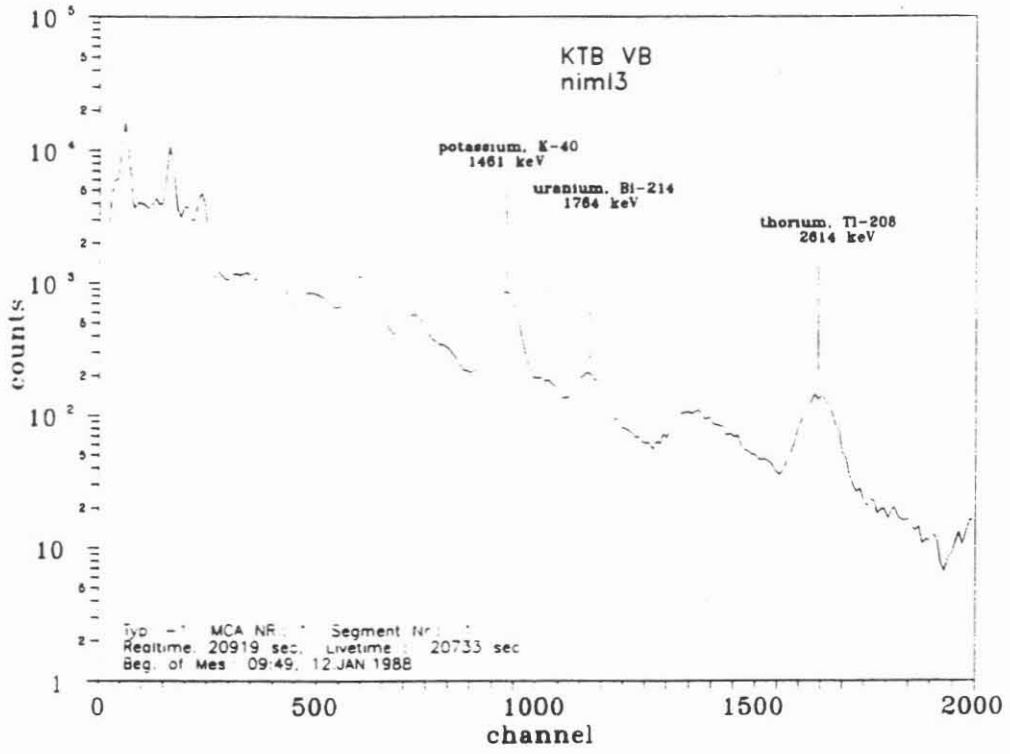

Fig. D.2.4: Gamma ray spectrum of the calibration sample NIM-L. K, U and Th peaks are marked.

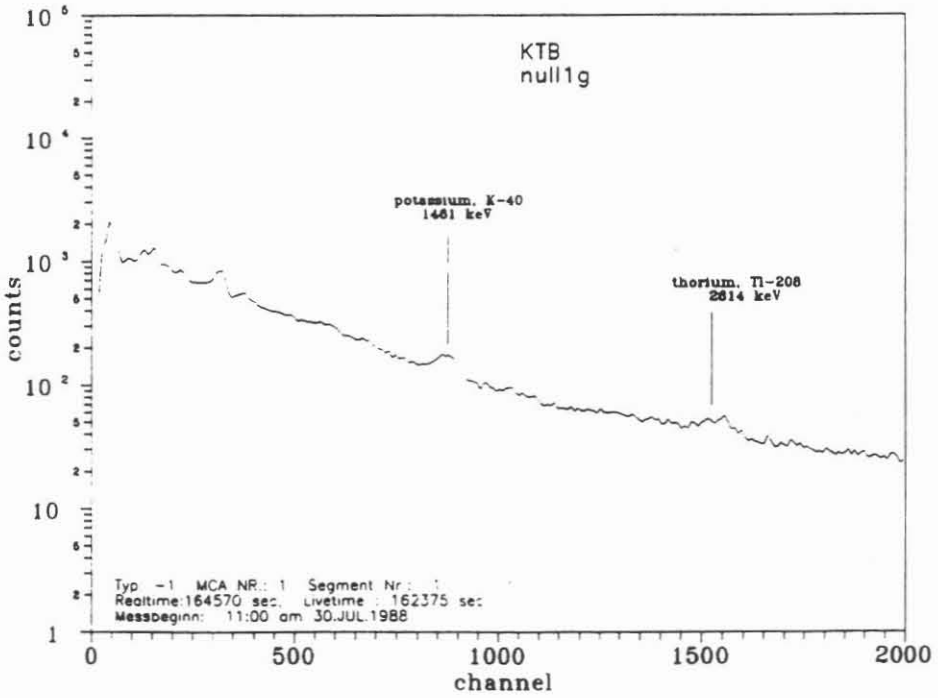

Fig. D.2.5: Spectrum of the background radiation, recorded with an empty Marinelli-beaker. The potassium peak is significant.

D.2.3 Results

Total counting rates from our spectra were plotted against depth (Fig. D.2.6) to initially compare results of gamma ray measurements of cuttings and the downhole gamma-ray log (GR). The lithological boundary between gneiss and amphibolite at 1160 m can easily be recognized and is better defined from the gamma-ray log than from the measurements on cuttings. This is probably due to the way cuttings are recovered; they represent a mixture of material from a depth interval of approximately 1...3 meters. The only core (KM 253) recovered during the directional drilling phase from 992 to 1210 m was amphibolite between 1177 and 1183 m. The radiation of the cuttings from the same interval, however, is as high as that of the gneiss penetrated between 530 and 1160 m. Therefore, we believe that these cuttings are mainly cavings from between 530 and 1160 m. This interpretation is supported by density and susceptibility measurements and petrographic examination (see RAUEN et al., 1988).

The contents of potassium, uranium and thorium in the cuttings are plotted versus depth in Figure D.2.7. The figure also shows the heat production rate versus depth, calculated according to equation [1]. The gneiss above 1160 m has an elevated content of radioactive elements: 2.2 % potassium, 3 ppm uranium and 6-12 ppm thorium. The heat production rate is also quite high due to the high radioactivity (1 to 2 $\mu W/m^3$). These values compare well with the average heat production rate of granitic rocks from the upper crust (VAN SCHMUS, 1984). The concentration of radioactive elements is distinctly lower in the amphibolite below 1160 m: 1 % potassium, < 1 ppm uranium and < 5 ppm thorium. The specific heat production is much less than 1 $\mu W/m^3$. As can be seen from equation [1], potassium makes the least contribution to the heat production rate. The large scatter of uranium and thorium concentrations is due to inhomogeneities in the drilled rocks.

We have not yet compared the gamma spectrometry measurements of cuttings with the gamma-spectrum of core 253 recovered from 1177 m because of a lack of suitable calibration cores.

Figure D.2.8 shows an example of our measurements (depth: 1152 m; lithology: gneiss; livetime: 43200 sec.). Evaluation of the designated peaks produced the following results:

sample	K [%]	U [ppm]	Th [ppm]	Th/U	A [$\mu W/m^3$]
cut1152	2.20	3.1	12.2	3.9	1.9

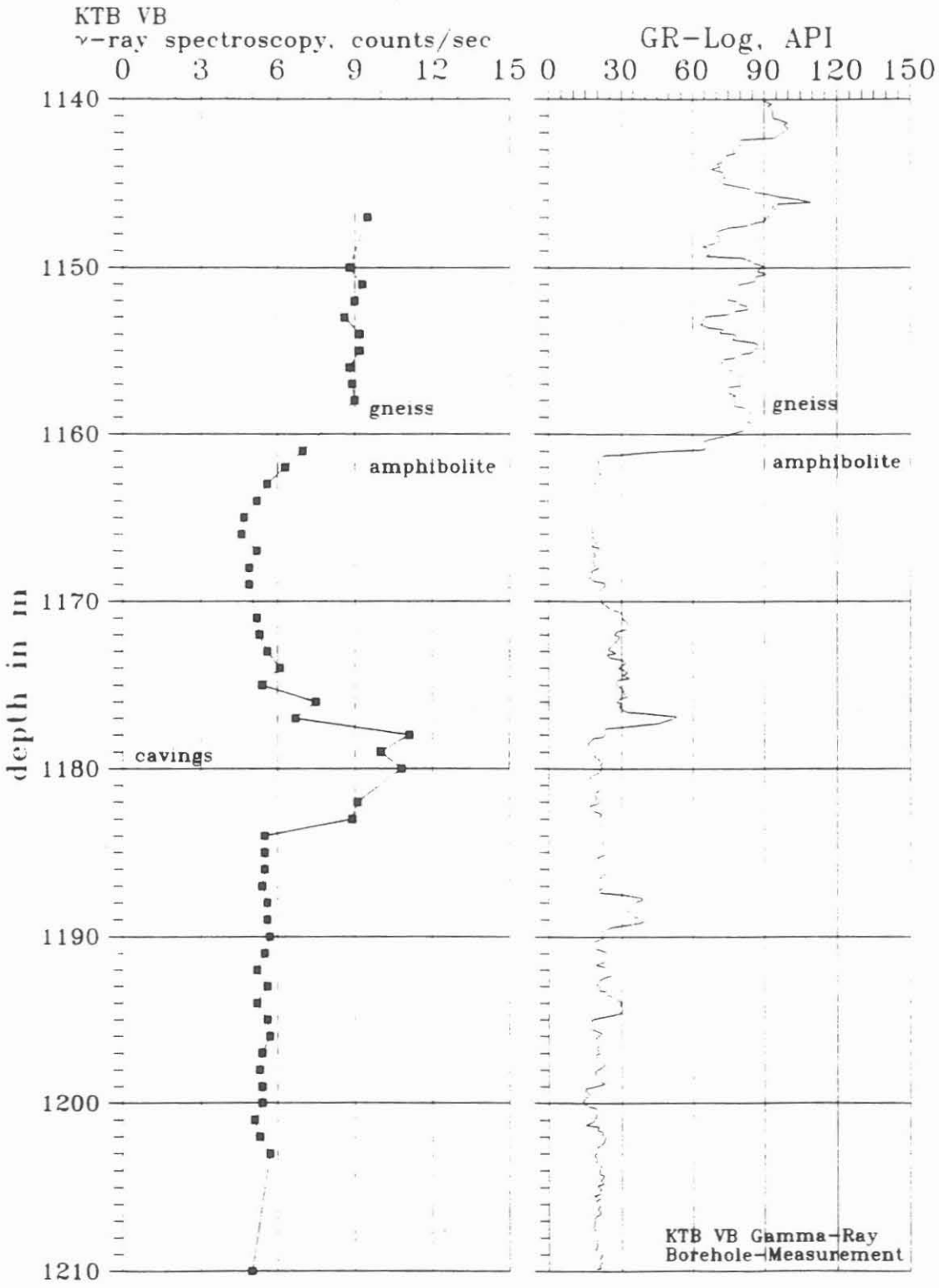

Fig. D.2.6: Left: depth log of counting rate, calculated from gamma ray spectroscopy of cuttings. Right: down hole gamma ray-log (GR).

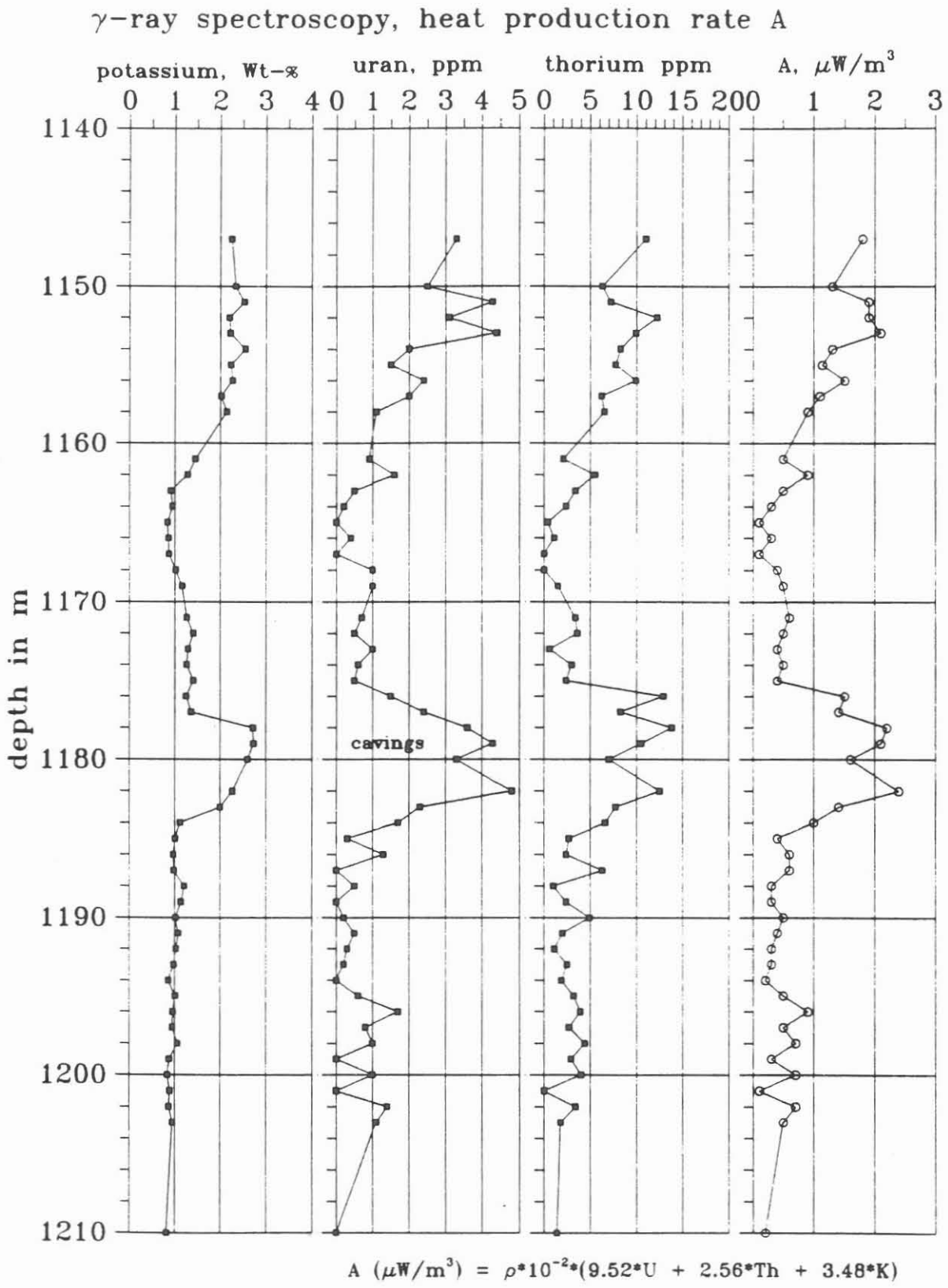

Fig. D.2.7: Gamma ray spectroscopy measurements on cuttings: contents of K, U and Th. For right column: heat production rate, calculated from the density of the cuttings with the formula of RYBACH (1976).

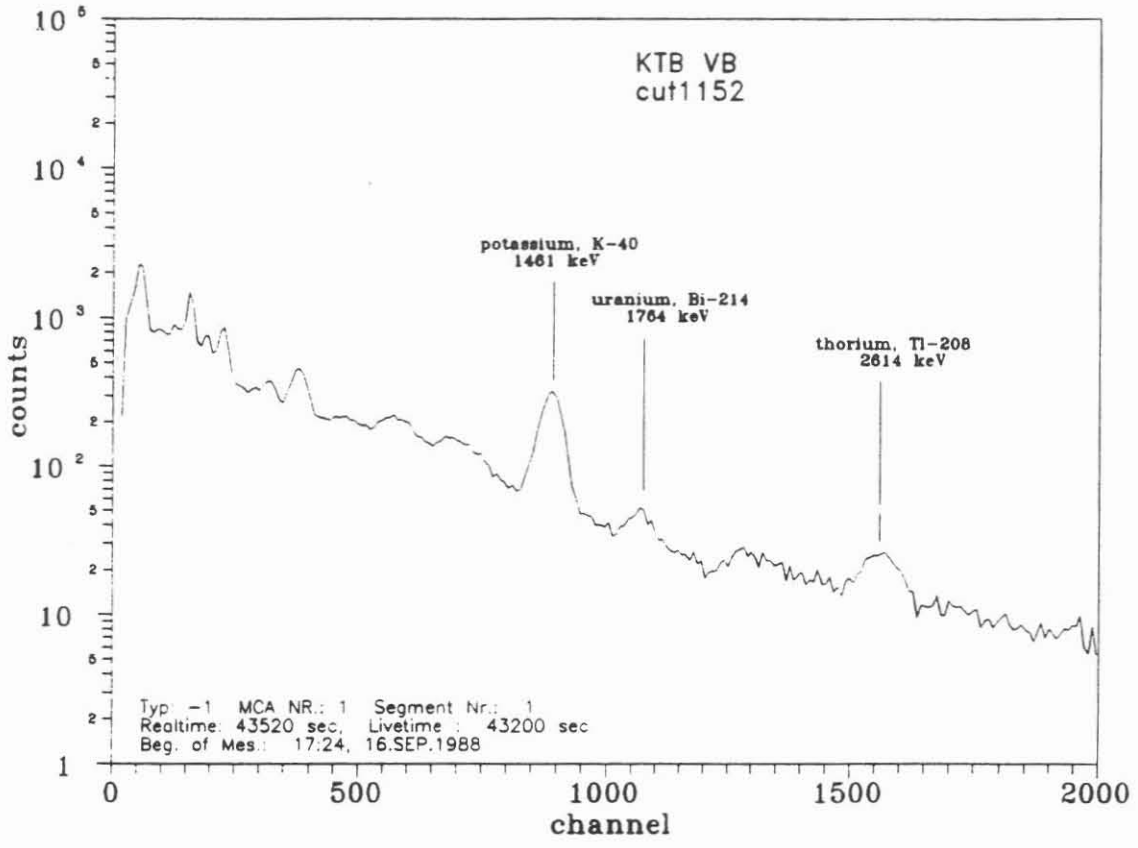

Fig. D.2.8: Gamma ray spectrum of a cuttings sample from 1152 m.

From 1177 to 1183 m, most cuttings were identified as cavings. In Figure D.2.7, this depth range can be easily recognized by high concentrations of radioactive elements. Locally, there are even higher concentrations than those determined for the gneiss above 1160 m. We suspect that most of these cavings originated from cataclastic zones with relatively high contents of radioactive elements and low mechanical stability.

Thorium and uranium concentrations may show strong local variations, but the ratio Th/U is commonly constant (see RYBACH, 1973). Average Th/U-ratios are in the range of 3 to 4 in the investigated samples (Fig. D.2.9). With increasing uranium concentrations, a weak trend toward a decreasing Th/U ratio can be recognized. Further investigation will shed more light on this phenomenon, which was previously reported by RYBACH (1973). Presently, no unambiguous conclusions can be drawn due to the small number of measurements that have been made.

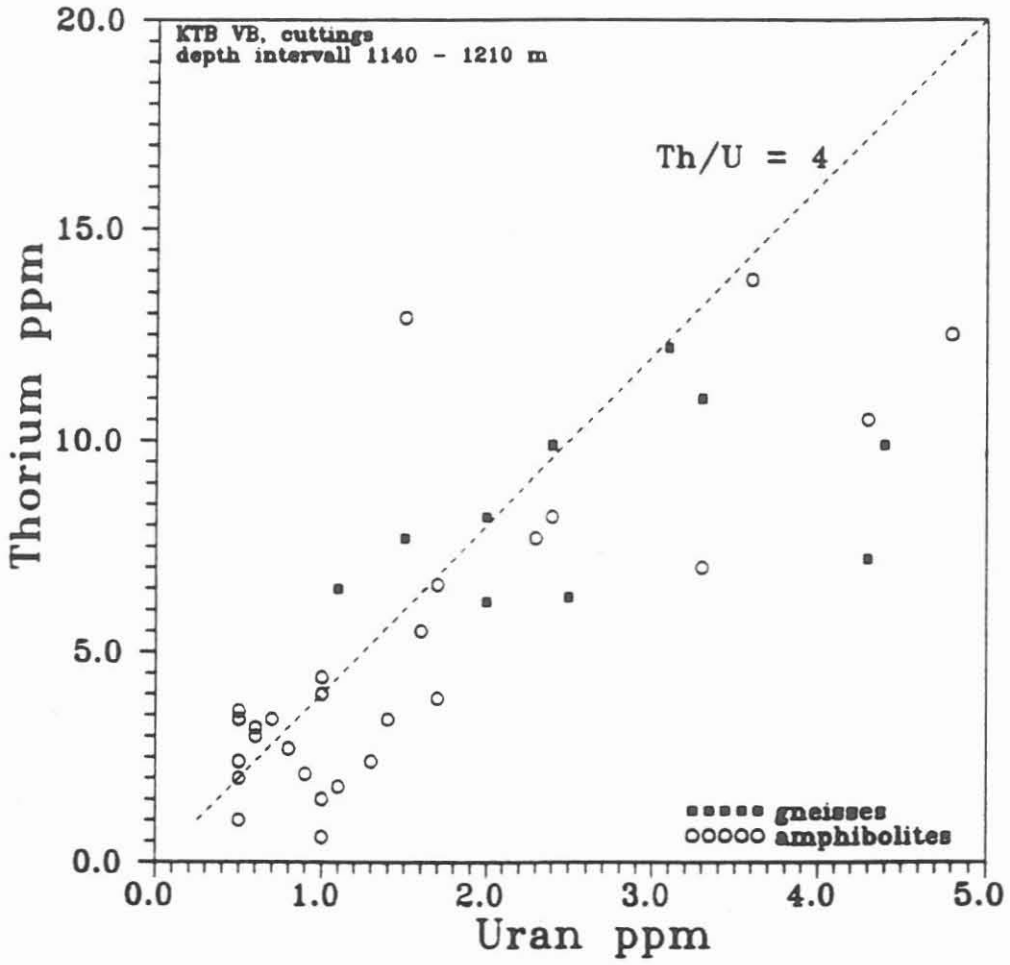

Fig. D.2.9: Th/U - ratios of cuttings from 1140 - 1210 m. Dashed line: Th/U - ratio 4. Circles: amphibolites. Squares: gneisses.

A comparison between the laboratory gamma-spectroscopy and the logging results of the NGS (Natural Gamma Spectrometer, see DRAXLER & HAENEL, 1988a, p. 51) shows close agreement for uranium and thorium. Potassium concentrations, however, differ by as much as 0.5 % with the higher readings being from the NGS. This difference is especially marked in the gneiss above 1160 m (Fig. D.2.10).

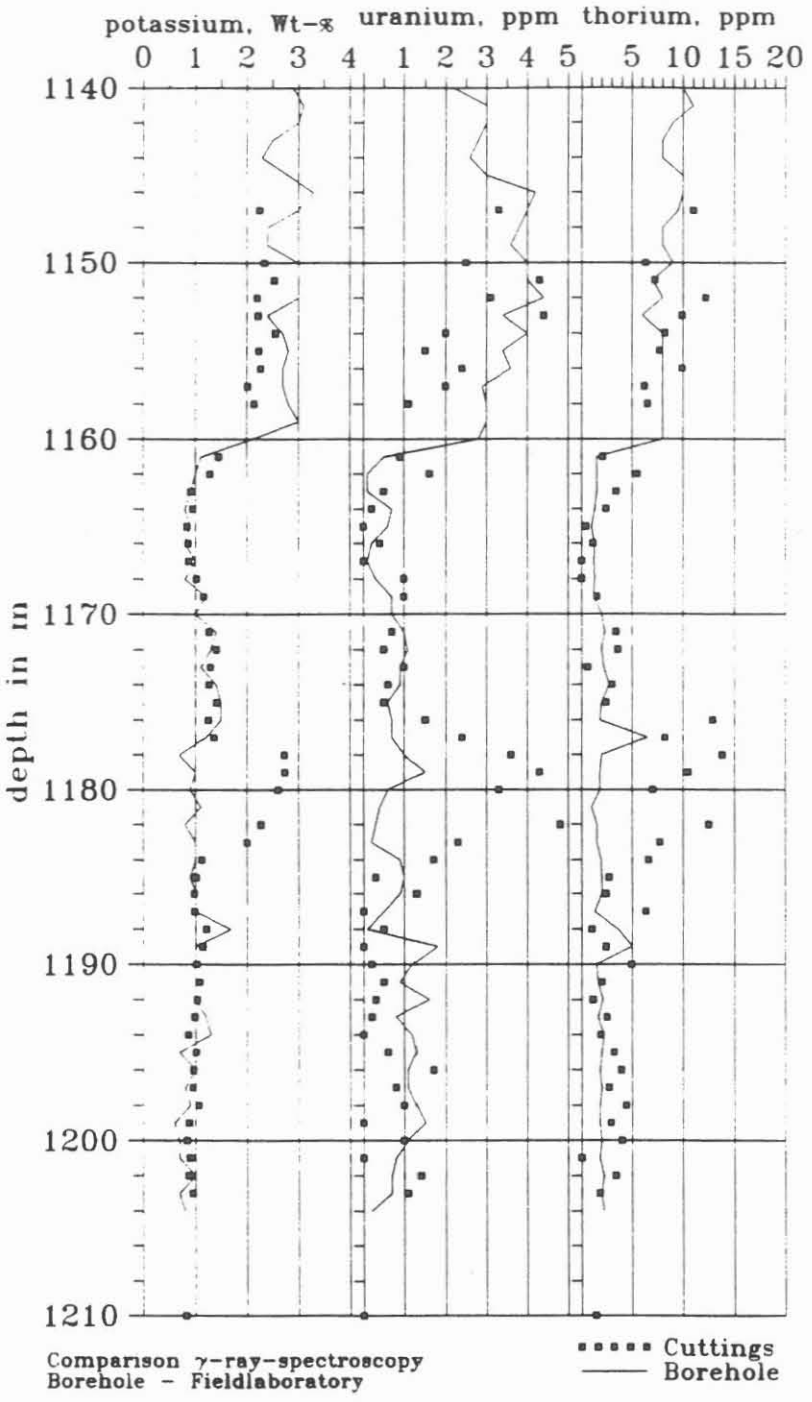

Fig. D.2.10: Comparison of potassium-, uranium- and thorium-contents determined with gamma ray spectroscopy on cuttings in the laboratory (squares) and NGS logging in the borehole (full line).There is a close agreement between both methods below 1160 m. From 1177 to 1183 m the cuttings were contaminated by cavings.

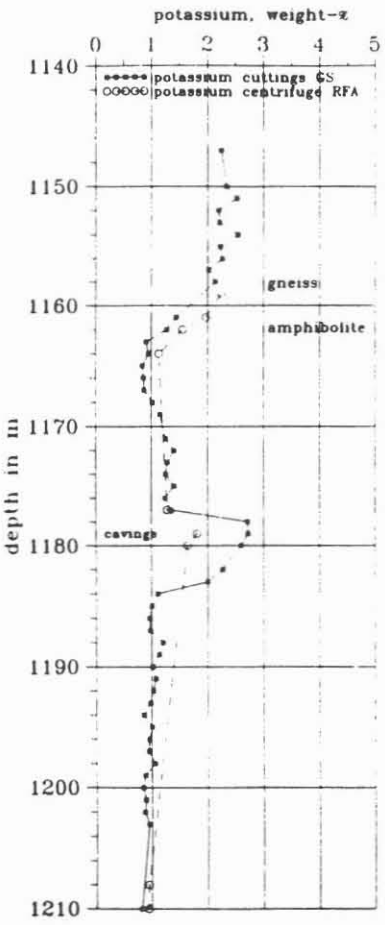

The comparison of the concentrations of potassium determined for material from the centrifuge by our X-ray flourescence group and for results of laboratory gamma-spectroscopy for cuttings shows a close agreement (Fig. D.2.11). Figure D.2.11 also shows a depth difference between cuttings and the relatively fine-grained fraction obtained from the centrifuge. If the gamma spectrometry results are shifted down 1.5 meters, both methods for determination of potassium content yield nearly identical concentrations. A possible explanation for this observation may be sampling procedures for cuttings and material from the centrifuge: both are taken at the same time, but at different places within the circulatory system of the mud.

Fig. D.2.11: Comparison of potassium-concentrations of cuttings, determined with gamma ray spectroscopy (squares) and X-ray flourescence (RFA, circles) (see STROH et al., 1988).

Elevated concentrations of potassium have been mentioned by DRAXLER & HAENEL (1988b). We think that these high concentrations are due to loading of the mud with K_2O. Gamma-spectroscopy determinations of the potassium content of the mud yielded a maximum concentration of 0.2 % (Fig. D.2.12). Thus, loading of the mud with K_2O cannot alone explain the higher potassium values from the NGS. The difference may be the result of a geometric effect: radioactive elements in the mud are closer to the scintillator of the logging tool than to the walls of the well and so they have a disproportionate effect on the NGS results. However, potassium contents determined by NGS and by laboratory measurements show close agreement in the amphibolite and differ only in the gneiss. So we suspect that even with static mud in the hole, there are reactions between mud and the formation; the mud gains potassium from exposed K-rich formations in the hole. The NGS measurement or its evaluation cannot presently be excluded as a reason for the different values obtained for potassium concentrations.

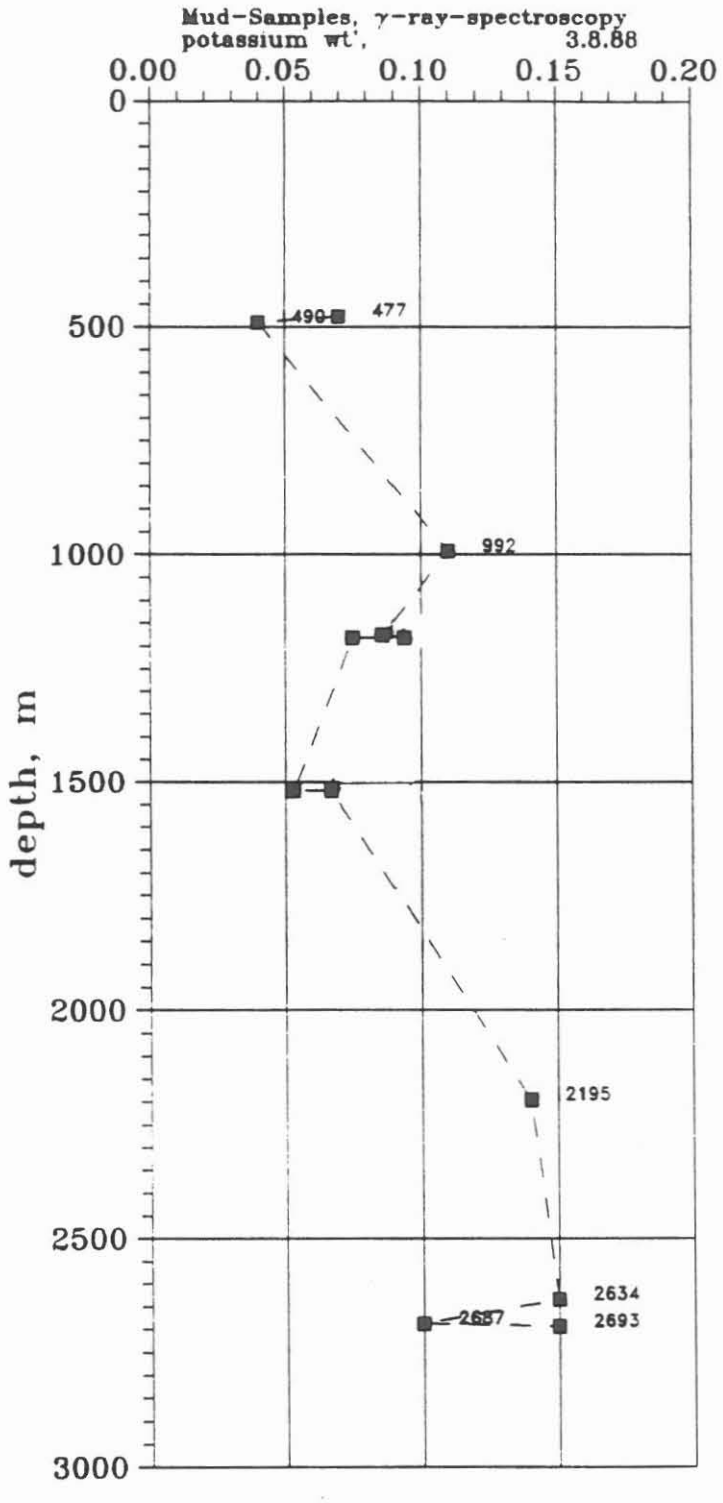

Fig. D.2.12: Potassium-concentrations of mud, sampled at different times and depths. Determination of the concentrations was done with gamma spectroscopy. Loading of the mud with K from 490 m can be recognized.

D.3 Sonic Velocity

D.3.1 Introduction

No coring was done for 34 days due to directional drilling, cementing and sidetracking. Coring resumed at 1802 m, and from there to 2500 m, 485 p-wave velocity readings were taken perpendicular to the axis of the samples. In May 1988, new equipment introduced into our routine work enabled determination of p- and s-wave velocities parallel to the core axis.

D.3.2 Methods and Equipment

Sonic velocity measurements were initially made using a commercial sonic measurement instrument (for description, see BÜCKER et al., 1988). Although the results were quite reliable, there were some drawbacks. Firstly, sensitivity and power output were too low in some cases. Particularly with badly fractured samples, it was often not possible to obtain good signals for reliable velocity measurements over a full rotation of the core. Secondly, determination of sonic velocities parallel to the axis of the samples was very time consuming, making routine measurements impossible. Finally, we wanted more information on the mechanical properties of the rocks than mere velocities (e.g., Q-values). Therefore, a new apparatus for sonic velocity measurement that satisfies all of these drawbacks was developed at the 'Institut für Allgemeine und Angewandte Geophysik' of the University of Munich.

With the new apparatus, sensitivity was increased by 32-fold stacking of consecutive signals. This improved the signal-to-noise ratio at the receiver side, and sufficient output power is provided by a separate power amplifier, delivering 200 Volts within 0.5 µsec to the sound-emitter.

To reduce time consuming preparation for determining velocities parallel to the core axis (i.e. sawing the ends of the samples), a method was adapted that permits measurement of p- and s-wave velocities with refracted waves. This method is known from seismic field work as the CMP (Common-Mid-Point) method (Fig. D.3.1). Although it may seem difficult to conduct s-wave measurements with the arrangement shown in Fig. D.3.1 (because there is water between the sensors and the sample!), s-waves in fact are the dominant phases in our signals because p- to s-conversion is very efficient at the boundary between water and the sample. The CMP-method also eliminates the need to determine absolute dimensions of the sample and absolute distances between the sensors or absolute travel times. Only the increase in travel time versus the increase in distance between emitter and receiver must be measured.

Finally, a fast digital recorder (100 nsec sampling interval, 10 bit resolution) is now used, thus allowing storage of the recorded signals for further analysis.

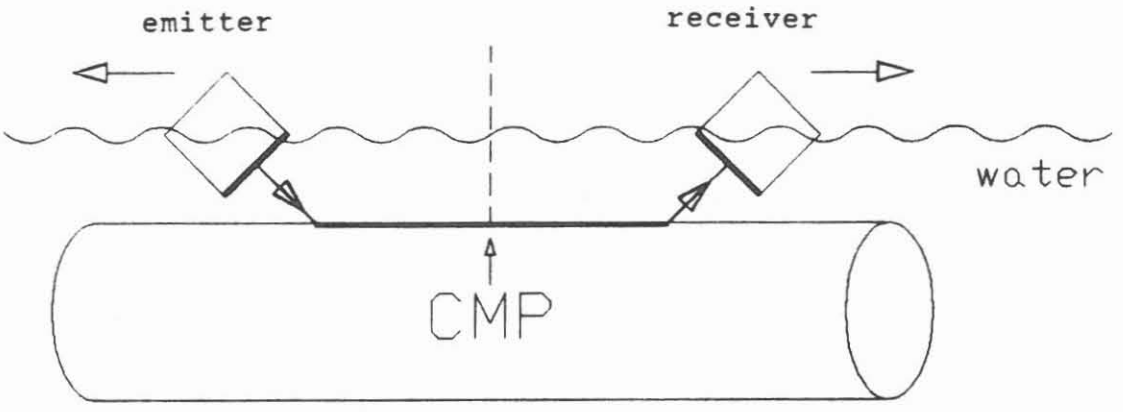

Fig. D.3.1: Arrangement of the piezo-electric sound transducers for determination of p- and s-wave velocities parallel to the core axis. S-waves are very efficiently generated at the boundary between water and the sample.

D.3.3 Results

Figures D.3.2.a and b show the depth log of maximum and azimuthally averaged radial (i.e. perpendicular to the core axis) p-wave velocities. Because of the rather homogeneous lithology, these logs do not exhibit any exciting features. Even the change in lithology at 2469 m is not apparent in our velocity log; gneiss recovered between 2469 and 2500 m is distinguished from the gneiss previously recovered by the high garnet content (the density log clearly indicated that change, see Fig. D.1.1).

We also calculated the anisotropy coefficient of the p-wave velocities, A, (where

$$A = (Vp_{max} - Vp_{min})/Vp_{average}$$

(see Fig. D.3.3). The results of that calculation are plotted only if the angle between the directions where maximum and minimum velocities were determined is in the range of 90 ± 20 degrees. This condition excludes results of measurements on badly fractured samples. On such samples, we could often conduct only a few measurements approximately parallel to the fractures, and anisotropy coefficients calculated from velocities obtained on such samples would be meaningless. So figure D.3.3 mainly illustrates the change in equipment used. There is a higher density of data points below 2250 m, where the stronger power amplifier and sensi-

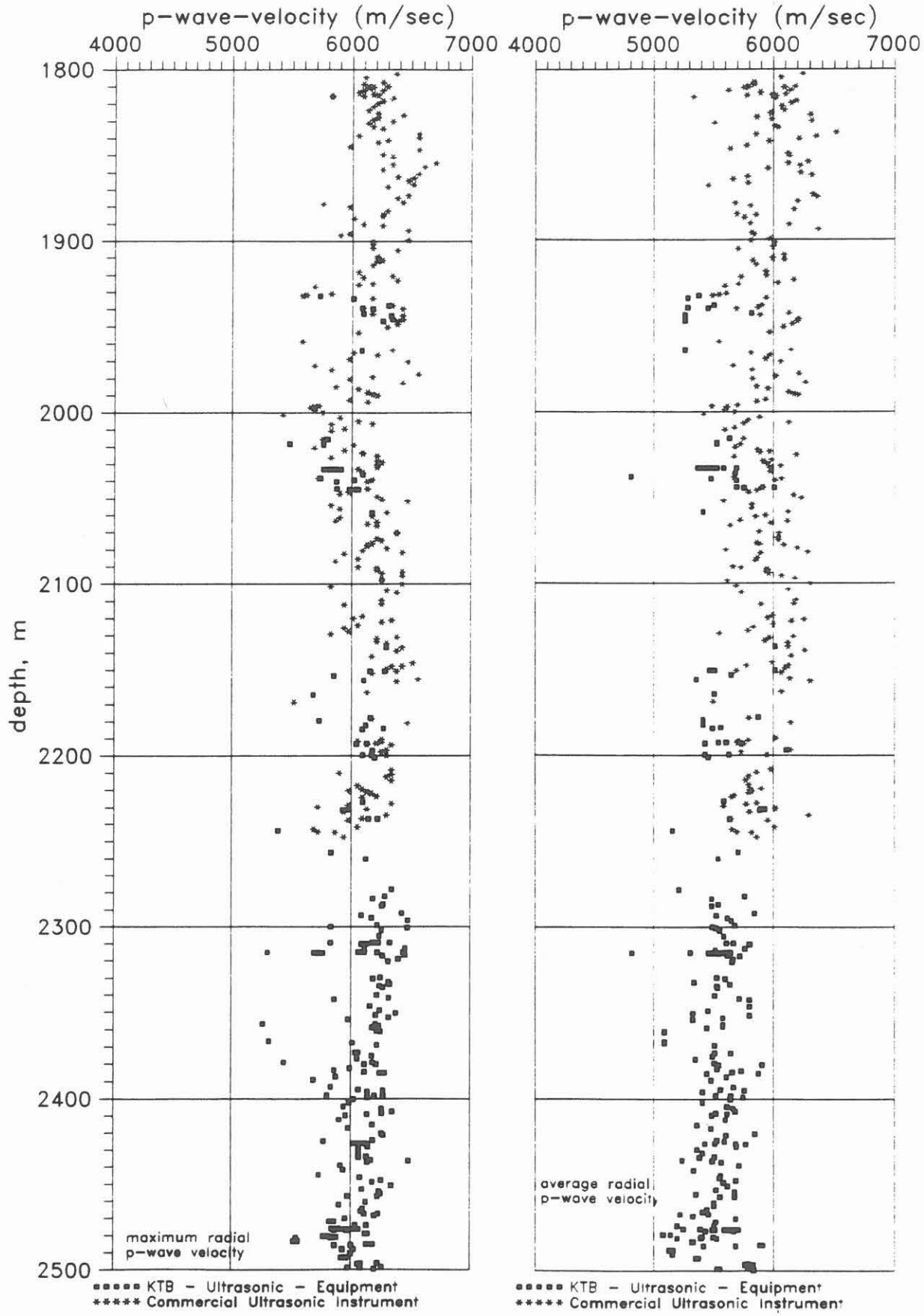

Fig. D.3.2.a: Maximum radial p-wave velocity

Fig. D.3.2.b: Average radial p-wave velocity

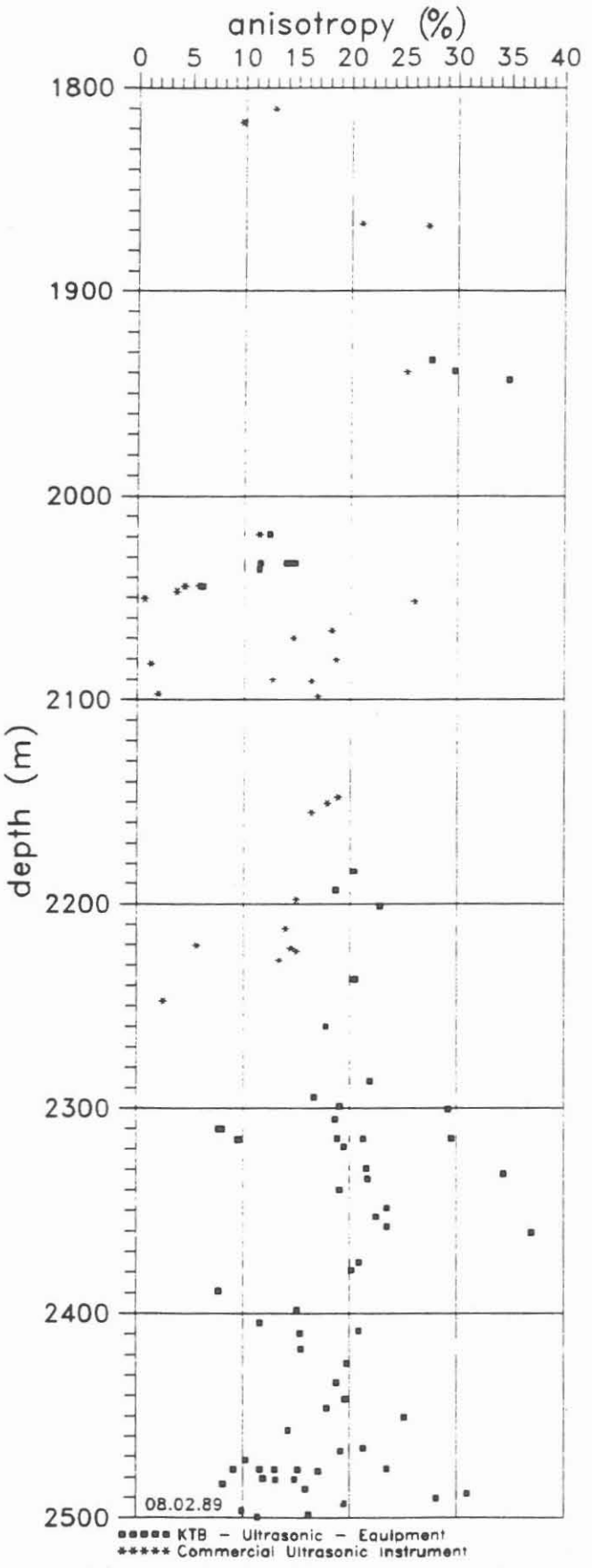

Fig. D.3.3: Anisotropy of p-wave velocity

tive receiver of the Munich ultrasonics machine was put into use allowing us to obtain good signals on samples where formerly we had only noise.

Figures D.3.4.a and b show the distribution of our data. The p-wave velocities determined between 1802 and 2500 m are grouped closely around 6100 m/sec (maximum p-wave velocities) with a standard deviation of only 230 m/sec. Average velocities have a mean value of 5700 m/sec and a standard deviation of 290 m/sec. Figure D.3.5 shows an attempt to correlate densities with the maximum velocities. A disappointing correlation coefficient of only 0.33 was determined.

The best fit is: Vp = - 524 + 2416 * density (m/sec).

The poor correlation is likely due to several factors, the most important being the uniform lithology in which observed density variations were very small (standard deviation of the density log is only 0.032 g/cm^3).

Figure D.3.6 shows an example of the time dependence of the p-wave velocities of a fine-grained gneiss. This plot confirms what we suspected earlier: the maximum p-wave velocities are relatively stable, whereas the minimum values strongly depend on time and saturation of the samples with water. This observation correlates well with the relaxation experiment conducted in the field lab (see section D.7).

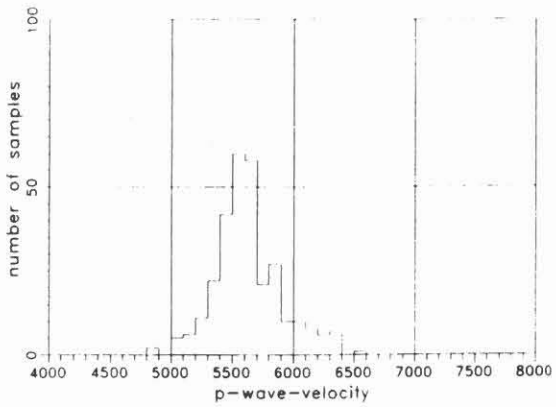

Fig. D.3.4.a: Frequency of average p-wave veolcities from 1800 - 2500 m.

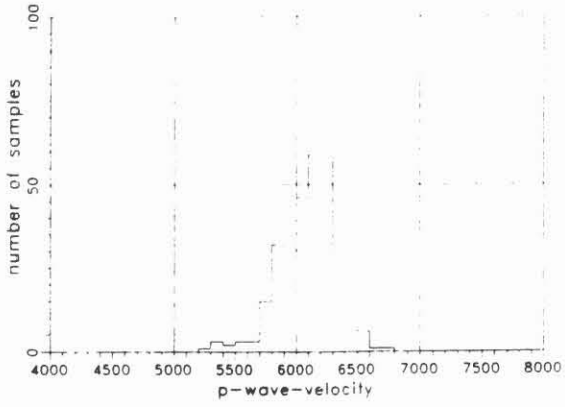

Fig. D.3.4.b: Frequency of maximum p-wave velocities from 1800 - 2500 m.

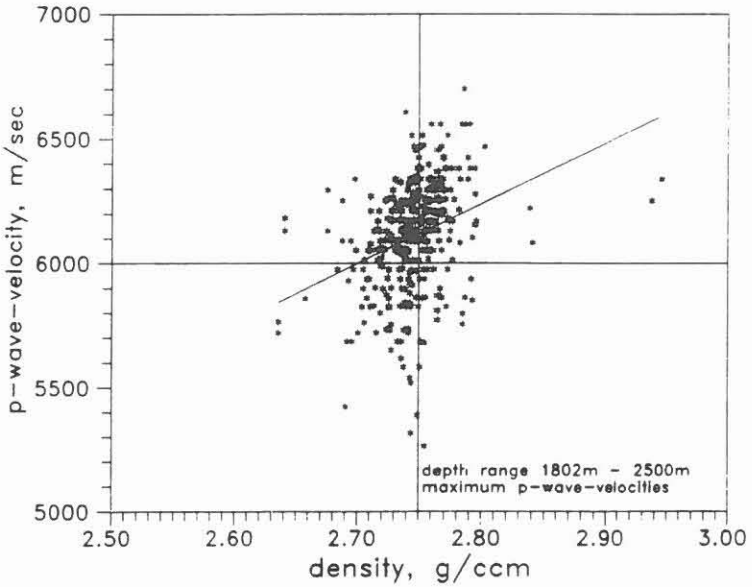

Fig. D.3.5: Plot of maximum p-wave velocities versus density.

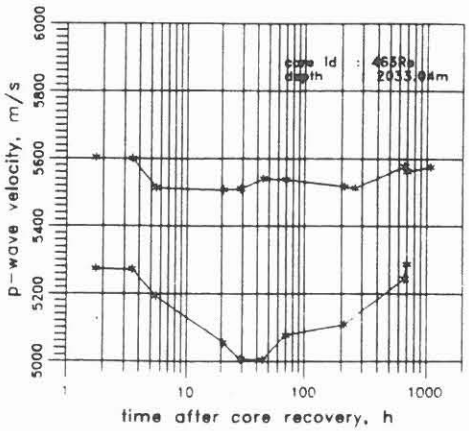

Fig. D.3.6: P-wave velocity as a function of time after core recovery. The high velocity was measured ± parallel to foliation and the low velocity perpendicular to foliation.

The opening of microfractures parallel to the foliation of the cores seems to have a marked effect on the mechanical properties of the rocks, reducing sound velocity perpendicular to foliation, and after a certain time, the microfractures become water saturated, thereby increasing sound velocity to near the initial level.

Figure D.3.7 is a plot of the first results of determination of velocities parallel to the core axis. The p- to s-wave velocity ratios are approximately √3. Further analysis is presently inconclusive because of the very small data set.

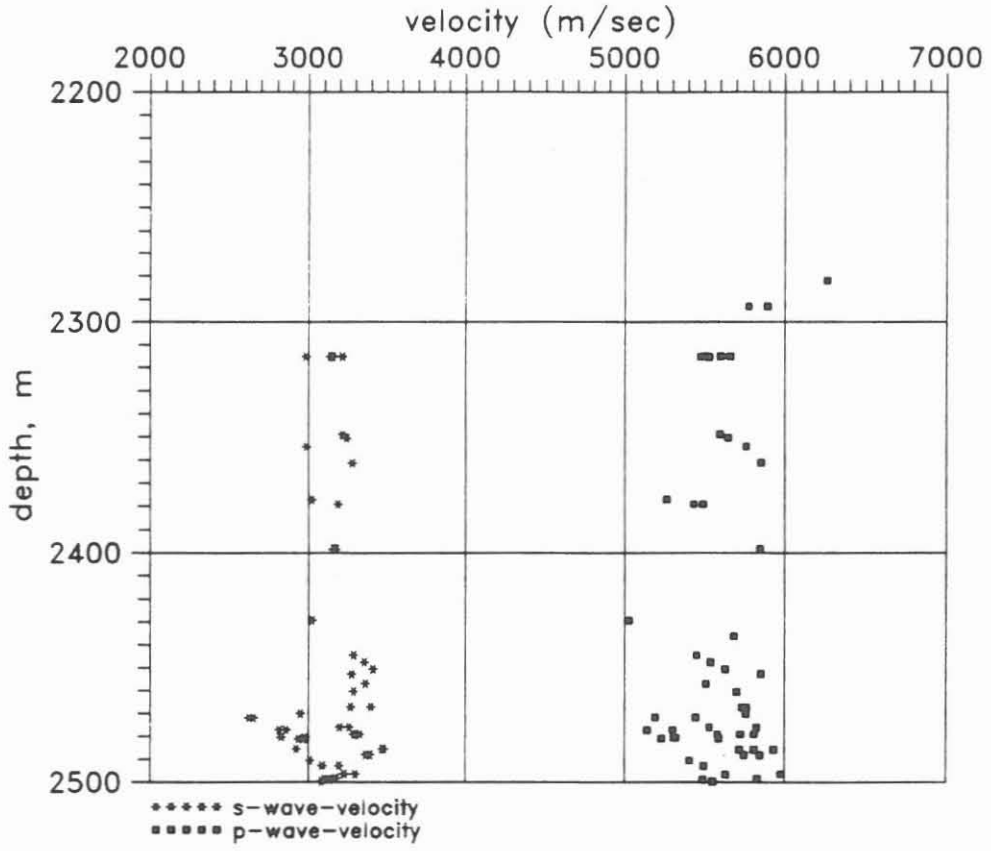

Fig. D.3.7: Results of p- and s-wave velocity measurements parallel to the core axis

The following plots (Figs. D.3.8a - d) give an overview of typical dependencies of velocity on the angle of transmission. Very few samples with anisotropies less than 10% are found between 1802 and 2500 m.

D.3.4 Correlation between the two branches of the KTB-borehole

Finally, possible correlations between the velocities measured in each of the two branches of the KTB Borehole were examined (Fig. D.3.9). Unfortunately, the overlap between

the branches is very small, the lithology is very uniform and the sampling intervals are relatively large. Thus, no firm conclusions about the depth difference of lithological units could be drawn from the velocity log.

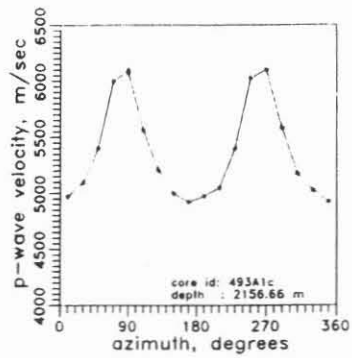

(a) Sample 493A1c from 2156.66 m

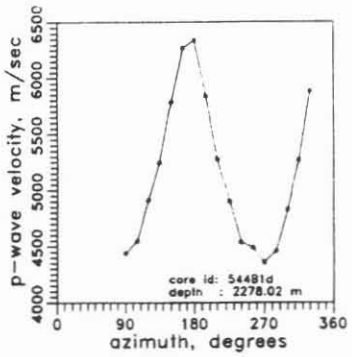

(b) Sample 5441d from 2278.02 m

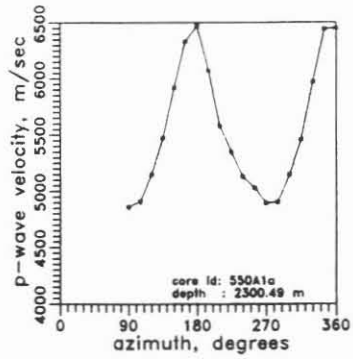

(c) Sample 550A1a from 2300.49 m

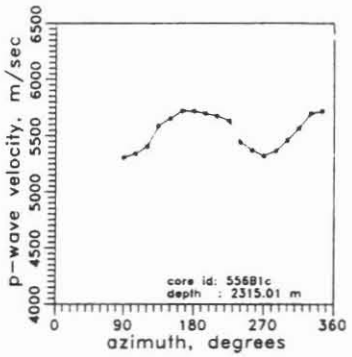

(d) Sample 556B1c from 2315.01 m

Fig. D.3.8 a-d: Typical dependencies of velocity on angle of transmission for 4 core samples.

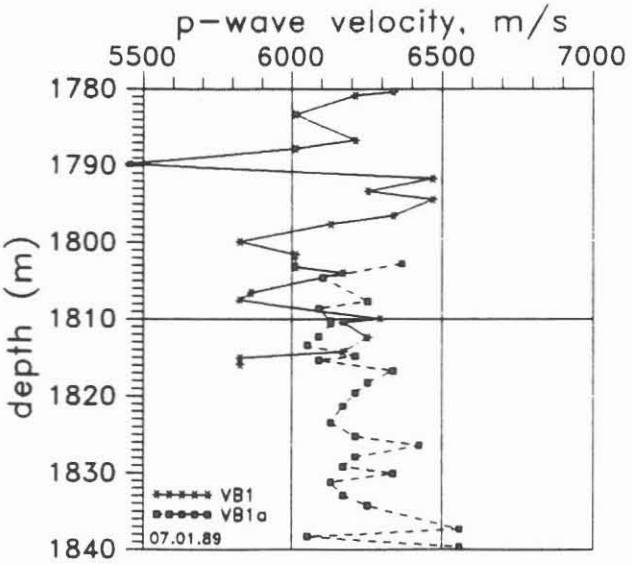

Fig. D.3.9: Results of maximum p-wave velocity investigations on cores from the two branches of the KTB-pilot-borehole.

D.4 Thermal Conductivity

D.4.1 Introduction

Thermal properties of the rocks are needed to enable interpretation of the temperature profile of the borehole. Therefore, a thermal conductivity log, at intervals of 5 to 10 m, was constructed.

The Fourier-equation [1] defines the thermal conductivity, k, as the material property which causes the heat flow, q, at a temperature gradient, grad T:

$$q = \underline{\underline{k}} * \text{grad } T \qquad [1]$$

In general, the thermal conductivity of rocks is anisotropic. Thermal conductivity of foliated crystalline rocks can be considered transversely isotropic with the main axis of thermal conductivity ($k_{11} = k_{22}$) in the plane of foliation and the smaller value (k_{33}) perpendicular to the foliation.

D.4.2 Method and results for cores between 0 and 2500 m

A nonstationary method was used for determination of the thermal conductivity. The sensor consists of a heating wire and a closely attached thermistor. Both are contained in a steel tube (length 70 mm, diameter 2 mm), which is embedded on the surface of a thermally nonconducting solid (Fig.D.4.1) (for more details see RAUEN et al., 1988; ERBAS, 1985). This probe is pressed (5 bars) on the cut and polished surface of the core with 2.5 % Dehydril HT (HEINSCHILD et al., 1988) used to improve contact.

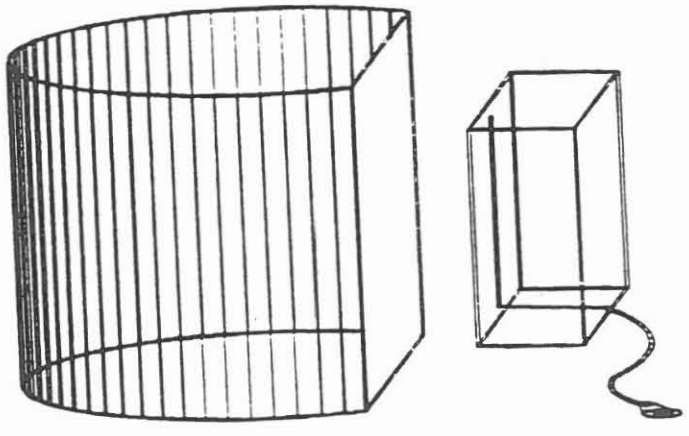

Fig. D.4.1: Vertical cut core and line source probe.

The current through the heating wire is kept constant during the measurement with variations less than 0.02 %. The temperature increase is measured with a resolution greater than 5/1000 K; the sampling interval is 1 second ($\pm 10^{-6}$ s).

Equation [2] describes the longtime solution of the temperature of the line source, T(t) in °C, which is heated with the constant power density of the line source, Q in W/m, on the surface of a solid with the thermal conductivity, k in W/(mK), (see KRISTIANSEN, 1982).

$$T(t) = \frac{Q}{2\pi k} * \ln(t) + \text{const} \qquad [2]$$

To get the longtime solution, [2], of the heating, the influence of the contact between probe and rock, which gives a lower time limit of the validity of equation [2], is taken into account. An upper limit is posed by the boundary effects of the probe and the rock. For evaluation of the temperature-time curve, a method developed by ERBAS (1985) is used. The accuracy of the conductivities calculated with this method is approximately 5 %. The method used is controlled with calibration bodies.

Equation [3] describes the temperature-time approach T(t) of a constant heated line source (see KRISTIANSEN, 1982) in a homogeneous isotropic solid (coefficients A_i, i = 1...4). The derivation of [3] to ln(t) leads to a time-function of the apparent thermal conductivity of the solid, $k_a(t)$, equation [4]. The values of this function are called 'apparent' because only the longtime solution as represented by equation [2] allows us to refer to a property of the solid.

$$T(t) = A_1 + A_2 * \ln(t) + A_3 * \frac{\ln(t)}{t} + \frac{A_4}{t} \qquad [3]$$

$$K_a(t) = \frac{Q}{2\pi \left(A_2 + A_3\left(\frac{1}{t} - \frac{\ln(t)}{t}\right) - \frac{A_4}{t}\right)} \qquad [4]$$

To evaluate the measurements, we try to fit equation [3] to the measured heating curve within any possible contiguous part (longer than 30 seconds) of an outer time interval (30 to 80 seconds). For each fit, we get coefficients A_i (i = 1...4) for the function [4], thus obtaining a large group of different functions. ERBAS (1985) has shown that the set of coefficients that causes the maximum of $k_a(t)$ to appear at the highest time, gives the best approximation to the real thermal conductivity, minimizing contact and boundary effects. This method has the advantage that it does not need any further calibration.

The heating curve is measured five times after removing and replacing the probe at every position of the line source on the sample. Thus, we get a mean value and a standard error of the mean. High standard errors of the mean are caused by variations, within a few cubic centimeters, in the mineralogy of the samples.

Three positions of the line source are usually chosen on the horizontal rock plane - one parallel to the 0°-direction (0° = preliminary reference), one parallel to the 90°-direction, and one parallel to the borehole on the vertical cut core (Fig.D.4.1). This vertical cut produces a plane which is 80 mm wide and more than 80 mm long.

With the line source, thermal conductivity of the plane perpendicular to the direction of the line is measured. The denotation of the two directions which span this plane, for example, $k_{90/z}$, $k_{0/z}$ and $k_{0/90}$, are used.

Figure D.4.2 represents the thermal conductivity log of the first 2500 m, which has in part already been published (RAUEN et al.,1988; and LIPPMANN et al., 1988). Conductivity values parallel to the horizontal plane (= 0°/90°), and results from the first 500 m have not yet been published. Lower values were distinguished at the metabasites and higher at the gneisses. The foliated gneisses have different thermal conductivities in the three measured planes. Further discussions should be done after transformation of these values to main axis thermal conductivities (see chapter D.4.4).

D.4.3 Thermal conductivity of VB1a cores between 1800 and 2500 m

Thermal conductivity of cores between 1800 and 2500 m was determined with an average sampling interval of approximately 5 m (Fig. D.4.3). Values range from 2 to 4 W/mK depending on mineralogy and on the direction of the line source relative to the sample. The measurements were made on foliated gneiss, with the exception of some lamprophyre dykes (with conductivities as low as 2.3 W/mK at 2082.47 m) and quartz veins (>6 W/mK at 2485.33 m). When these results are compared with those from gneiss between 500 and 992 m (Fig. D.4.2), it is significant that conductivities less than 3 W/mK were often measured.

Fig. D.4.2: Thermal conductivity in W/(m K) with standard error of the mean of KTB cores from 0 - 2500 m. Symbols: o-parallel 90°/z; solid circles parallel 0°/z; x-parallel 0°/90°.

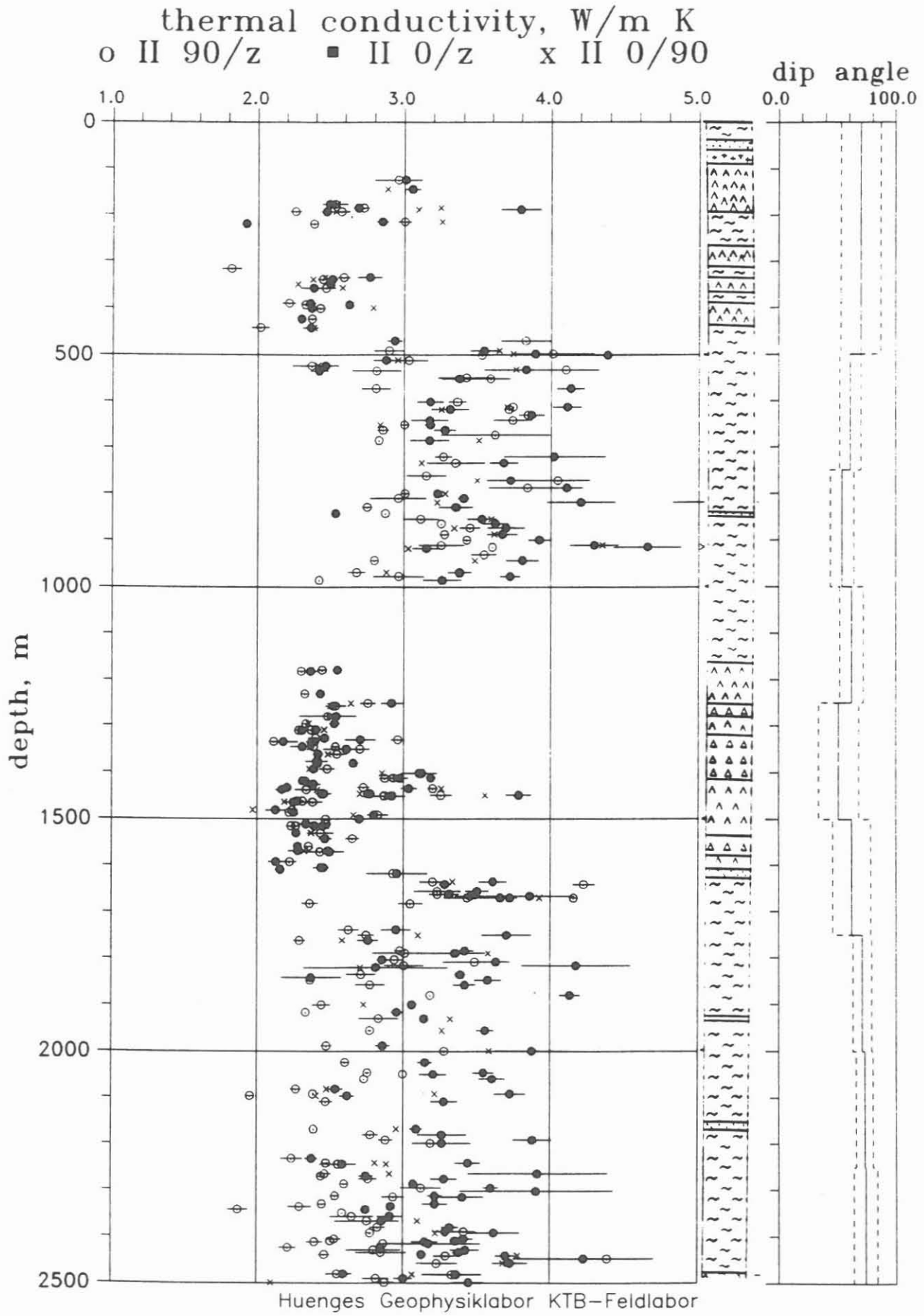

Fig. D.4.3: Thermal conductivity in W/(m K) with standard error of the mean of KTB cores from 1800 - 2500 m. Symbols: o-parallel 90°/z; solid circles parallel 0°/z; x-parallel 0°/90°.

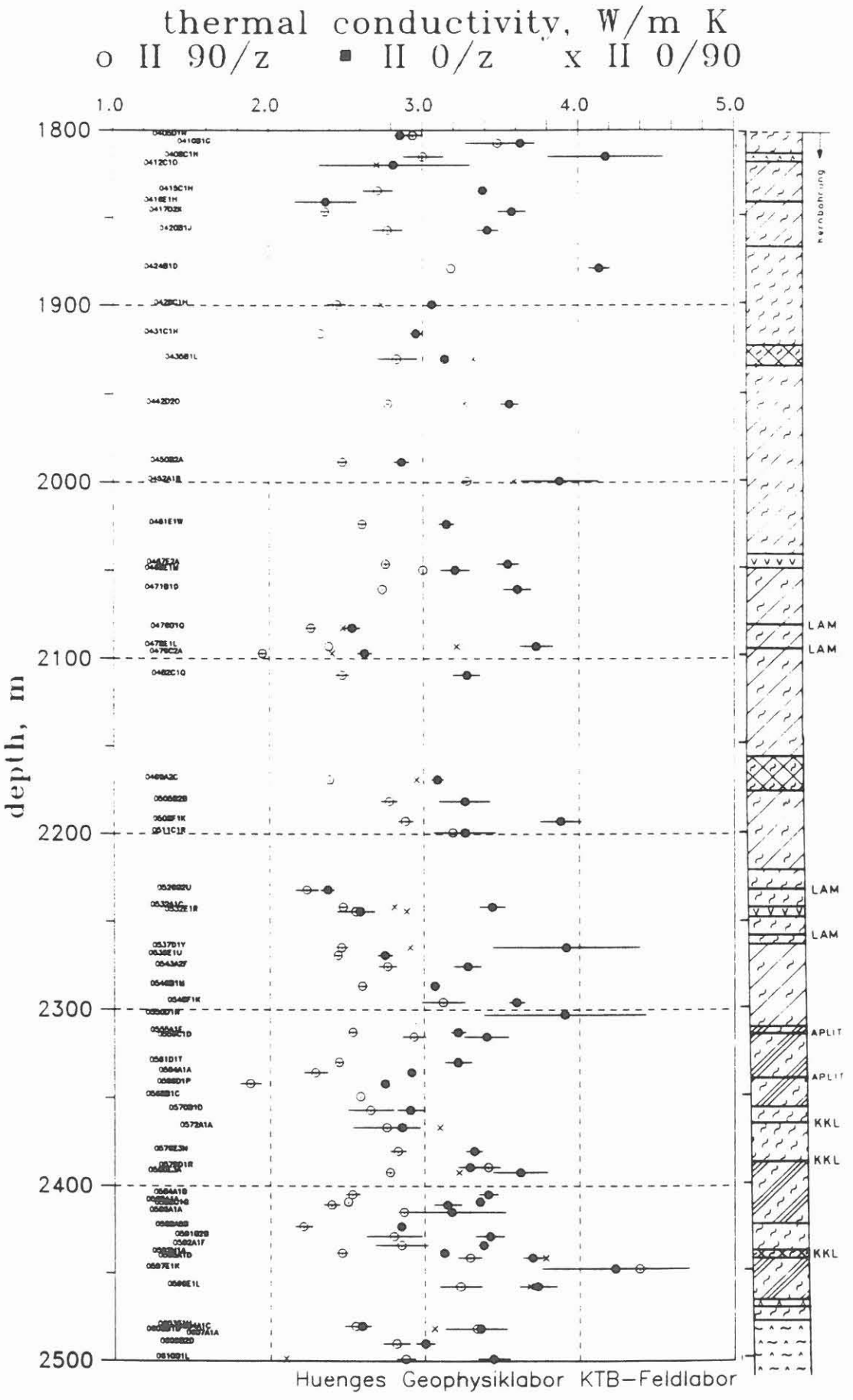

D.4.4 Transformation of the measured thermal conductivity to the main axis

The thermal behaviour of the rocks can be characterized better if the data are transformed to the main axis thermal conductivity. GRUBBE et al. (1983), and in more detail KÖNIG (1988), developed a transformation for thermal conductivities measured with a line source (in our case, $k_{90/z}$, $k_{0/z}$ and $k_{0/90}$) to main-axis values (k_{11} and k_{33}).

Visible structural parameters (azimuth of dip, β, and dip angle, α, of the foliation measured by the geology group; see chapter B) are used for the transformation which is based on three equations [5,6,7] for determination of k_{11} and k_{33}.

$$k_{90/z}^2 = k_{11}k_{33}\,(1 - \sin^2\beta\,\sin^2\alpha) + k_{11}^2\,\sin^2\beta\,\sin^2\alpha \qquad [5]$$

$$k_{00/z}^2 = k_{11}k_{33}\,(1 - \cos^2\beta\,\sin^2\alpha) + k_{11}^2\,\cos^2\beta\,\sin^2\alpha \qquad [6]$$

$$k_{0/90}^2 = k_{11}k_{33}\,\sin^2\alpha + k_{11}^2\,\cos^2\alpha \qquad [7]$$

Figures D.4.4a - d show the distribution of the thermal conductivities parallel and perpendicular to the foliation for four borehole sections between 0 and 2500 m. Figure D.4.4a shows that alternating layers within the first 530 m do not produce a uniform main axis thermal conductivity distribution. Thermal conductivity distribution of the other sections is obviously related to the lithology of the rocks. Strong anisotropy of gneiss between 530 and 992 m and between 1610 and 2500 m can be recognized. Metabasites between 1160 and 1610 m are weakly foliated (see KEYSSNER et al., 1988) and there is no notable anisotropy in thermal conductivity. Table D.4.1 lists the mean values and standard deviations of the main axis thermal conductivity and the thermal conductivity parallel to the borehole within the four sections.

We believe that the different anisotropies in the four sections are related mainly to the content and distribution of quartz and mica in the rocks. Results of an investigation of this will be reported in a future KTB report. In particular, the lower thermal conductivity for k_{11}, from 1610 - 2500 m compared to 530 - 992 m must be explained.

Fig. D.4.4: Distribution of the thermal conductivity perpendicular (dotted lines) and parallel (solid lines) to the foliation of KTB-cores from 4 depth intervals.

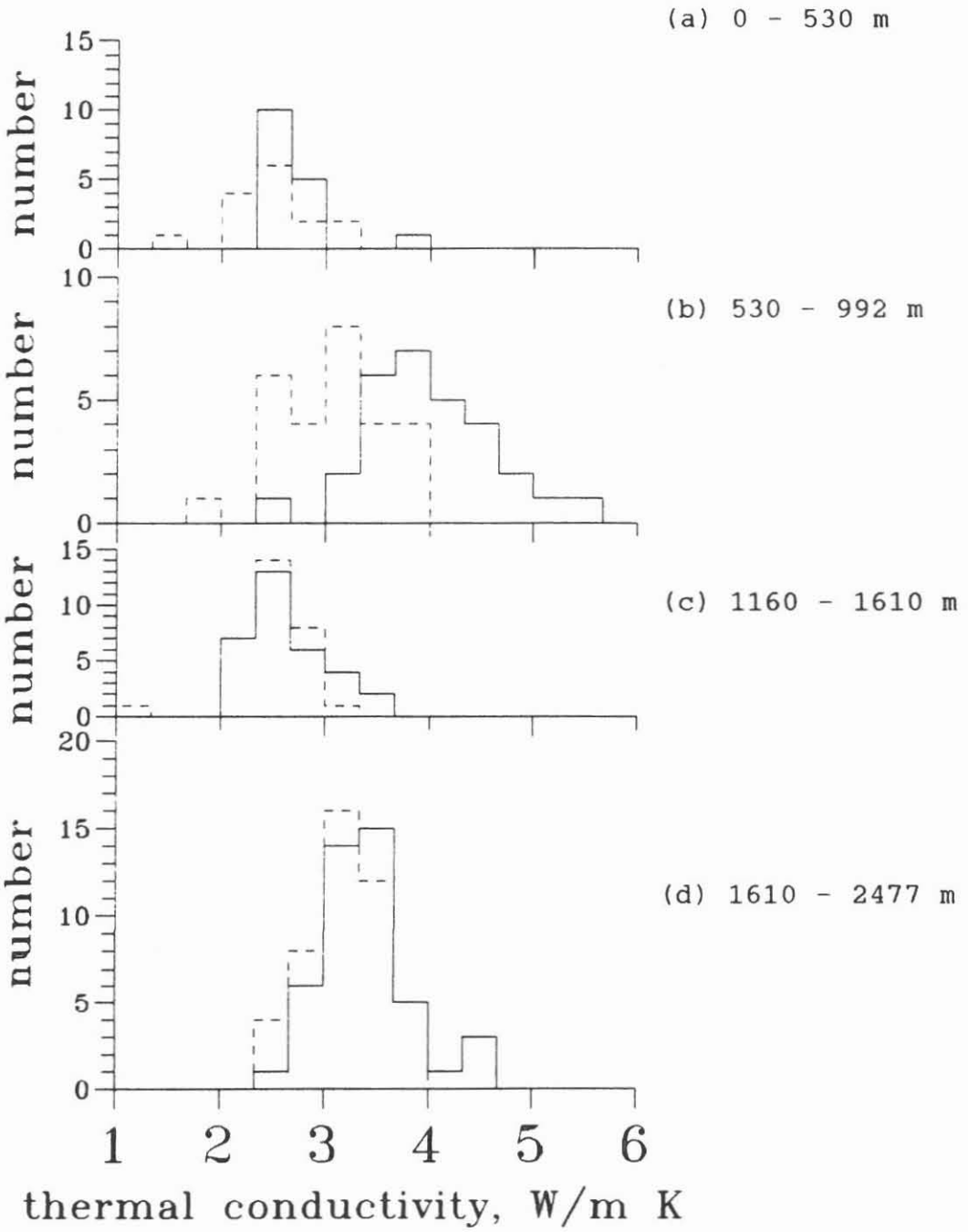

D.4.5 Determination of the thermal conductivity parallel to the borehole

Thermal conductivity parallel to the borehole (k_Z) is needed for interpretation of the temperature profile because grad T is also measured parallel to the borehole. There are two possible ways to determine k_Z.

If three measurements are possible ($k_{90/z}$, $k_{0/z}$ and $k_{0/90}$), k_Z can be calculated with equation [8]. If only two measurements are possible, k_Z can be calculated from main axis thermal conductivity with equation [9] (see KÖNIG, 1988).

$$k_z = \frac{k_{90/z} * k_{0/z}}{k_{0/90}} \qquad [8]$$

$$k_z = k_{11} - \cos^2\alpha \, (k_{11} - k_{33}) \qquad [9]$$

Figure D.4.5 shows the individual conductivities of samples parallel to the borehole. Table D.4.1 presents a summary of these results from 0 - 2500 m for the four intervals previously discussed:

- low to medium thermal conductivity of 2.7 (7) W/m K above 530 m with a high standard deviation due to the alternating layers of gneisses and metabasites
- medium to high values of 3.4 (5) W/m K between 530 and 992 m with a high standard deviation due to the local high variation of the dip angle within the gneiss section
- low values of 2.6 (3) W/m K from 1160 to 1610 m within the metabasite section
- intermediate values of 3.1 (5) W/mK from 1610 to 2500 m.

Fig. D.4.5: Thermal conductivitiy of the KTB-VB cores parallel to the borehole with mean error.

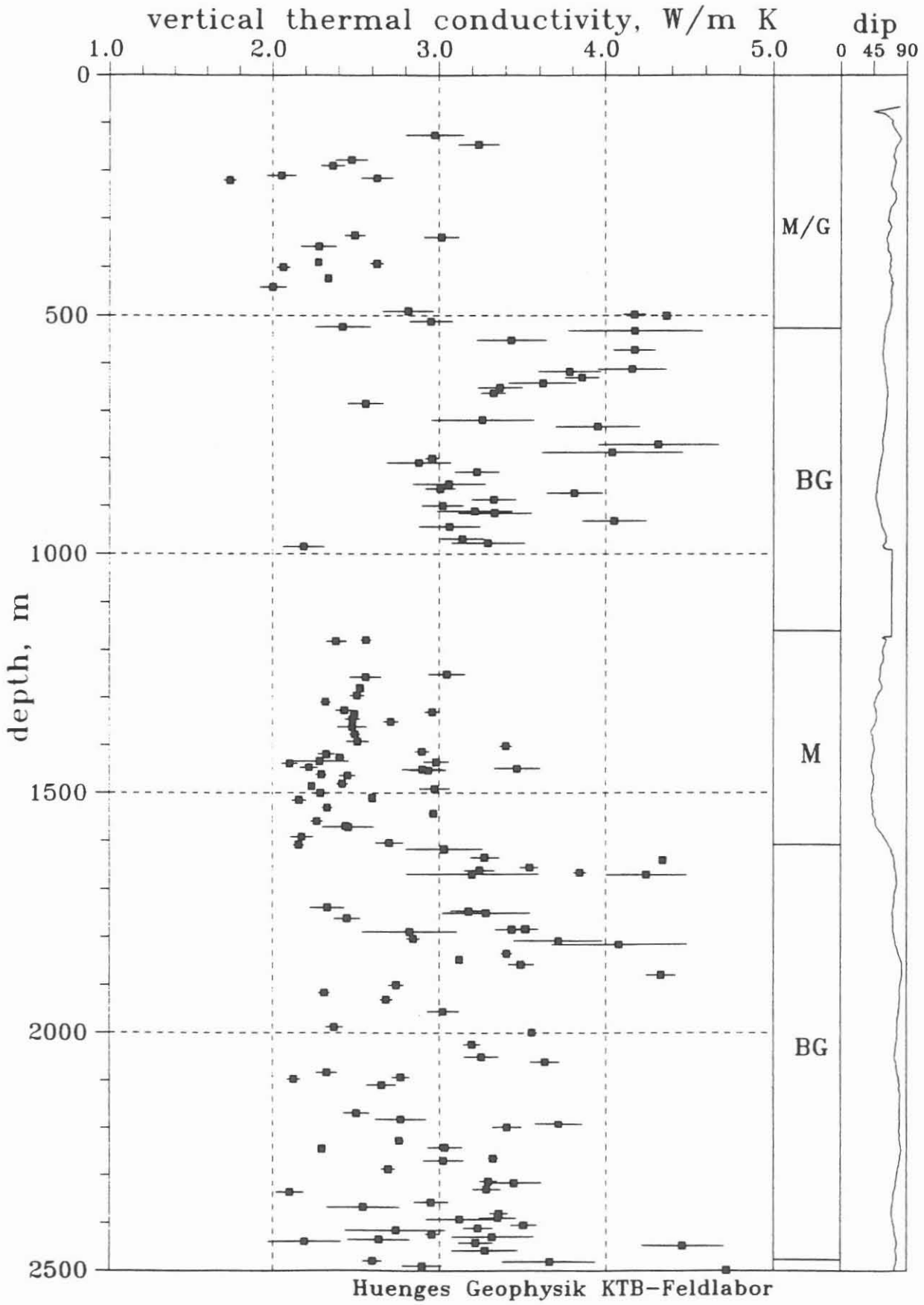

Tab. D.4.1: Summary of the transformed mean thermal conductivity results for four borehole sections (standard deviation in parentheses).

depth in m	main lithology	thermal conductivity in W/m K		
		parallel to the foliation	perpendicular foliation	parallel to the borehole
100 - 530	alternating gneisses and metabasites	2.7 (4)	2.6 (5)	2.7 (7)
530 - 992	gneiss	4.0 (6)	3.1 (5)	3.4 (5)
1160 - 1610	metabasite	2.6 (4)	2.5 (4)	2.6 (3)
1610 - 2500	gneiss	3.4 (5)	3.1 (5)	3.1 (5)

D.5 Electrical Conductivity

D.5.1 Introduction

Electrical conductivity (resp. its inverse, the electrical resistivity) was measured on VB1a cores above 2500 m with a new apparatus described in the following section. With this equipment, measurements on non-prepared cores can be made. Detailed electrical conductivity measurements can also be made on selected cores. The equipment which was formerly used (standard 4-electrode configuration) and earlier results are described in RAUEN et al. (1988).

D.5.2 Equipment used for the detailed measurements of electrical resistivity: the "Mini-Wenner" apparatus

D.5.2.1 Measurement apparatus

This new apparatus shown schematically in fig. D.5.1, was developed by the scientists of the KTB field laboratory and the "Institut für Allgemeine und Angewandte Geophysik" of the University of Munich.

An oscillator generates a square-wave alternating voltage with a frequency of 150 Hz. This voltage is applied to a "current-source-module", which generates an alternating current of this frequency with a constant amplitude. This amplitude can be adjusted in four steps from 78 µA to 0.15 µA. If the desired current cannot be obtained (e.g., because of breaks in the electric circuit or high-resistive core), an LED automatically lights, so the operator can reduce the current.

The electrical circuit is closed via the current-emitting electrodes and the core itself. The electrodes consist of porous plastic pins, which contact the surface of the core over an area of several mm^2. The pins are placed inside brass-liners, which are connected to the electrical circuit. The porous pins are soaked with tap-water to decrease contact-resistance versus direct metallic contact.

The alternating voltage is measured between two identical electrodes and then amplified and fed to a lock-in-amplifier. It compares the input signal with a reference signal from the oscillator and makes measurements at exactly the same reference-phase, which greatly improves signal to noise-ratio. The output of the lock-in-amplifier is a direct

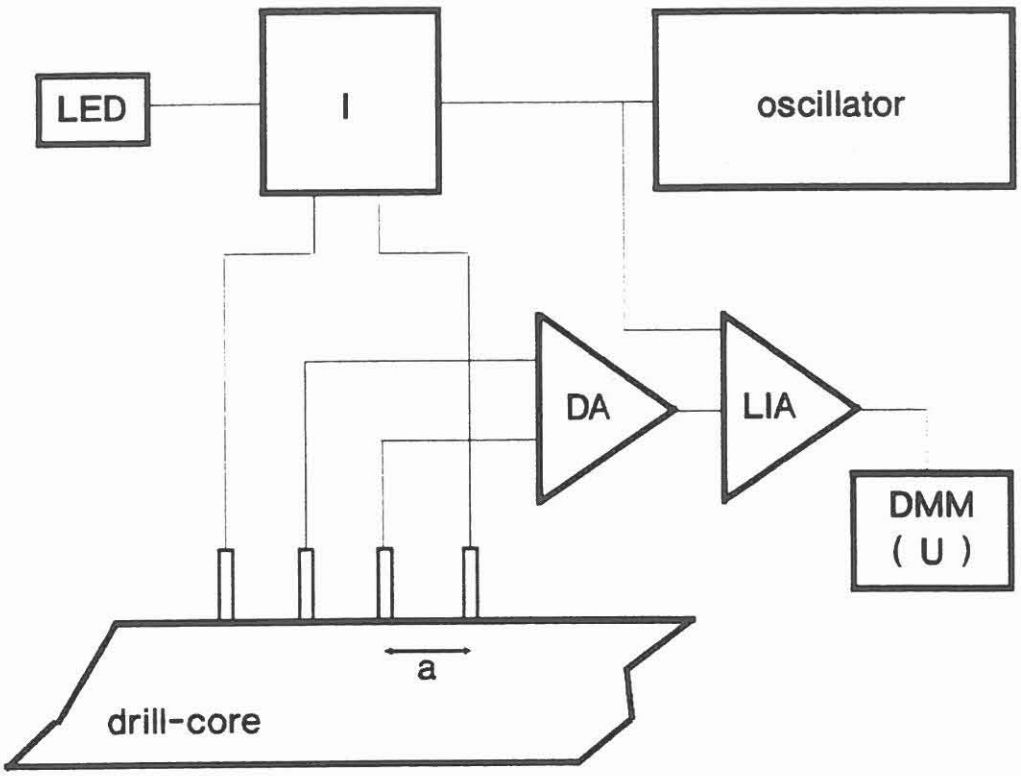

Fig. D.5.1: Schematic of the apparatus used for detailled measurement of resistivity. Specimen is a piece of drill core, which does not need to be prepared.

Symbols:

LED = signal to indicate overmodulation.
I = source of alternating current with a constant amplitude
DA = differential amplifier.
LIA = lock-in-amplifier.
DMM = digital multimeter (measuring direct voltage).
a = distance of electrodes in WENNER-geometry (here: 2 cm).

See equation [1] for computing (apparent) resistivity.

voltage proportional to the amplitude of measured signal. This direct voltage is measured by a normal digital multimeter.

An advantage of the constant current source is that the operator does not to have to measure the current. The only measured parameter is the voltage, which is directly proportional to resistivity.

D.5.2.2 Arrangement of electrodes

All four electrodes are arranged in a line and are set in equal distances. The two middle electrodes are the potential electrodes; the outer two are the current emitters. Distances between two neighboring electrodes can be as small as 1 cm. In applied geophysics a similar configuration is usually called a WENNER-configuration (see DUCKERT, 1961). "Apparent" resistivity (in Ωm) is calculated with the following equation :

$$rho_a = \frac{U}{I} * 2\pi a \qquad [1]$$

where :
U = voltage [V]
I = current [A]
π = 3.14 ..
a = distance of the next 2 electrodes [m].

Apparent resistivity equals real resistivity if the measured object is a "homogeneous half-space" (i.e. expands infinitely horizontally and vertically under the electrodes and has homogeneous and isotropic conductivity). Results of DUCKERT (1961) and our own test measurements show that this condition is approximately fulfilled for our cores with ø ≈ 10 cm and electrode seperations up to 2 cm. Smaller pieces of core (with dimensions similar to the overall electrode seperation) do not fulfill this condition, but the influence of such geometric effects can be calculated.

The electrical conductivity σ (in 1/(Ωm) = S/m = mho/m) corresponds to the inverse of the specific electrical resistivity.

D.5.2.3 Measurement method

Each core sample is placed in a tap-water bath for approximately 24 hours before measuring to saturate open and near-surface cracks. Thus conditions are similar to the mud-filled borehole and there are comparable conditions for each measurement. Then the core is placed between 2 parallel rollers allowing easy ratation of the core around its vertical axis. Electrode distance is set to 2 cm. Twelve measurements are made parallel to the vertical axis, around the mantle surface of each core. The mean value and standard deviation of resistivity is calculated from these 12 voltages. Figure D.5.2 shows an example in which a drastic decrease in resistivity is seen, due to the influence of a graphite-filled crack.

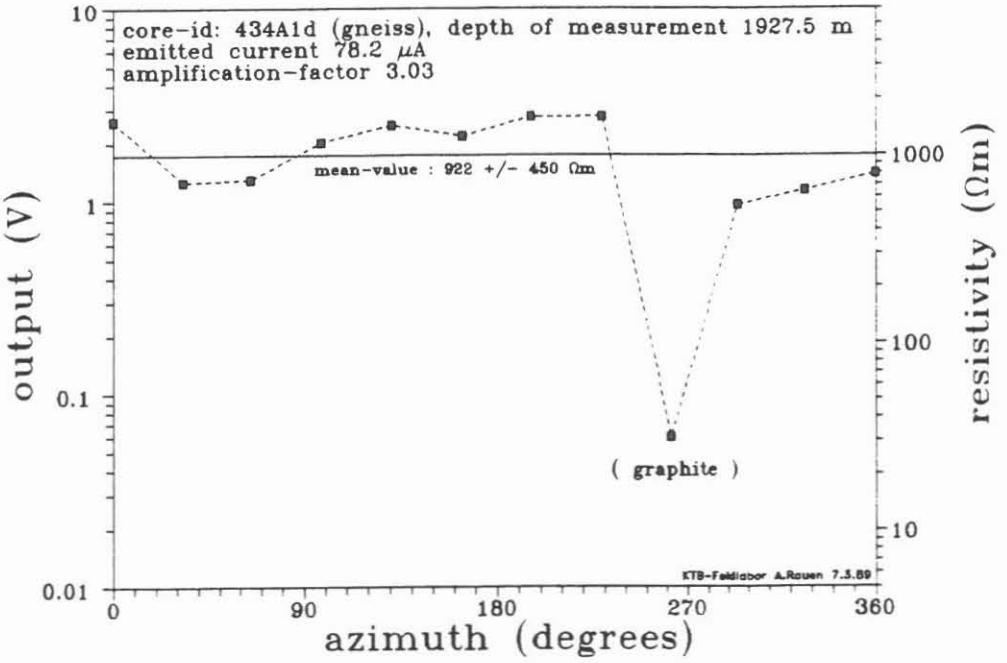

Fig. D.5.2: Example of a total series of measurements with the small electrodes in WENNER-geometry. On the left, the output voltage of the lock-in-amplifier is shown as a function of measurement azimuth to the reference line of KTB field laboratory. On the right is the calculated resistivity. The minimum of ≈ 30 Ωm was observed next to a graphite-filled crack, a few mm in thickness.

In the case of smaller pieces of core, fewer measurements are taken, because of the smaller surface. The electrode arrangement used has the advantage that small pieces of core and detailed variations of resistivity of a core piece can be measured without preparing the sample.

D.5.3 Results from 1709 m to 2500 m

Figure D.5.3 shows the distribution of electrical resistivity data and figure D.5.4 is the depth-log of resistivity. The data distribution can be approximated by a logarithmical normal distribution. Such a log-normal distribution can also be seen in susceptibility data (see chapter D.8). Because data follow a logarithmical normal-distribution, averaging is not calculated arithmetically, but logarithmically.

Measurements were made on one core per 4 m in gneisses from 1800 m to 2500 m (see figure D.5.4). The measured values scatter around the (logarithmic) mean of 4090 Ωm.

A fault-zone at 1926 m is of special interest. There, core surfaces have thin layers of graphite. Low resistivities of ≈ 13 Ωm (at certain single points < 5 Ωm) were measured on this graphite planes. This decrease in the resistivity must be caused by an increase in the electronical conductivity.

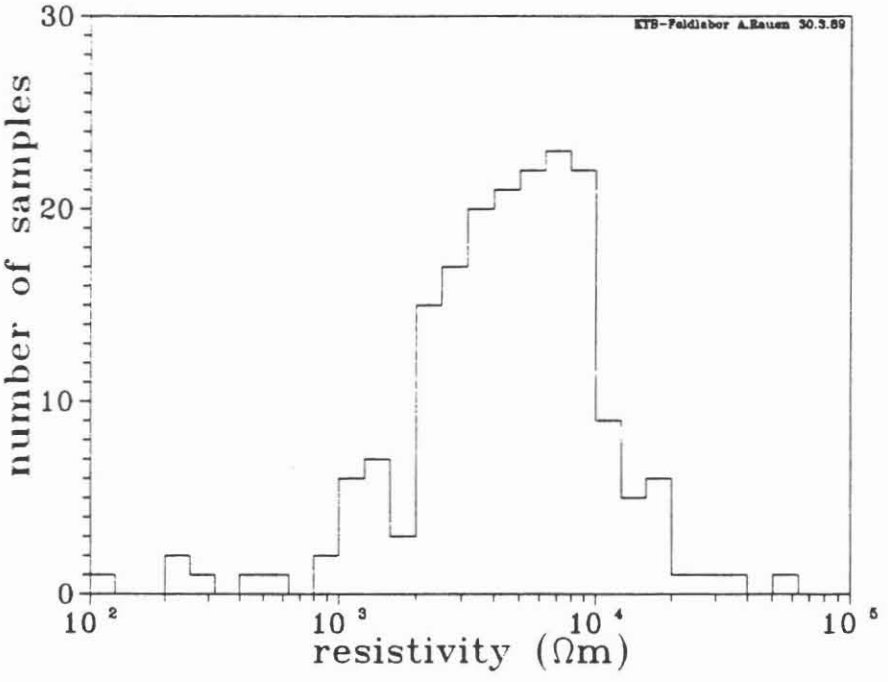

Fig. D.5.3: Distribution of resistivity data. The resistivity interval from 100 Ωm to 100 000 Ωm is logarithmically divided into 30 parts. The total number of measured values within each interval is plotted.

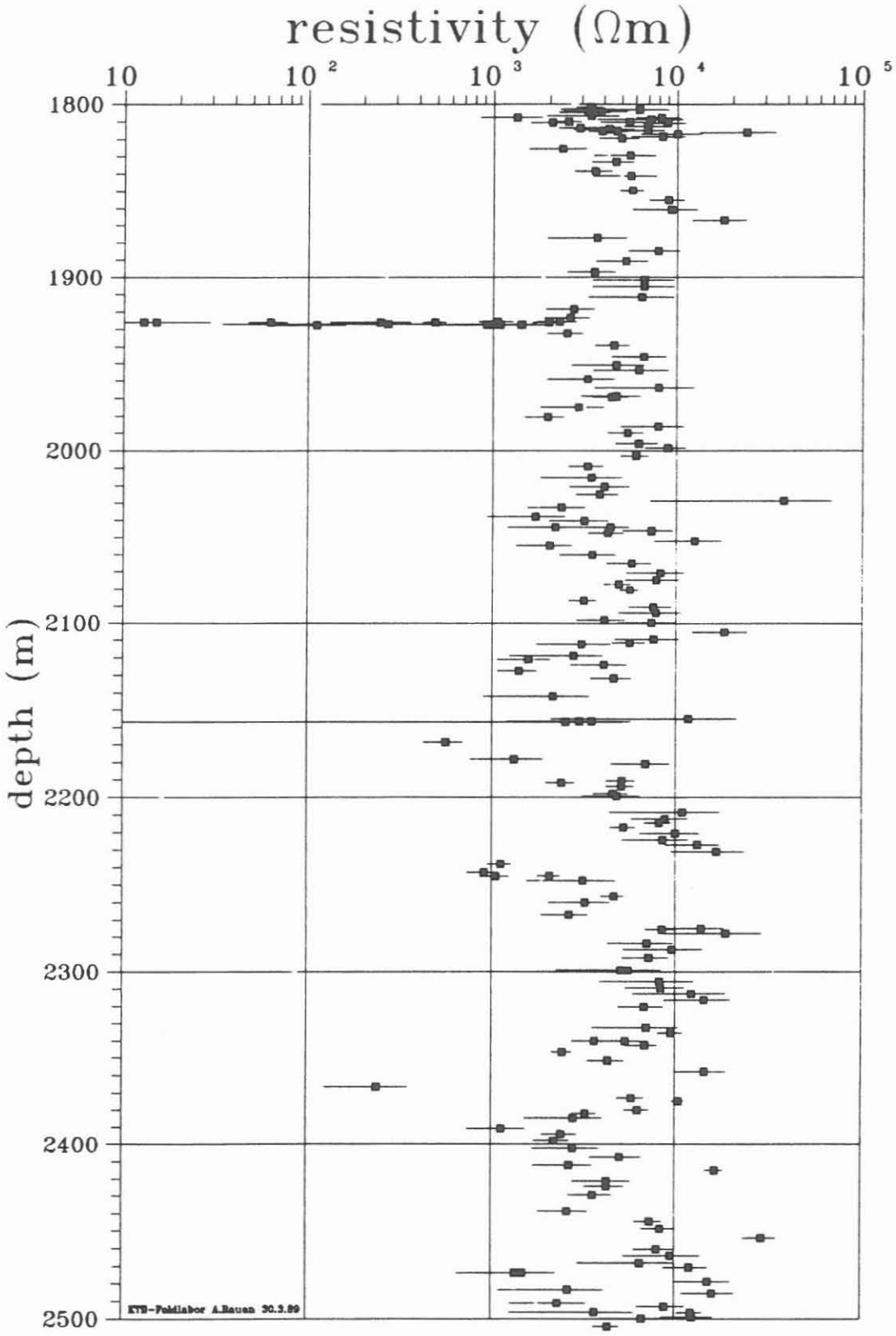

Fig. D.5.4: Depth log of electrical resistivity from 1709 m to 2500 m. The arithmetic mean-value ± standard deviation of generally 12 measurements for each core is plotted.

D.6 Natural Remanent Magnetization (NRM)

D.6.1 Introduction

The NRM was determined on 239 core pieces (KM 409 to KM 611) from the start of coring in hole VB1a at 1802 m to 2550 m. On average, at least one core piece per cored interval was examined. The average sample interval was about 3 m, but this was reduced whenever significant magnetic anomalies became apparent.

Details regarding the measurements and equipment used are given in RAUEN et al. (1988). Chapter B of this report provides a detailed lithologic description.

D.6.2 NRM depth log

The depth log of the NRM (Fig. D.6.1) shows two clearly separated zones. The interval from 1800 m to 2220 m is distinguished by its weak magnetization of less than 100 mA/m. This is related to the presence of gneiss and lamprophyric dykes (e.g., at 2048 m). Comparable magnetization values were measured in gneiss between 500 m and 992 m (see also WIENAND et al., 1988). The gneiss from 2220 m to 2365 m has a distinctly higher magnetization with peaks up to 2000 mA/m. A weakly magnetized interval occurs below this to 2470 m where the magnetization values again vary between 10 mA/m and 300 mA/m. This lowest section from 2470 m - 2500 m is characterized by a metablastite-amphibolite sequence (see also chapter B). Its magnetization is comparable to that of the amphibolite from 1160 m - 1610 m (see also RAUEN et al., 1988).

The increased magnetization between 2220 m and 2365 m cannot be correlated with a change in lithology. The litholog shows a monotonous sequence of gneiss interrupted only by some lamprophyric dykes (see also chapter B). The susceptibility data also show higher values in this interval. Geochemical analysis of centrifuge samples did not indicate any specific anomalies, e.g., an increased content of iron-sulphur compounds. Thin section microscopy, however, indicated an increased concentration of opaque minerals (ore phases; see also chapter B).

Using the NRM depth log for reference, samples for polished sections were taken and in cooperation with the petrographers, the magnetic ore phases were investigated. Pyrrhotite is irregularly distributed in the matrix and is partially orientated parallel to the foliation. It was also

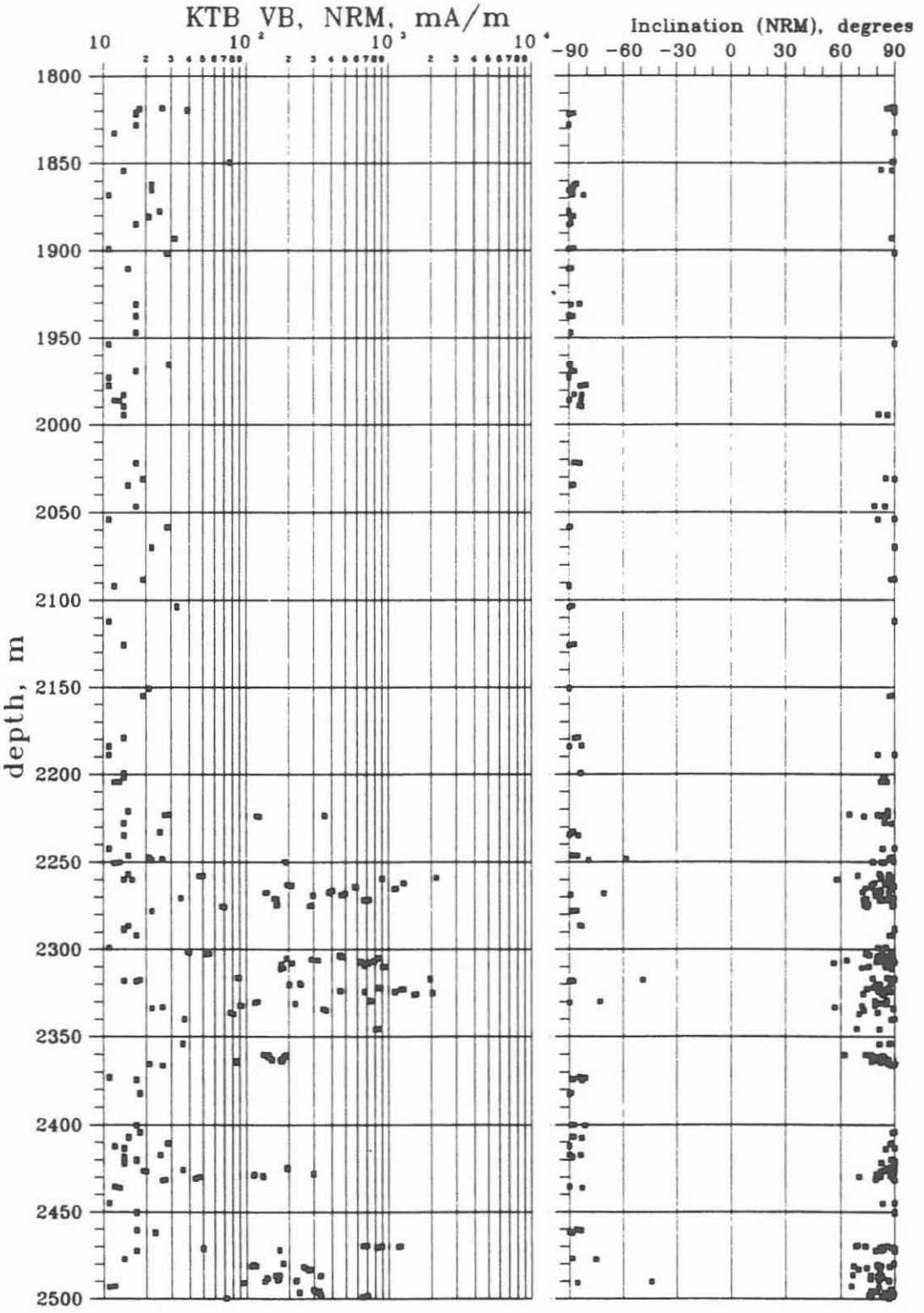

Fig. D.6.1: Left : depth log of the NRM.
Right: depth log of the inclination of the NRM.
The litholog indicates the presence of gneisses in the interval with increased magnetization values from 2220 m - 2365 m.

found on the shear planes of the gneisses. By applying a 'Ferrofluidum' (superparamagnetic magnetite particles in an organic carrier substance which inhibits their clustering; see e.g., SOFFEL, 1968) in the ore microscopy, pyrrhotite could be clearly distinguished from pyrite. No other magnetic minerals (e.g., magnetite or hematite) were detected in the polished sections (see also chapter B: ore mineralization).

PUCHER (1986) also identified pyrrhotite by rock-magnetic investigations as the carrier of magnetization in the surface amphibolites east of Erbendorf. Likewise, BADER & STETTNER (1988a) consider pyrrhotite to be the effective mineral of the magnetic anomaly zone of Erbendorf-Vohenstrauss. They point out that the anomalies which were detected by ground magnetics generally appear at the margins of large amphibolite bodies just as in gneisses. In the KTB well, a magnetic anomaly was traced for the first time through a gneiss complex from 2220 m - 2365 m after another strong anomaly had been measured in a 40-m-thick gneiss sequence between 200 m and 240 m (see also BÜCKER et al., 1988).

In Figure D.6.2, the components of the magnetization (x, y, z; with x = 0° referred to the field laboratory reference line, z = core axis) are plotted against depth. It is evident that the z component is dominant in depth ranges with strong magnetization resulting in steep inclinations.

D.6.3 Inclination of the NRM

The depth log of inclination of the NRM (Fig. D.6.1) shows mainly steep negative and positive inclinations which is similar to observations made higher in the hole. Negative inclinations could hardly be established in the strongly magnetized interval between 2220 m and 2365 m (see also Fig. D.6.2). The accumulation of negative inclinations at weaker magnetizations was noticeable and became especially evident in the plot of NRM versus inclination of the NRM (Fig. D.6.3).

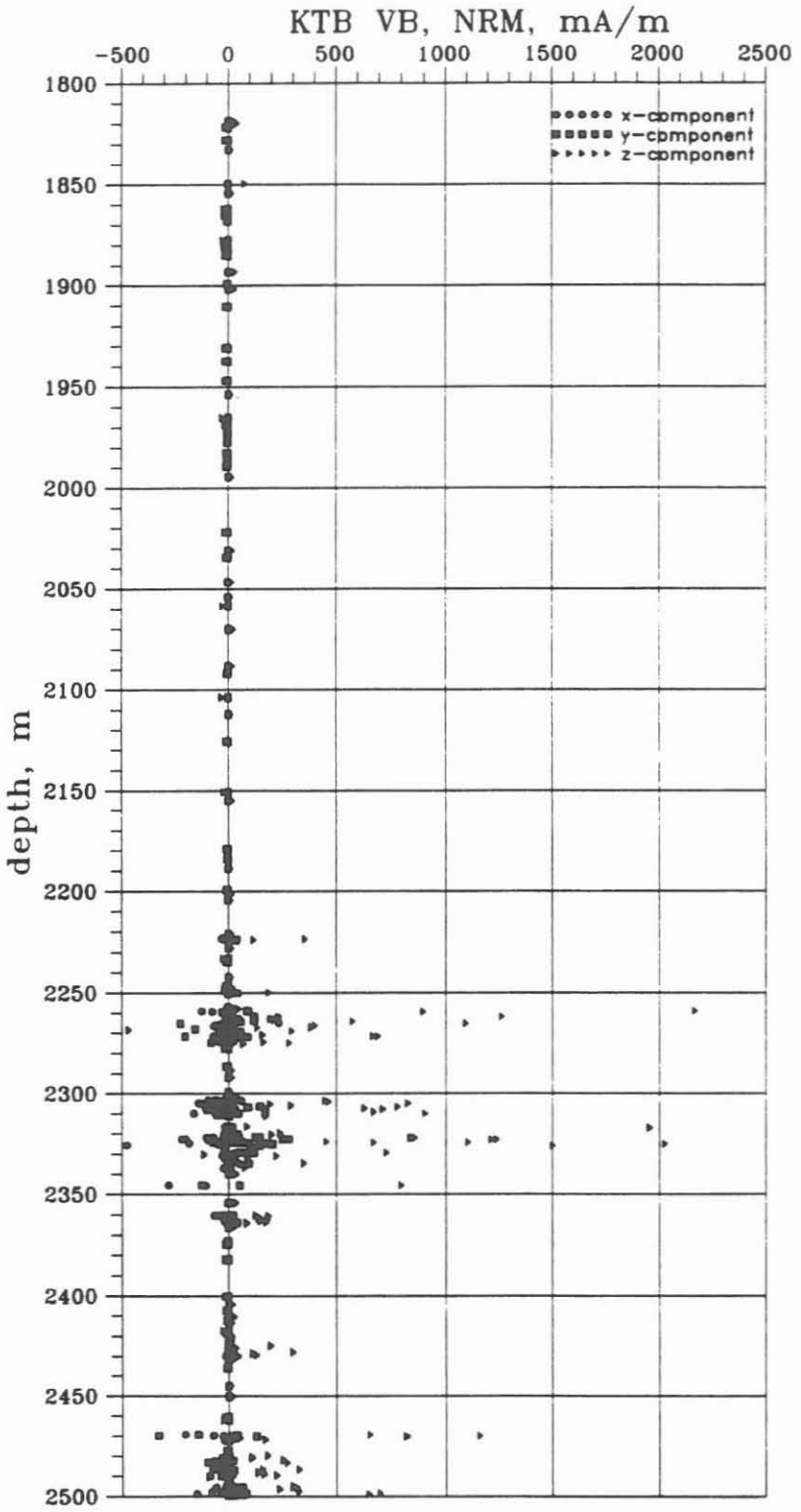

Fig. D.6.2: Depth log for the x-, y- and z- components of magnetization. The z-component is dominant in depth ranges with strong magnetization .

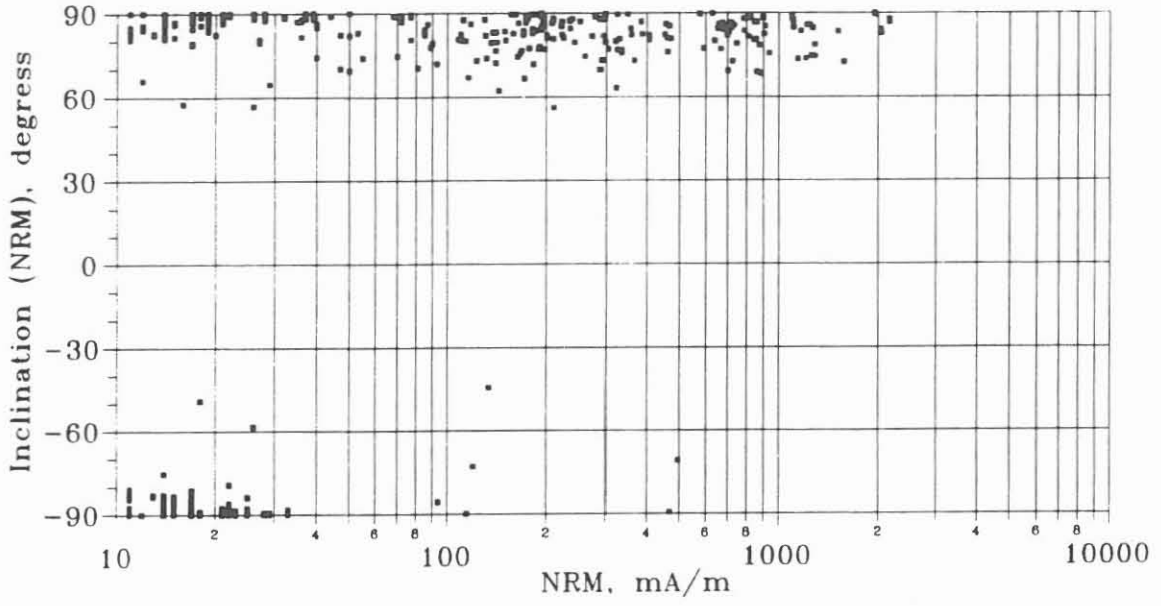

Fig. D.6.3: Cross plot of NRM versus inclination(NRM). Steep negative inclinations mainly occur where there are weak magnetization values.

The magnetic field inside and outside of the assembled core barrel (including the drill bit) was investigated with a flux gate magnetometer (Fig.D.6.4) in order to determine why steep inclinations were observed, particularly with respect to DIRM (Drilling induced remanent magnetization). To make the measurement, the core barrel was arranged horizontally in an E-W direction. Strong inhomogeneous fields with an amplitude of about 0.1 mT were detected around the end of the drill bit. Inside the core barrel, the field was directed parallel to the barrel axis. A separate reading of the shoe of the inner core barrel showed that this part holds the strongest magnetization; its value exceeded the range (± 0.1 mT) of the applied magnetometer. However, with respect to the total amplitude, it is assumed that this magnetic field is not sufficient to cause the observed DIRM (see PETERSEN, 1978; RAUEN et al., 1988).

A relation between steep inclinations and weak remanences (low coercivity force) has been reported from DSDP (Deep Sea Drilling Project) drillholes and other wells (e.g., ADE-HALL & JOHNSON, 1976). OEZDEMIR et al. (1988) disagree with BURMESTER (1977) who believes that piëzoremanent mechanisms cause the DIRM. Moreover, the lithostatic pressure of about 0.7 MPa at 2500 m cannot alone produce the observed DIRM, because even at shallow depths and accordingly low pressures, steep inclinations are present. Rather, it can be assumed that the DIRM arises from the influence of the magnet field of the drill pipe and/or the drilling bit on the rock in combination with tension, temperature and vi-

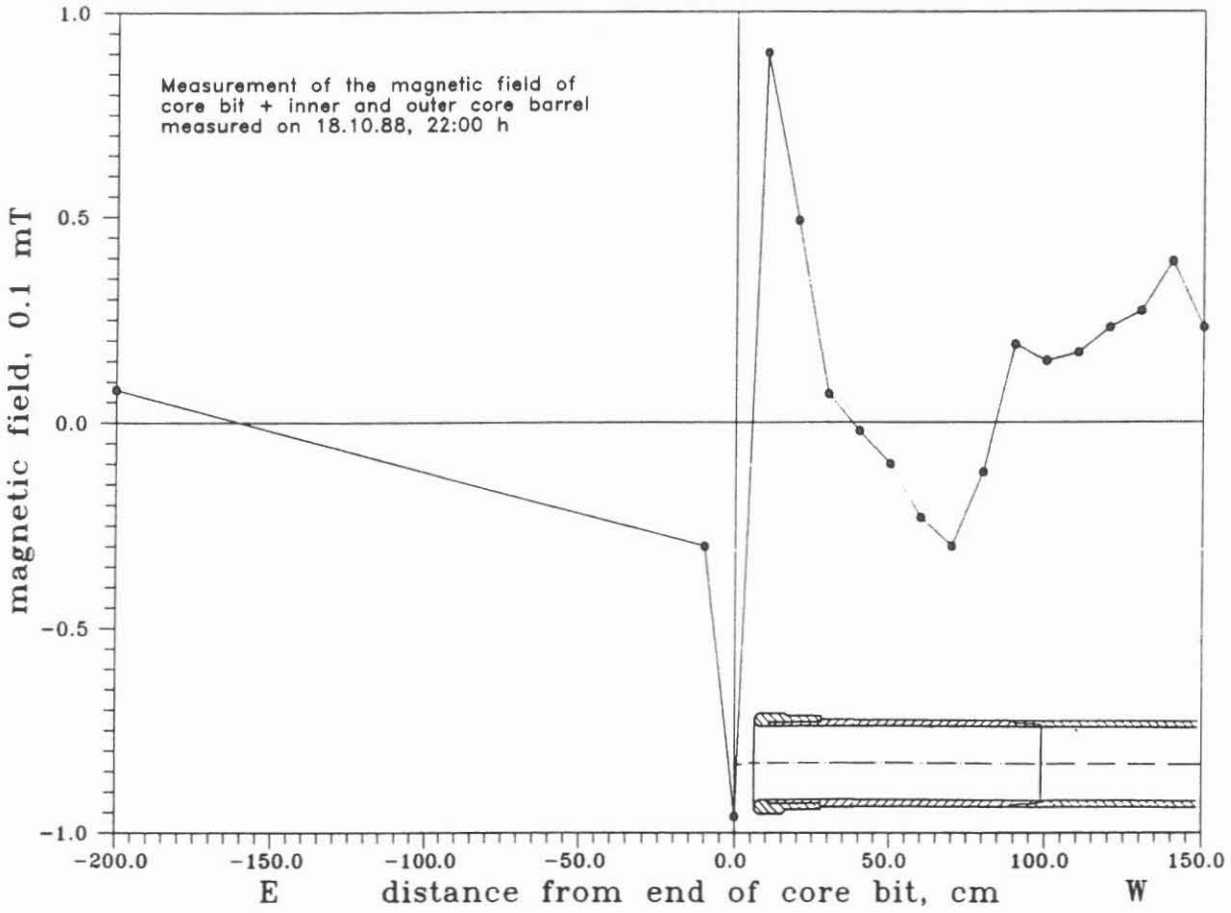

Fig. D.6.4: Detected magnetic field outside (negative x values) and inside (positive x values) of drilling bit and core barrel.

bration during drilling. Accordingly, the DIRM must be considered as a temporal, unstable magnetization (VRM, viscous remanent magnetization), which is imprinted on the core parallel to the dominant magnetic field of the drill bit. Thus, large magnetite grains at the fringe of the core receive the strongest influence (BURMESTER, 1977). From the publications previously referred to, it is assumed that the DIRM can be removed in most cases, by alternating magnetic fields with relatively low amplitudes or by relatively moderate temperatures. Measurements on plugs (ø = 2.5 cm) drilled vertical to the core axis indicated higher magnetization values and steeper inclinations for samples from near the margin of the core than for those close to the centre (POHL, personal communication). To more closely investigate these phenomena, a thesis project at the 'Institut für Allgemeine und Angewandte Geophysik' of the University of Munich is underway which will also address the DIRM problem in the KTB project.

D.6.4 Königsberger Q-factor

Figure D.6.5 is a plot of the natural remanent magnetization versus the induced magnetization from 1800 - 2500 m. There is good correlation between these two parameters, particularly for higher susceptibilities.

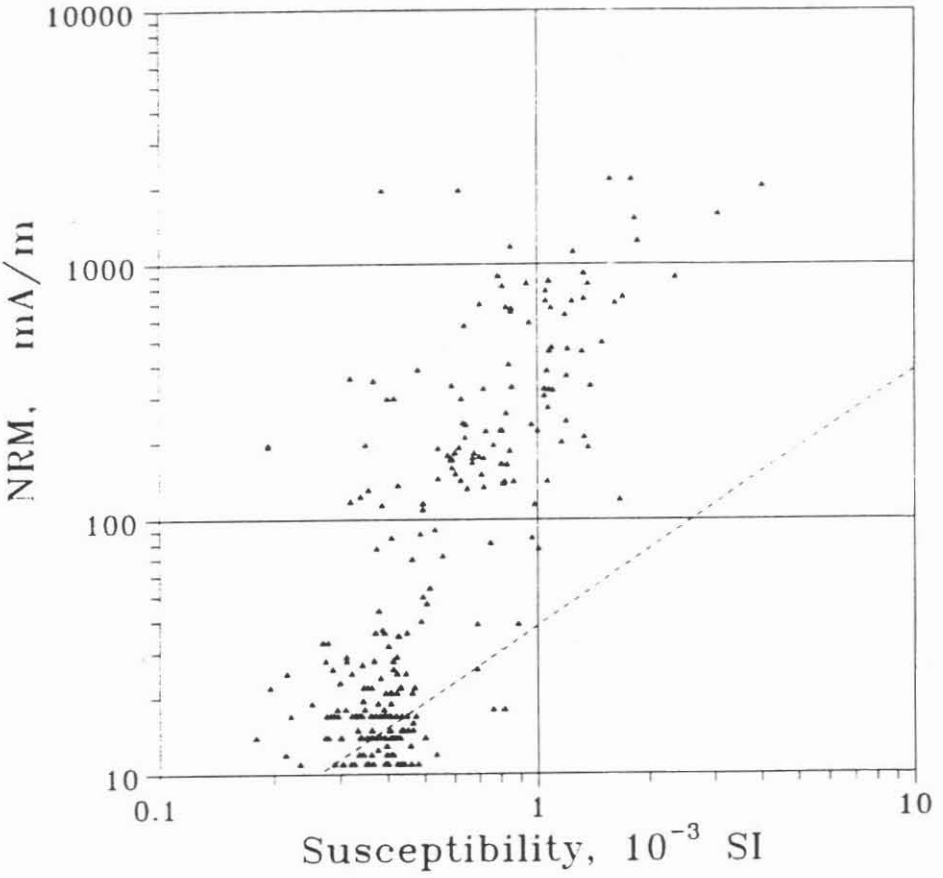

Fig. D.6.5: Cross plot of susceptibility versus NRM, measured respectively in equal depths. The dashed line indicates the induced magnetization (M_{ind} = X * H_{Earth}; H_{Earth} = 38.2 A/m) for the Upper Palatinade. Symbols above that line indicate measured values of cores with Q-factors greater than 1.

The depth log of the Königsberger Q-factors (quotient of remanent and induced magnetization, see COLLINSON, 1983; Fig. D.6.6) in the strongly magnetized interval from 2220 to 2365 m also shows Q-factors which are significantly higher than 1. Despite the very high induced magnetization (susceptibility) in this range, the remanent magnetization must be dominant.

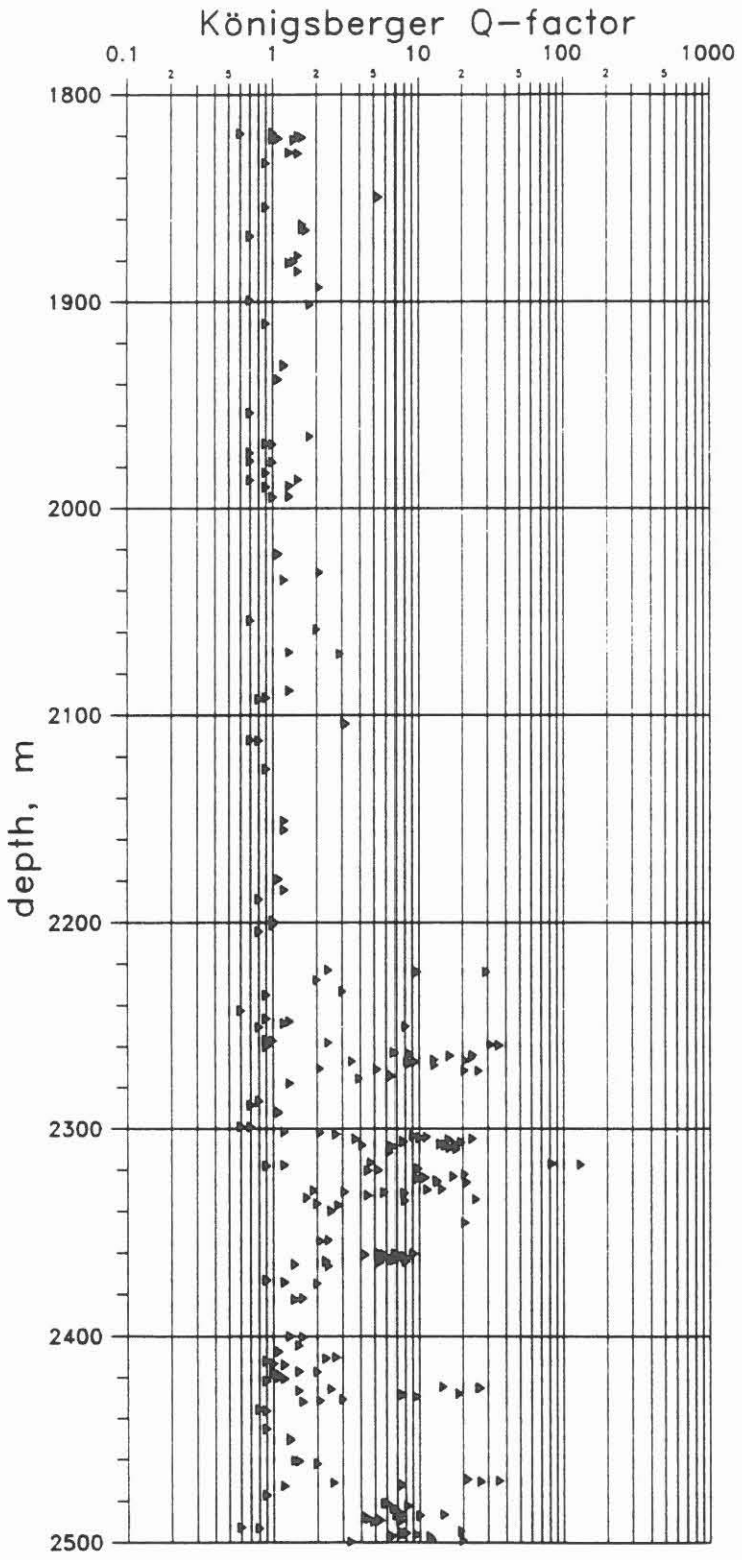

Fig. D.6.6: Depth log of the Königsberger Q-Factor (quotient of remanent and induced magnetization). Q-Factors greater than 1 were measured in intervals with high magnetic values (2220 - 2365 m).

D.7 Magnetic Susceptibility

D.7.1 Introduction

Magnetic susceptibility of cores and cuttings was determined using the procedures described in KTB Report 88-1 (BÜCKER et al., 1988). From the top of VB1a at 1709 m to 1800 m, only cuttings were available and only cores were taken from 1800 m to 2500 m. Sampling intervals were 1 m for cuttings and 1 cm for cores with the exception of badly fractured core samples.

D.7.2 Magnetic susceptibility of cores and cuttings

Susceptibility as a function of depth is shown in figure D.7.1 which has both linear and logarithmic scaling of the susceptibility axis.

Variance of the susceptibility of cuttings is higher than that of cores and mean values for cuttings are approximately 10 times higher. This is due to a changing and unknown fraction of cavings in the cuttings and a large amount of contamination by metallic abraded particles (often discernible to the naked eye). Similar trends in the susceptibility of cuttings have been described in KTB Report 88-9 (LIPPMANN et al., 1988).

The large volume of original core data (1 cm sampling interval) was compressed into a more manageable format by averaging over intervals of 20 cm (see RAUEN et al., 1988). Susceptibilities of cores usually show smooth behaviour over depth with characteristic values of around $0.35*10^{-3}$ SI for gneiss (see LIPPMANN et al., 1988). However, two intervals between 1709 m and 2500 m stand out: from 2250 m to 2370 m (susceptibilities equal more than $4*10^{-3}$ SI) and below 2470 m (susceptibilities are up to $3*10^{-3}$ SI).

Gneiss occurs in both of these intervals with high susceptibilities. This is unlike the upper regions of the borehole, where high susceptibility was generally associated with amphibolite. The high susceptibilities are very surprising, because the rocks are indistinguishable from other gneisses in all other than magnetic physical properties. Amphibolite lenses in the gneiss which raise susceptibility, occur only below 2475 m. From 2250 m to 2370 m, pyrrhotite is the carrier of the high susceptibilities. This interval is also notable because of its high remanent magnetization and high Königsberger Q-factors (= ratio of remanent magnetization to induced magnetization; also see section D.6 and chapter B).

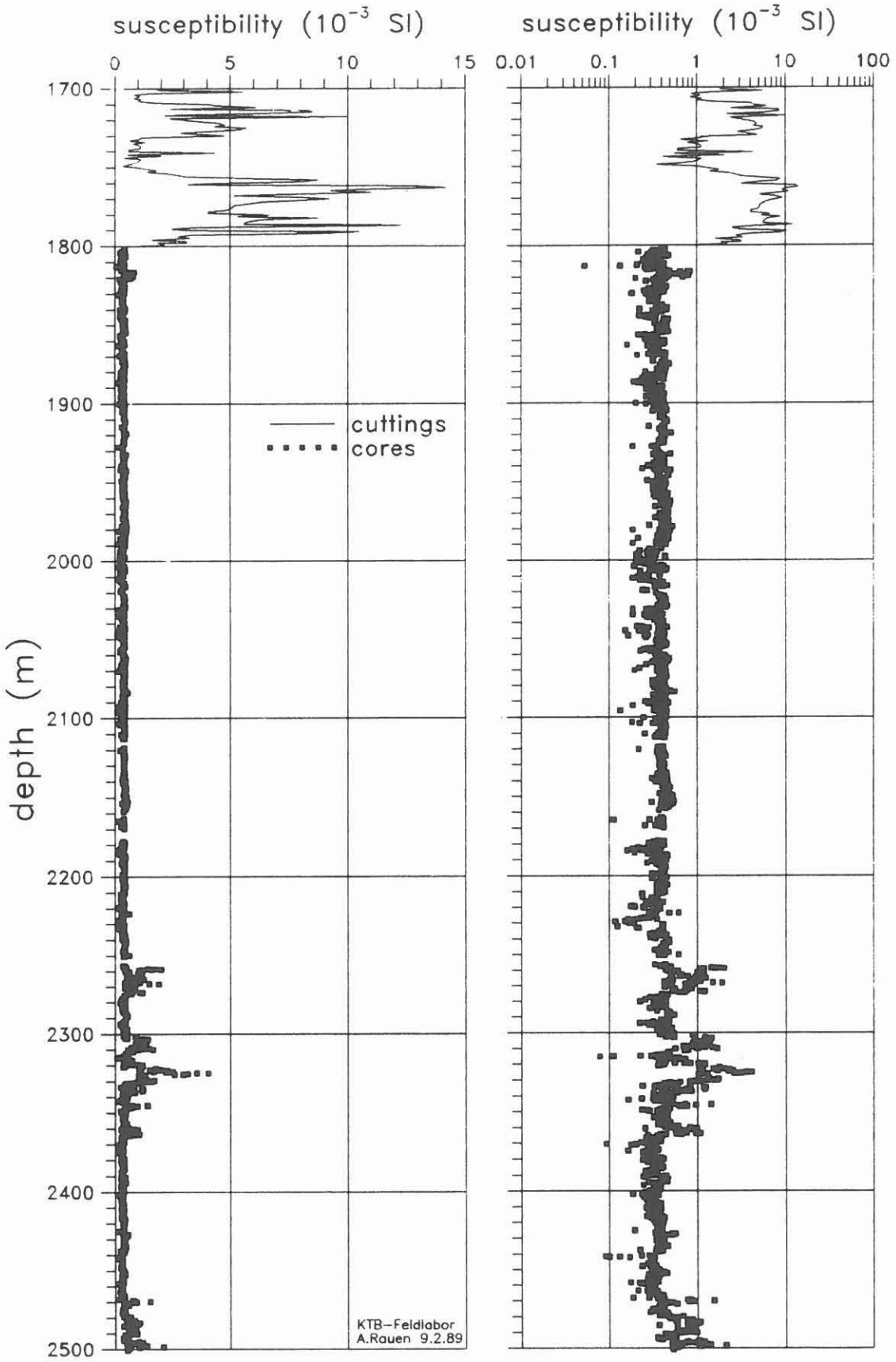

Fig. D.7.1: Susceptibility log of cores and cuttings.

The distribution of susceptibility data (Fig. D.7.2) is asymmetrical about a maximum at $0.4*10^{-3}$ SI with higher incidence at low susceptibilities. Susceptibilities in excess of $0.6*10^{-3}$ SI are relatively rare, but values of $(0.8 \text{ to } 1)*10^{-3}$ SI occur with a somewhat higher frequency corresponding to the presence of gneiss from 2250 m to 2370 m.

A near log-normal distribution of susceptibilities as observed here, has also been described by LATHAM et al. (1989).

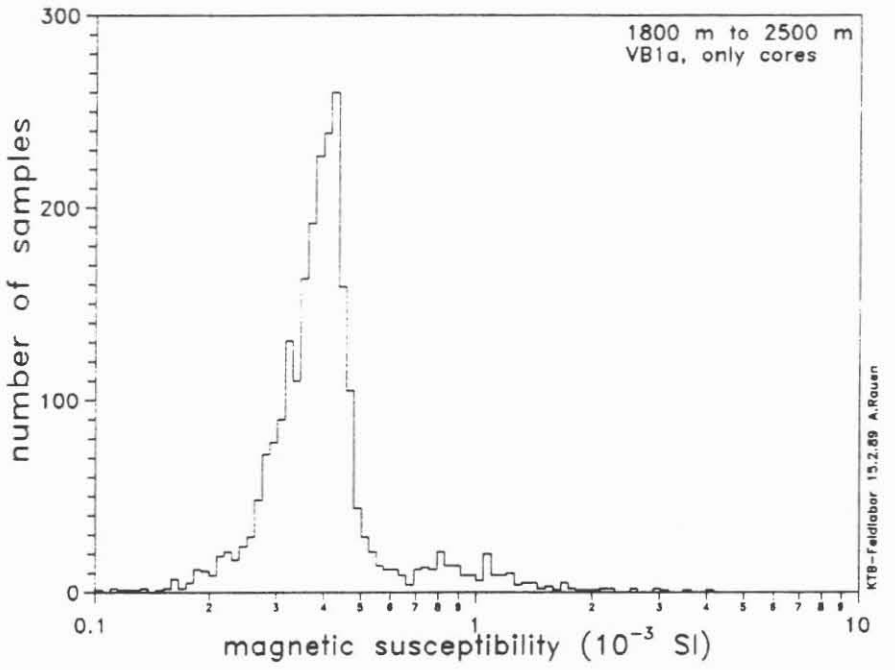

Fig. D.7.2: Frequency of observed susceptibilities of cores. 100 logarithmically scaled intervals from $(0.1 \text{ to } 10)*10^{-3}$ SI.

D.7.3 Correlation between density and susceptibility

Figure D.7.3 is a plot of density versus susceptibility data from the same depths ± 0.15 m (for selection of the values displayed, see LIPPMANN et al., 1988). Susceptibility increases with increasing density, as could be expected (see RAUEN et al., 1988). The correlation coefficient is 0.42, which is much lower than the coefficient of 0.88 from 1530 m to 1820 m (see LIPPMANN et al., 1988). The reason for this relatively low correlation coefficient is the highly susceptible gneiss previously described; this gneiss does not have a significantly higher density than the gneiss recovered earlier. Only slight density increases were observed below 2475 m.

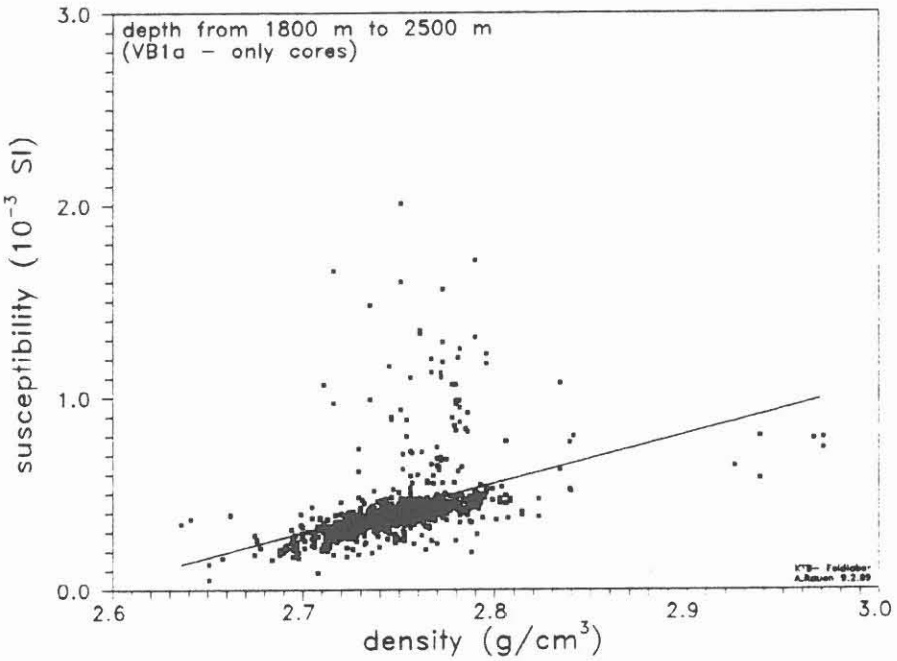

Fig. D.7.3: Susceptibility as a function of density. Measurements at identical depths ± 15 cm.

D.7.4 Correlation between VB1 and VB1a

Quantitative correlation in the overlap (start of coring at 1802 m in VB1a to base of coring at 1816 m in VB1) of the two branches of the borehole was attempted in order to detect lithological units found in the original hole (VB1), in the sidetrack (VB1a) and to quantify a possible depth difference between corresponding formations. Susceptibility was chosen as the physical parameter for such a correlation because it had the closest spacing between sampling points enabling us to compare two almost complete data sets.

An overview log (Fig. D.7.4) shows the susceptibility of cores (averaged over 20 cm) and cuttings for VB1 and VB1a from 1700 m to 2000 m. Data from cuttings are so degraded by the cavings and metal shavings from the bit and drillstring that there is no easily visible correlation. There is also no obvious correlation in the overlap range where we have susceptibility measurements for cores from both branches. Calculation of the quantitative correlation between the two branches should yield more information than visual comparison of the curves, because the complete data set is considered in the calculation rather than just certain minima and maxima.

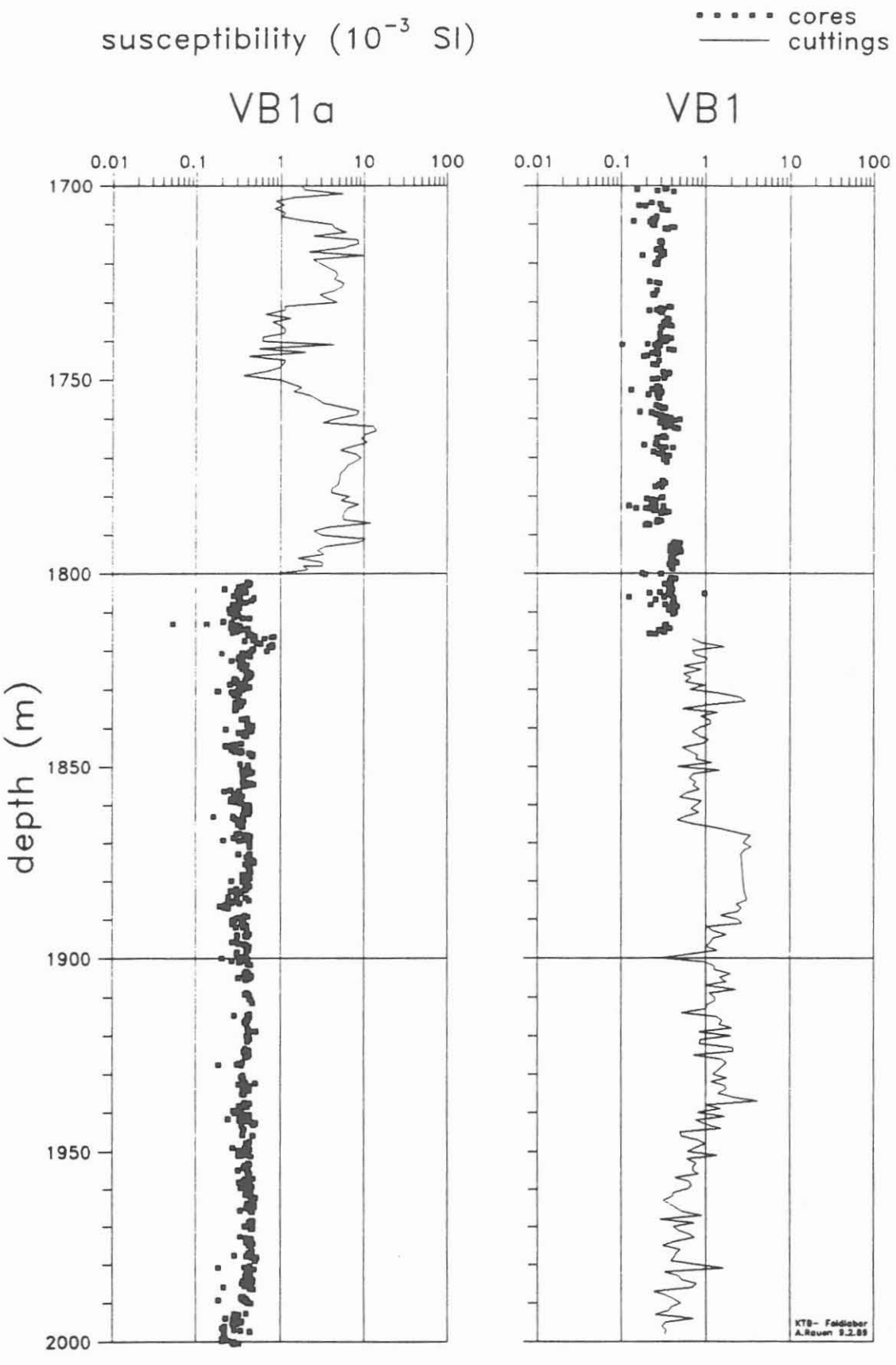

Fig. D.7.4: Susceptibilities of cores and cuttings from VB1 and VB1a.

To improve statistics, all available susceptibility data were taken into account. All data from the original data files (an example is shown in Fig. D.7.5) were stored in two files (VB1 and VB1a) with the exception of the data from the first and last 10 cm of core pieces. These were eliminated because of the strong effect of core-end geometry on the measured values. The effective sampling interval is 1.4 cm.

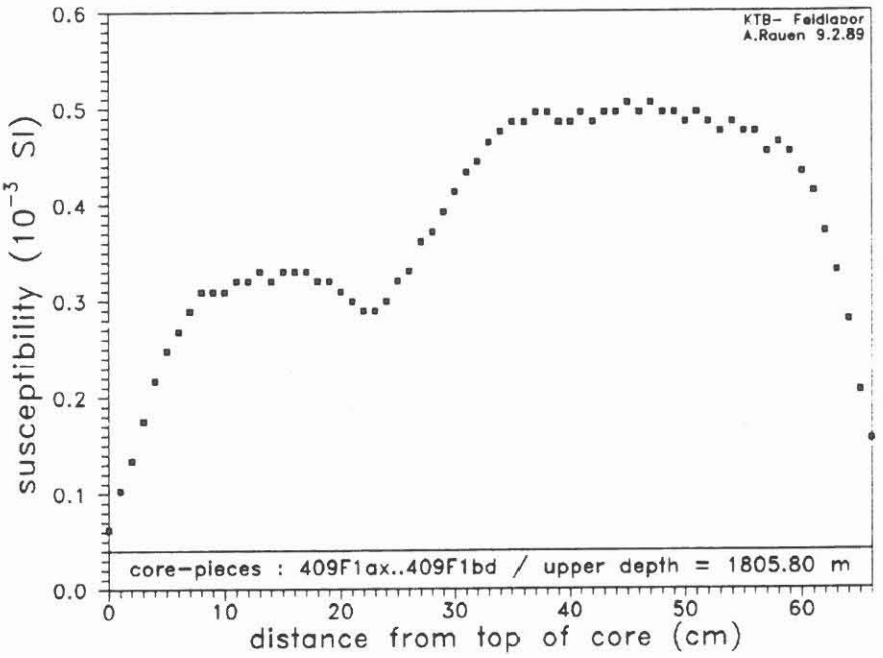

Fig. D.7.5: Susceptibility as a function of depth for a single core section.

Figure D.7.6 shows the resulting susceptibility logs for both branches of the hole in the overlap range. No outstanding differences are apparent because of the homogeneous lithology (almost all gneiss with variable mineralogy), with the exception of relatively high susceptibilities for VB1a from 1816 m to 1820 m. In that zone, VB1a penetrated amphibolite which was not encountered in VB1.

The depth range for calculation was then extended beyond the overlap range (upward for VB1, downward for VB1a) as evidence indicated that VB1a may be stratigraphically deeper than VB1 (foliation dips SSW and VB1a is south of VB1). Data from identical depths in both files was identified and used for calculation of the correlation coefficient (for calculation of cross-correlations, see GELLERT et al.,1979). The data set of VB1a was then depth-corrected, i.e. a certain value was added to the real depth, and the calculation was re-run. The results were standardized to the maximum available number of data pairs to eliminate the influence of unequally sized data sets used for the calculation.

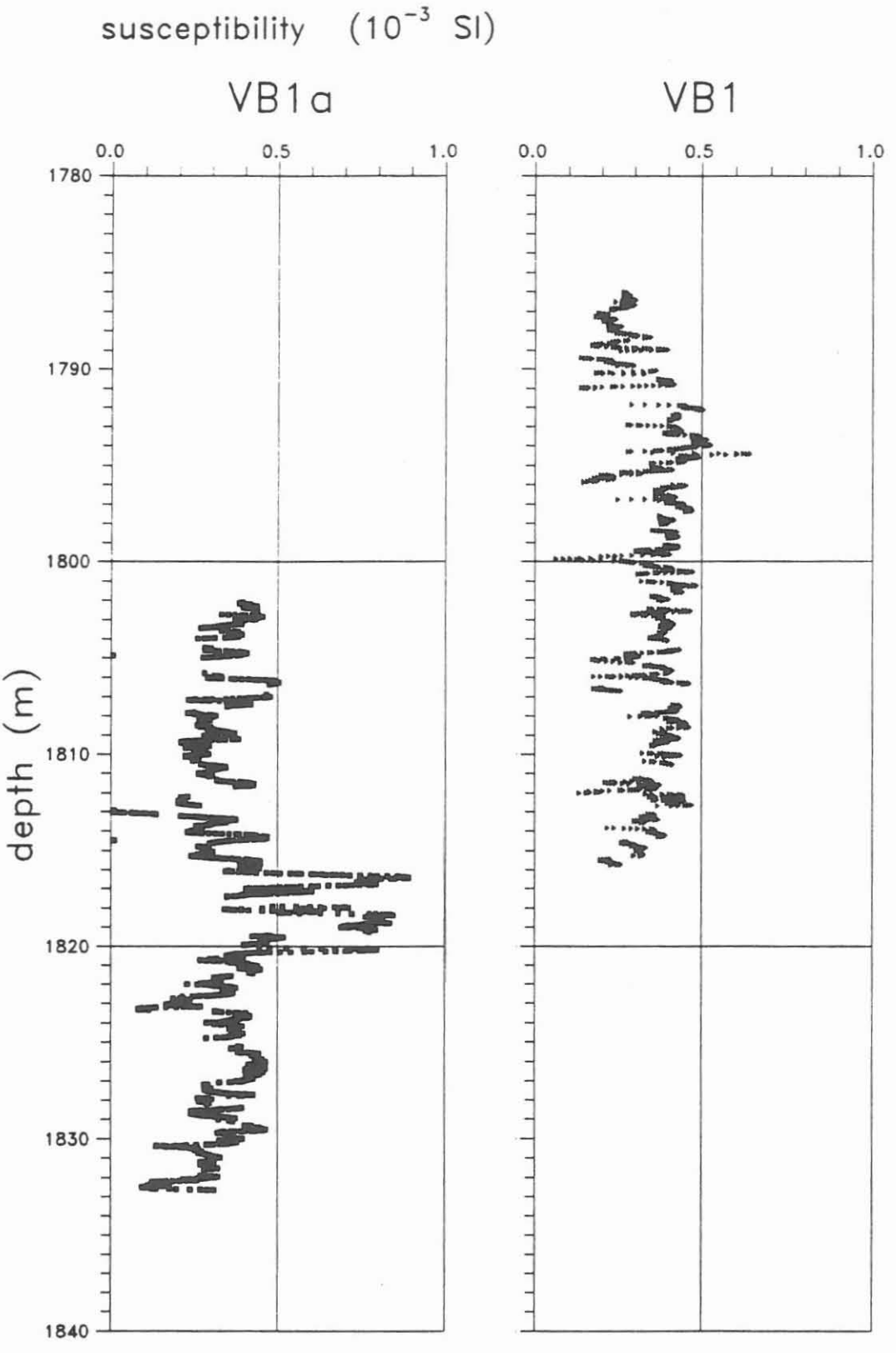

Fig. D.7.6: Comparison of susceptibilities from VB1 and VB1a using original data. Sampling interval = 1 cm. Samples taken within 10 cm of the ends of cores were not used for further calculations.

The result of the stepwise shifting of the data is shown in figure D.7.7. The calculated correlation coefficients are small (under 0.3) meaning that there is no obvious correlation between the susceptibility data from the two branches of the hole. However, a local maximum at a depth shift of -8 m may indicate the real depth difference between corresponding strata in the two holes, because geometry tends to indicate such a depth difference (see chapter B).

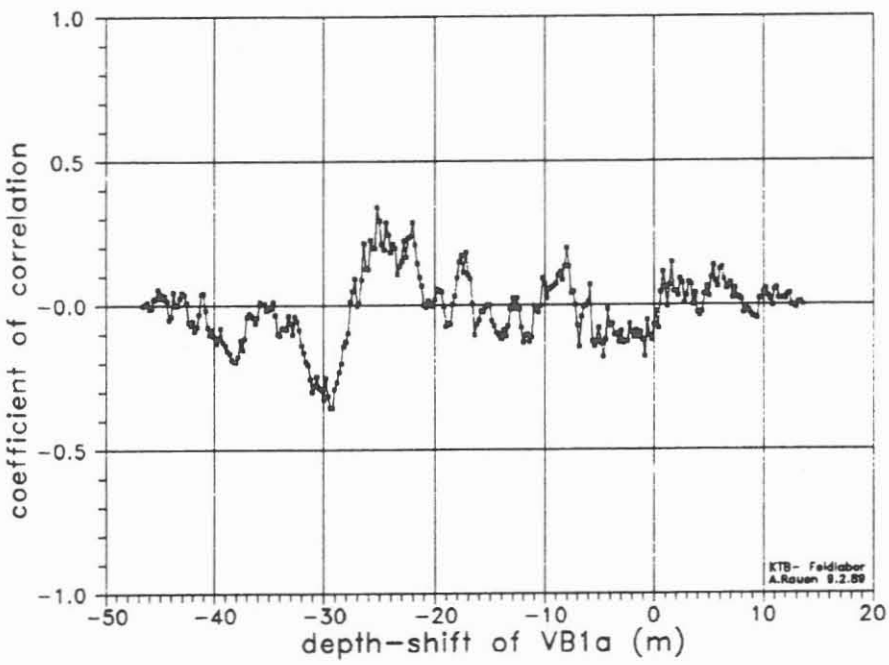

Fig. D.7.7: Correlation of VB1 / VB1a as a function of depth-shift of the VB1a-data. The entire data set of VB1, shown in figure D.7.6, was used for this calculation. Standardization to the maximum number of data points was used.

D.8 Porosity

D.8.1 Selection and preparation of the samples

A total of 516 plugs (diameter 15 mm, length approx. 30 mm) were examined between 95 and 2500 m. The plugs were cleaned, vacuum-dried for 24 hours, weighed and then saturated with distilled, degased water, which has low viscosity and a low surface tension. The samples are then stored under water for three days when the wet weight and the weight of the submerged sample are determined.

D.8.2 Measurement principles

Porosity is determined using the "Archimedies principle"; the sample is weighed under three different conditions:

1. the sample is weighed dry (= dry weight)
2. the sample is submerged in distilled water and weighed (= submerged weight)
3. the sample is taken out of the water, the remaining film of water removed from the surface (unintentionally a part of the fluid filling the pores may be removed, too) and it is weighed (= wet weight).

Determination of the submerged weight and the wet weight is repeated several times.

D.8.3 Evaluation

The three different weights can be defined as follows:

1. The weight of the dry sample, i.e. the pores are filled with air:

$$m_{dry} = d_{dry} * v_{dry}$$

2. The weight of the submerged sample, i.e. the apparent mass is:

$$m_{submerged} = (d_{matrix} - d_{pores}) * v_{matrix}$$

3. The weight of the saturated sample, i.e. the pores are completly filled with water:

$$m_{wet} = d_{matrix} * v_{matrix} + d_{pores} * v_{pores}$$

where abbreviations are as follows:

d - density
m - mass
v - volume

Porosity Φ, can be calculated from these three weights without knowing the density of the fluid:

$$\Phi = \frac{m_{wet} - m_{dry}}{m_{wet} - m_{submerged}} = \frac{d_{pores} * v_{pores}}{d_{pores} * (v_{pores} + v_{matrix})}$$

D.8.4 Results

Figure D.8.1 is a plot of porosity versus depth from 95 - 2500 m. 47 samples with porosities greater 2% are notable. These porosities, confirmed by repeated measurements, are unusually high for cristalline rocks. Joints in the samples may be the cause. The highest porosity (6%) is from a sample of garnet-amphibolite from 1315 m. Excluding these 47 samples with high porosity (probably crack-porosity), the mean porosity is 0.9% with a standard deviation of 0.4%. The minimum porosity (0.2%) is from a metagabbro sample from 1266.65 m, and the maximum porosity (1.9%) is from an amphibolite from 420.55 m.

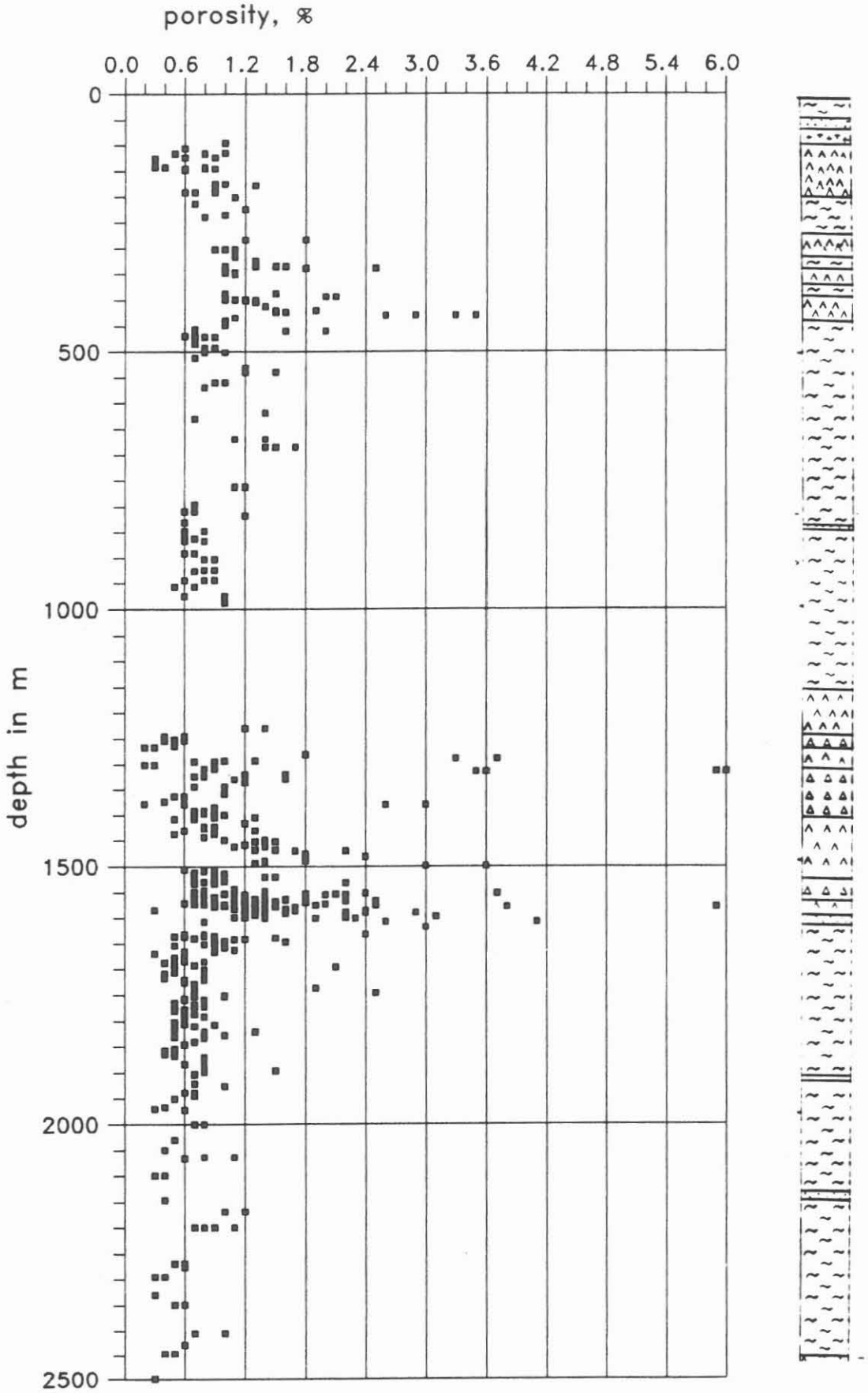

Fig. D.8.1 : Porosity. Interval : 0 - 2500 m

D.9 Permeability

D.9.1 Introduction

Most materials are somewhat "permeable" - that is, they can conduct fluids or gases. This ability is quantified by d'Arcy's equation [1]:

$$q = kA/\mu dP/dx \qquad [1]$$

where: q = flow [m^3/s] through an area, A [m^2], with a pressure gradient dP/dx [N/m^3]; the viscosity of the fluid is μ [Ns/m^2], and the permeability of the material is k [m^2].

To describe the flow of fluids in the KTB - drillhole, the in-situ permeabilities of the rocks as a function of depth are needed. The values determined in our laboratory are not in-situ permeabilities; permeability of the selected samples depends on pressure, temperature, and the composition of the fluid which is measured at other institutes. With these results, an extrapolation from laboratory data to the in-situ permeability is made. These data may then be correlated with other parameters, for example, downhole and laboratory measurements of electrical conductivity, seismic velocity and porosity.

D.9.2 Measurement Method

We plan to do permeability measurements in the field laboratory with an apparatus built at the "Institut für Tiefbohrtechnik (ITE)" at Clausthal (West Germany) but this equipment has not yet been installed at the laboratory. However, we have been carrying out some measurements in collaboration with the "Mineralogisches Institut der Universität Bonn" (West Germany). Other institutes have been measuring permeability on samples above 1500 m, and we began our measurements at roughly 2000 m.

Investigations of seismic velocities and thermal and electrical conductivity of cores have indicated that the rocks recovered so far usually show a strong anisotropy, which is closely related to the foliation of the samples. Therefore, the plugs sent to Bonn for determination of permeability, were drilled parallel and perpendicular to the foliation of the rocks.

The plugs with a diameter of 30 mm and a length of 15 ± 0.5 mm, are identified through depth and the number of the core from which they were drilled. Their orientation relative to the field laboratory reference line is also noted.

In Bonn, the samples were dried and placed in the measuring equipment developed by HUENGES (1987; Fig. D.9.1). The figure shows the cylindrical sample (black) within a glued shrink tube between porous pistons. With the help of a hydraulic ram, these pistons apply a uniaxial pressure to the sample, identical to the confining pressure, in order to reach hydrostatic conditions. The pistons are also used to conduct gases. Permeabilities were determined under hydrostatic pressures up to 70 MPa.

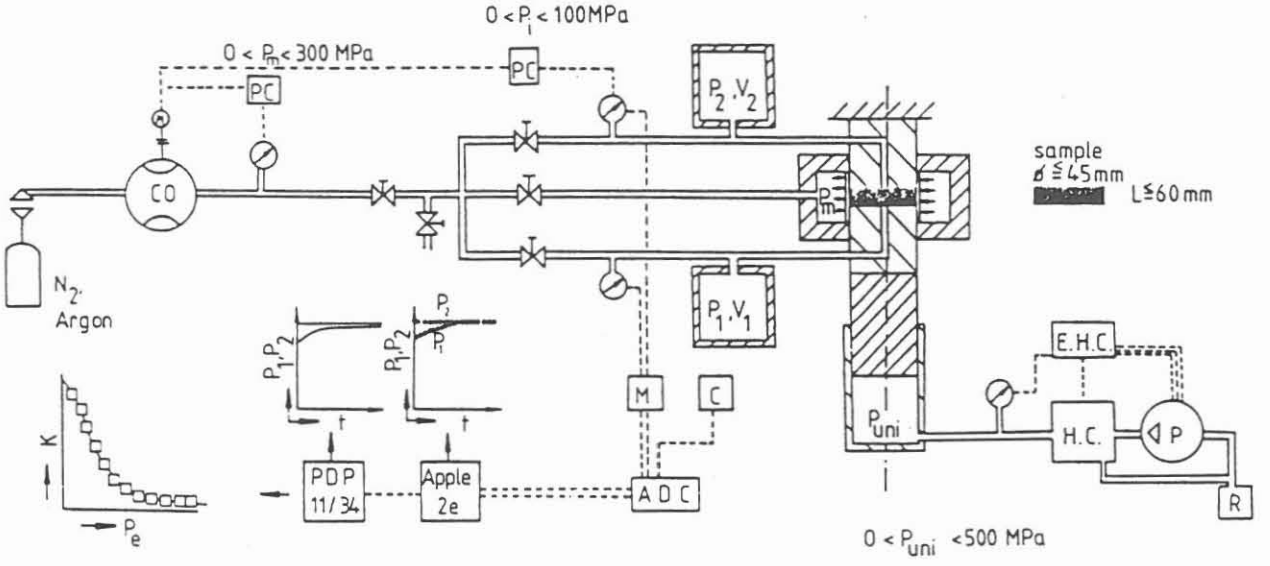

Fig. D.9.1 Experimental arrangement to measure the permeability as a function of uniaxial and confining pressure. Symboles: PC = Pressure Controller; CO = Compressor; M = Multiplexer; C = Clock; ADC = Analog-Digital-Converter; EHC = Electronic Hydraulic Controller; HC = Hydraulic Controller; P Pump, R = Reservoir (HUENGES, 1987)

Permeability is determined using the pressure transient method (see BRACE et al., 1968). The pressure on one side of the sample is kept constant at 6 MPa. At the other side of the sample there is a constant volume V_1 in which the rise of pressure (starting value: 0.1 MPa) versus time can be determined. Temperature, which has a strong influence on viscosity, was kept constant at 24 ± 1 ^{o}C .

D.9.3 Results

The results of the measurements to date (Fig. D.9.2 a - i) show an exponential increase of pressure versus time. As the confining pressure of the samples rises, the time constant of the pressure transients increases. We interprete this be results of the closing of microcracks which diminishes permeability of the samples.

The shortest time constants (Fig. D.9.2 a and i) were for two gneiss samples from 1996.96 m and 2199.32 m; both measurements were made parallel to foliation. On the other hand, two other samples (2145.89 and 2168.95 m) have very low permeability. The scatter in recorded pressure-values for these samples is due to the limited resolution of the pressure transducer (logarithmic scale!). Thus, for determination of such permeabilities either the observation time must be increased or the resolution of the pressure transducer improved.

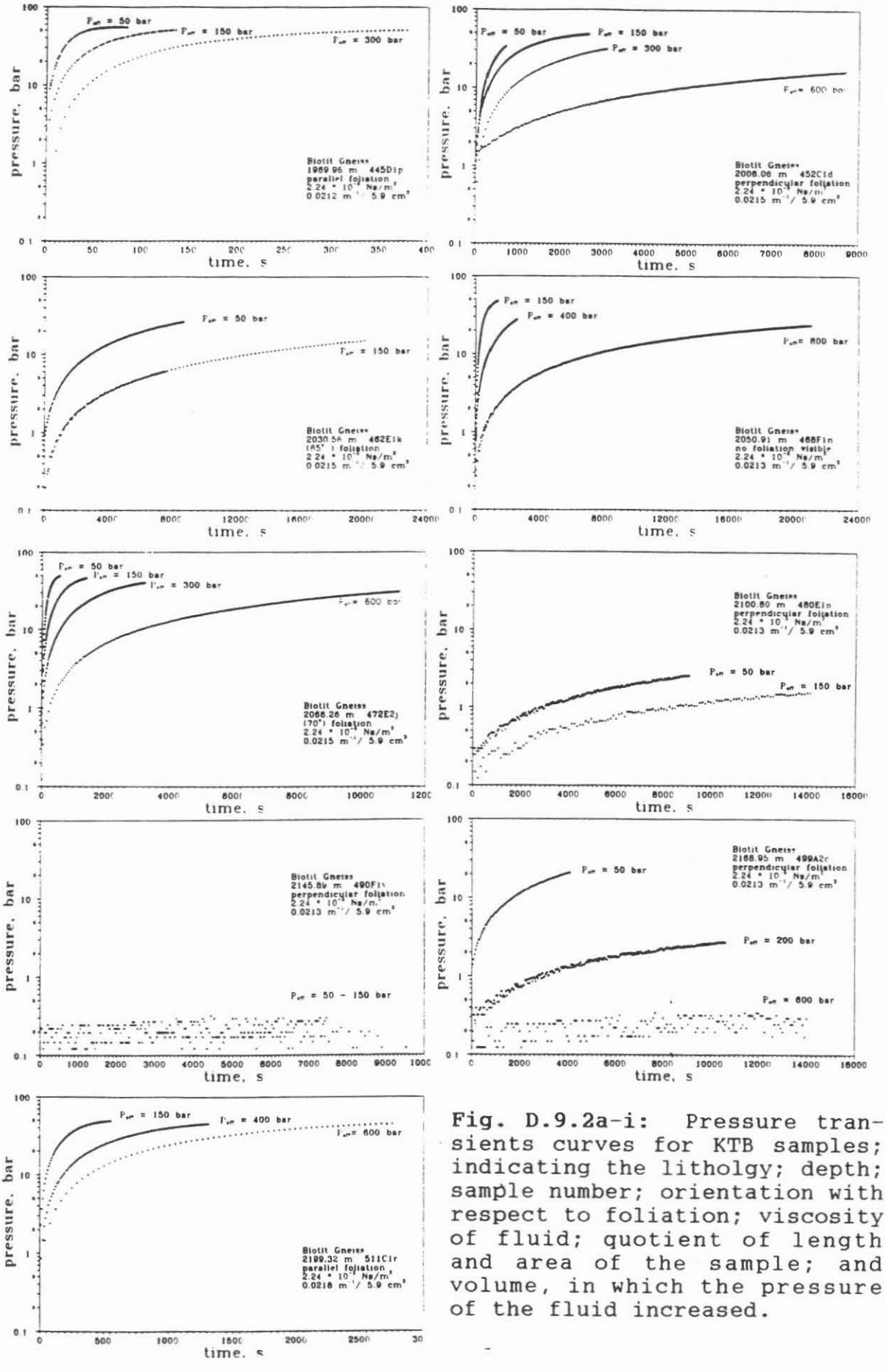

Fig. D.9.2a-i: Pressure transients curves for KTB samples; indicating the litholgy; depth; sample number; orientation with respect to foliation; viscosity of fluid; quotient of length and area of the sample; and volume, in which the pressure of the fluid increased.

D.10 Strain Retardation and Acoustic Emission

D.10.1 Introduction

The strain retardation and the occurrence of acoustic emission of different petrological rock types is investigated in the field laboratory (WOLTER et al., 1988; WOLTER & BERCKHEMER, 1989). The samples, from 1709-2500 m are mainly strongly foliated gneisses and non-textured lamprophyres. Fine-grained lamprophyres are well suited for this relaxation experiment, because of their homogeneity and isotropy.

In addition to measurement of strain retardation and numerical determination of the emission of acoustic signals, the magnitude distribution of the acoustic signals is analyzed.

Evaluation of the "Televiewer" and "Formation Micro Scanner" logs enables reorientation of core samples to their original position in the ground. Thus, information about the orientation of principal strains, and in some cases, principal stresses can be obtained.

D.10.2 Results of the strain retardation measurements

The values of the principal retarded strain (horizontal: e_1, e_2 and vertical: e_V) are given in Table D.10.1. The retarded strain histories of the samples are shown in Figures D.10.1a-f. The core samples display a wide variety of structures and textures. The paragneisses have a distinct texture and show a strong foliation. The lamprophyres are fine-grained and non-foliated, and the coarse-grained metablastic gneiss is weakly foliated.

core	depth [m]	e_1 [µm/m]	e_2 [µm/m]	e_V [µm/m]	rock type
416H1p	1842.9	265	- 1	50	paragneiss
422G1w	1870.9	398	44	92	paragneiss
464B1g	2035.8	248	65	201	paragneiss
468G1r	2051.0	312	103	147	lamprophyre
526G2u	2231.5	637	197	593	lamprophyre
588E5ac	2425.9	201	38	68	paragneiss
604A1b	2481.3	22	6	12	metablast.gneiss

Tab. D.10.1: Values of principal strain retardation

The relaxation times ($\tau_1, \tau_2, \tau_V, \tau\varnothing$) of the principal strain retardation (e_1, e_2, e_V) are given in Table D.10.2. The relaxation time is the time elapsed before 63% of the maximum strain is reached. Figures D.10.2a-f are semilogarithmic

presentations of strain versus time. The relaxation time ($\tau\phi$) is the mean value of the relaxation times (τ_1, τ_2, τ_V).

core	depth [m]	τ_1 [h]	τ_2 [h]	τ_V [h]	$\tau\phi$ [h]	rock type
416H1p	1842.9	13	11	--	12	paragneiss
422G1w	1870.9	50	40	55	48	paragneiss
464B1g	2035.8	12	15	13	13	paragneiss
468G1r	2051.0	46	36	29	37	lamprophyre
526G2u	2231.5	54	66	51	57	lamprophyre
588E5ac	2425.9	25	33	28	29	paragneiss
604A1b	2481.3	10	6	7	8	metablast. gneiss

Tab. D.10.2: Relaxation times of strain retardation

D.10.3 Measurement of acoustic emission

The retardation process is closely associated with the emission of acoustic signals. Figures D.10.3a and b represent two typical acoustic emission signals. The characteristics of the acoustic emission signals (e.g., time rate, frequency and maximum amplitude) depend on the structure and texture of the rock, the microfracturing process and the sample geometry. Table D.10.3 shows the results of the measurements of the acoustic emission. The number (n) and the relaxation time (τ_{AE}) for the acoustic emission varies for the different core samples. The dependence of the relaxation process on the material properties is dicussed in D.10.4. The relaxation time (τ_{AE}) for the acoustic emission is the time which is necessary before 63% of the total number of acoustic events are emitted. For comparision, Table D.10.3 also contains the relaxation time ($\tau\phi$) of the principal strain retardation.

core	depth [m]	AE [n]	τ_{AE} [h]	$\tau\phi$ [h]	rock type
416H1p	1842.9	--	--	12	paragneiss
422G1w	1870.9	21360	32	48	paragneiss
464B1g	2035.8	880	12	13	paragneiss
468G1r	2051.0	124	56	37	lamprophyre
526G2u	2231.5	1723	56	57	lamprophyre
588E5ac	2425.9	1710	27	29	paragneiss
604A1b	2481.3	1853	48	8	metablast.gneiss

Tab. D.10.3: Results of acoustic emission measurements

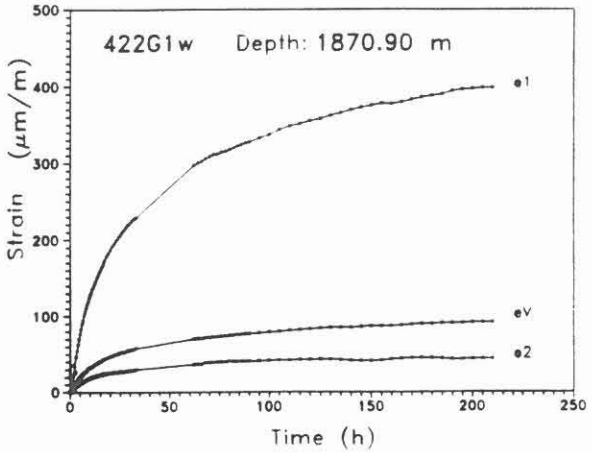

(a) Sample 422G1w

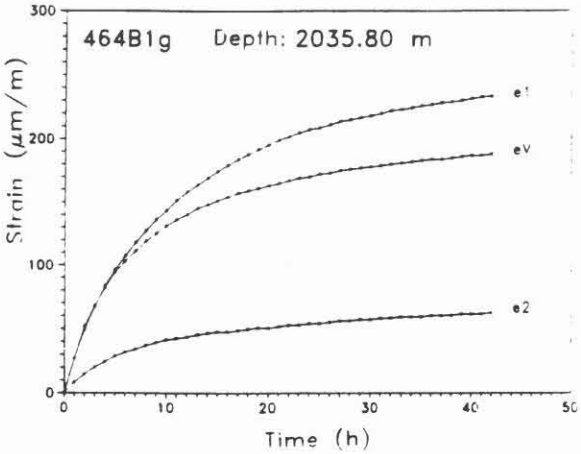

(b) Sample 464B1g

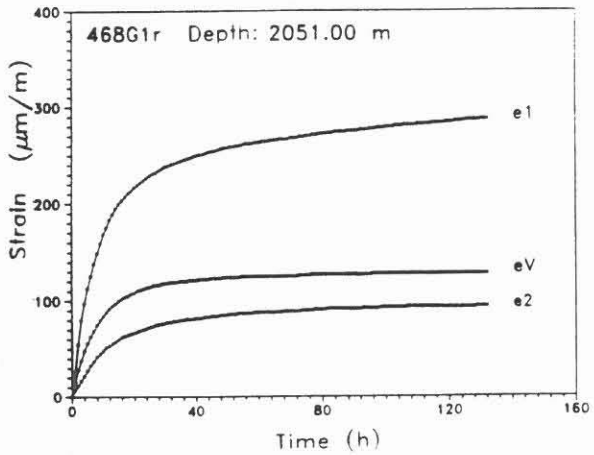

(c) Sample 468G1r

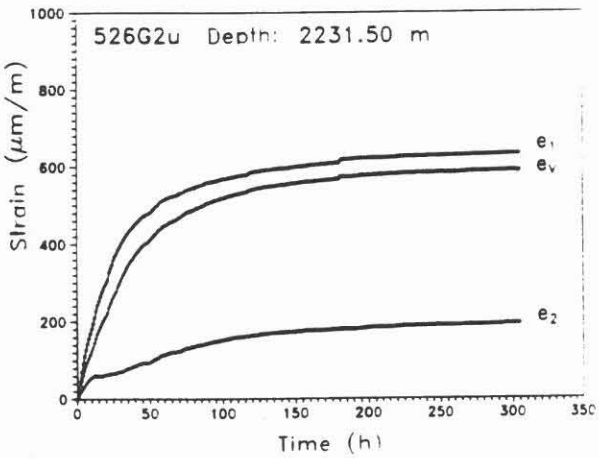

(d) Sample 526G2u

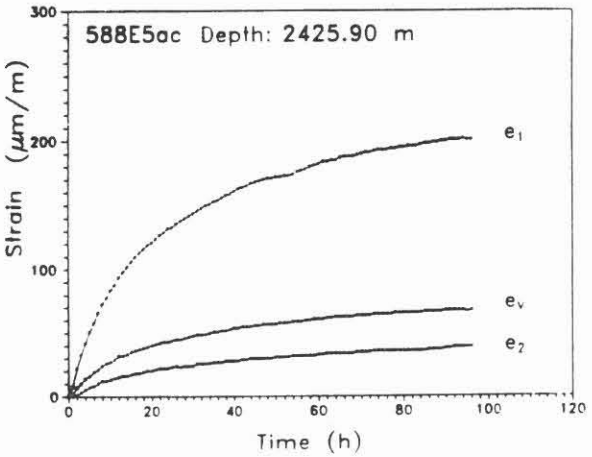

(e) Sample 588E5ac

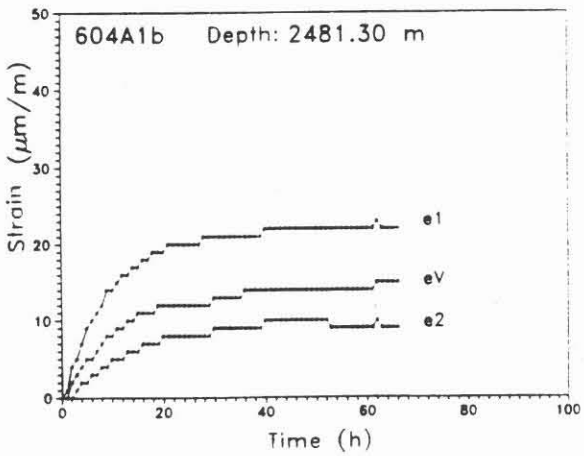

(f) Sample 604A1b

Fig. D.10.1a-f: Retarded strain histories of 6 samples (see Tab. D.10.1)

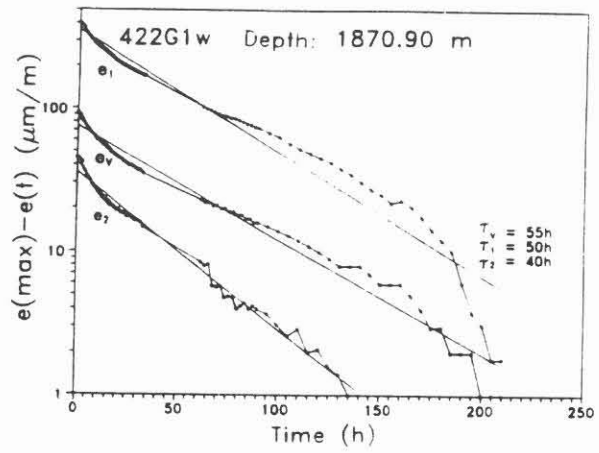

(a) Sample 422G1w

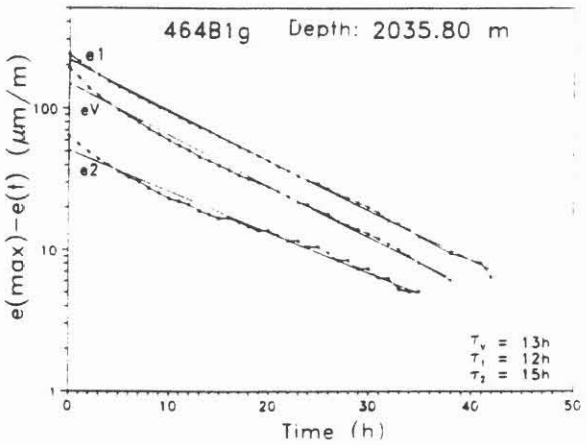

(b) Sample 464B1g

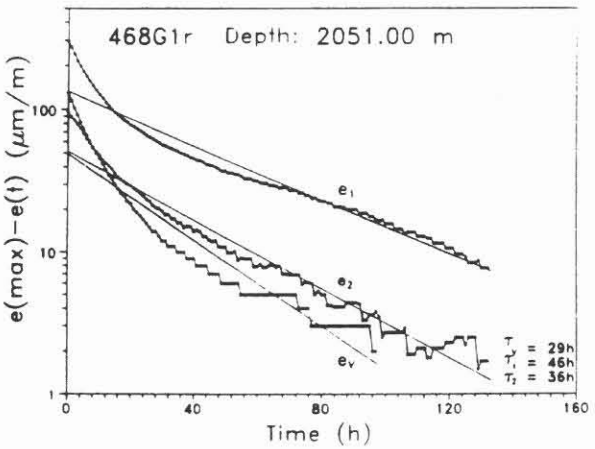

(c) Sample 468G1r

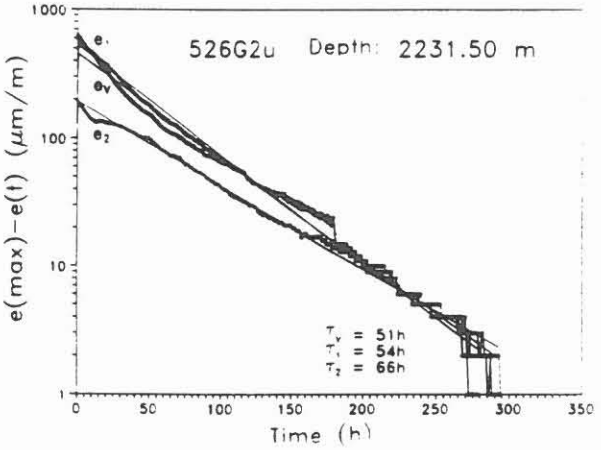

(d) Sample 526G2u

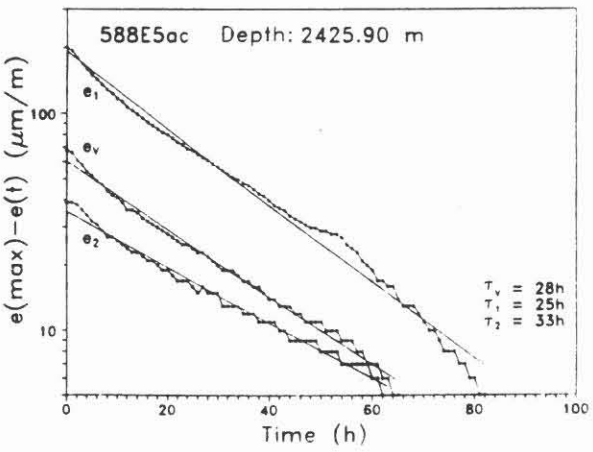

(e) Sample 588E5ac

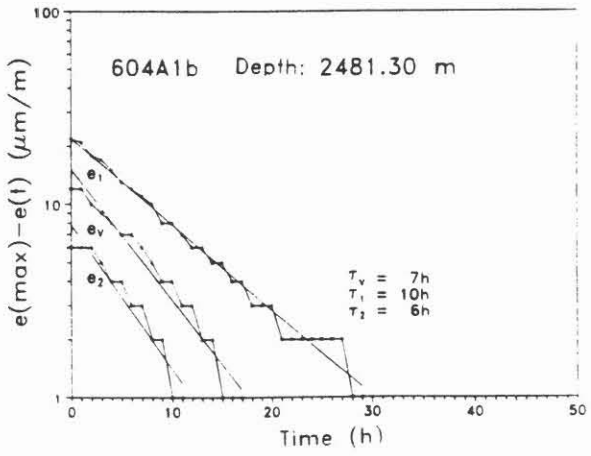

(f) Sample 604A1b

Fig. D.10.2a-f: Semilogarithmic presentations of strain versus time (see Fig.D.10.1, Tabs.D.10.1 and D.10.2)

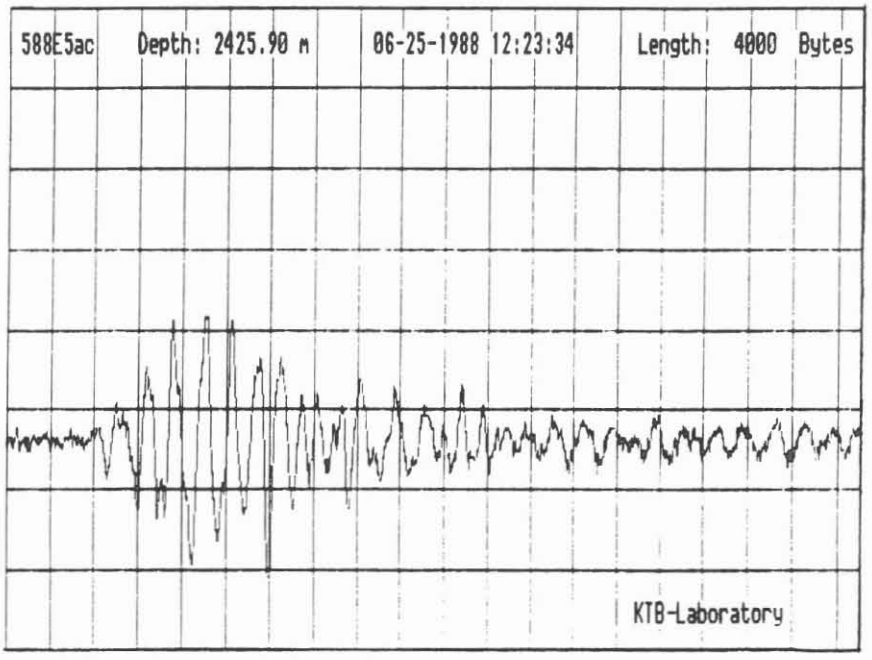

(a) Sample 588E5ac

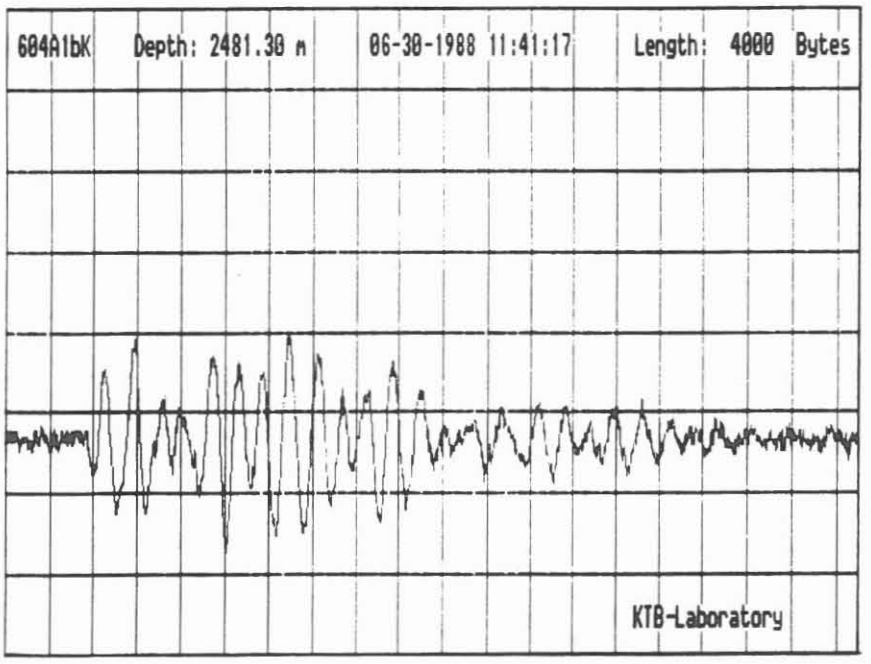

(b) Sample 604A1bk

Fig. D.10.3: Typical acoustic emission signals. One unit along the horizontal axis is 10μsec. The bandwidth of the frequency of emissions is 100-500 kHz.

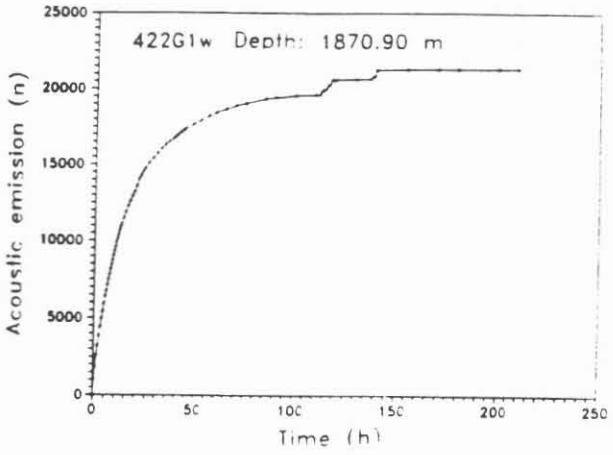

(a) Sample 422G1w

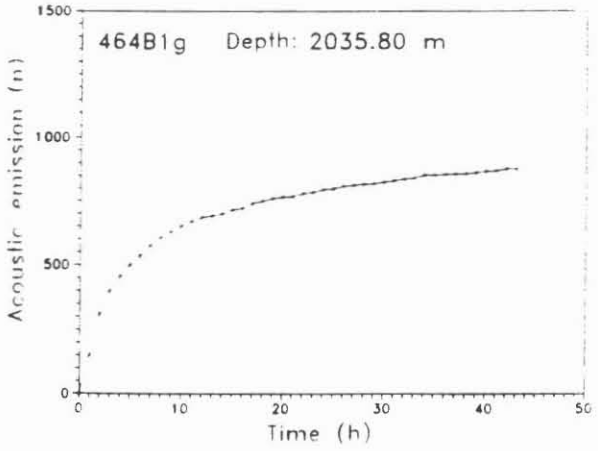

(b) Sample 464B1g

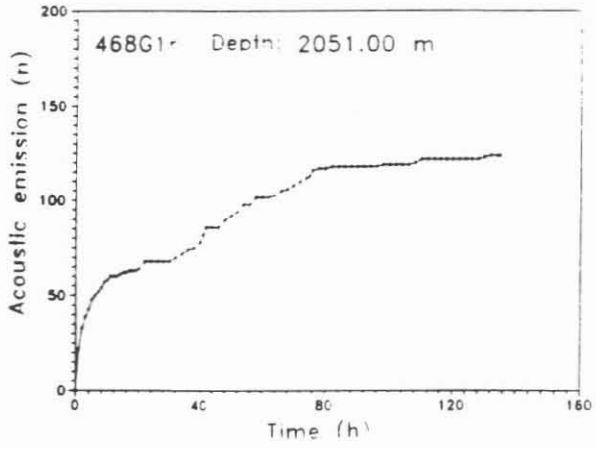

(c) Sample 468G1r

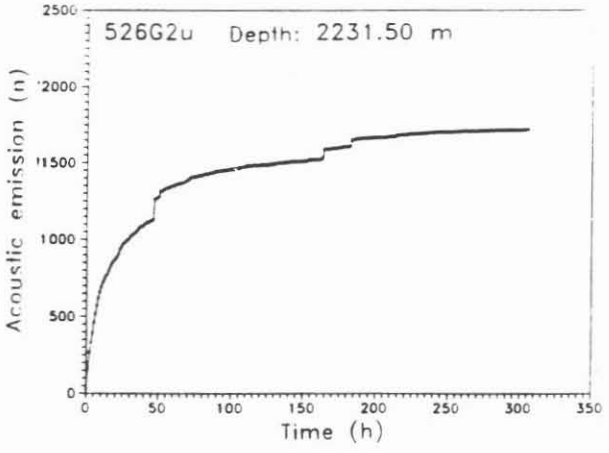

(d) Sample 526G2u

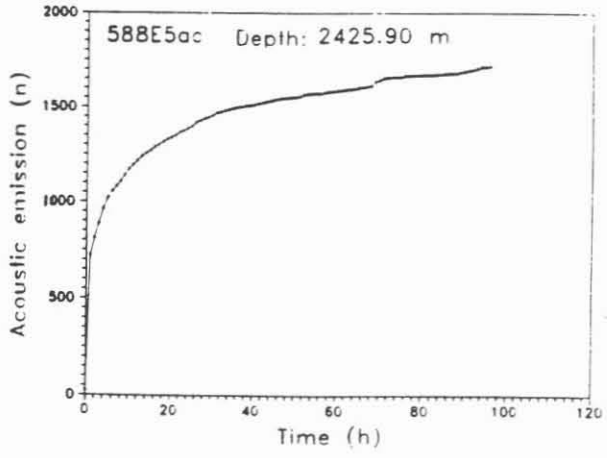

(e) Sample 588E5ac

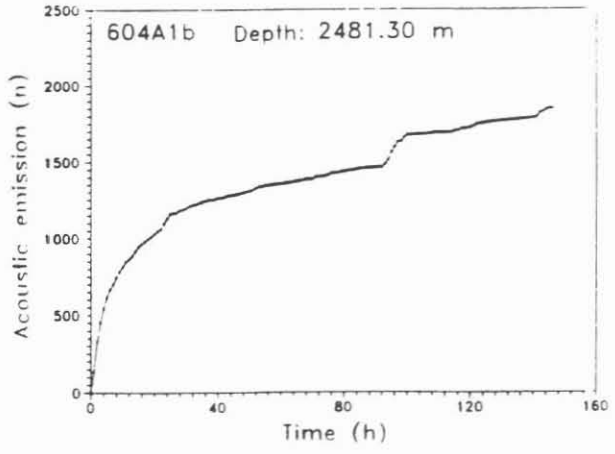

(f) Sample 604A1b

Fig. D.10.4a-f: Cumulative number of acoustic events for six core samples as a function of time

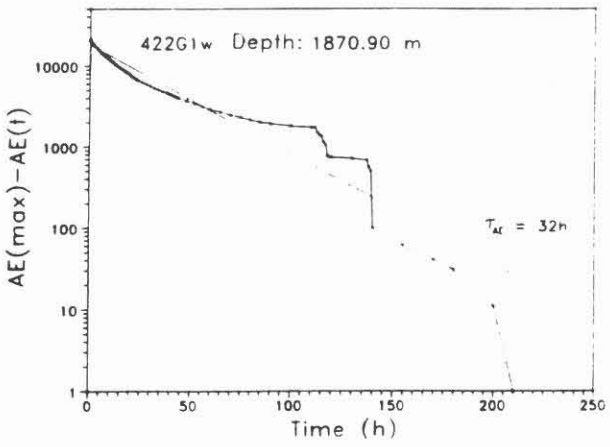

(a) Sample 422G1w

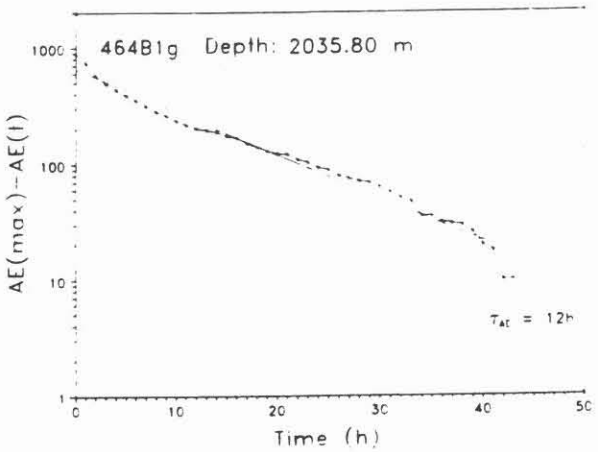

(b) Sample 464B1g

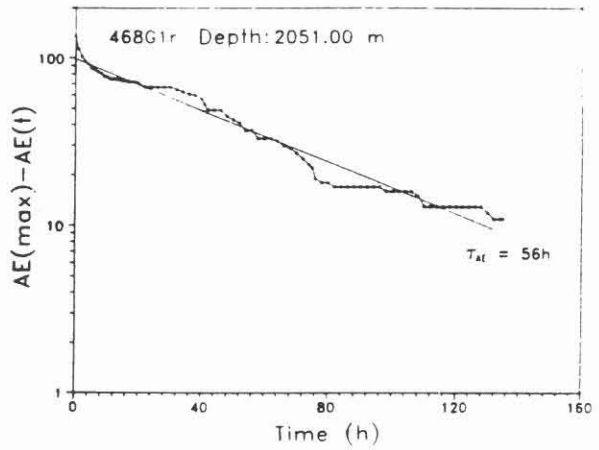

(c) Sample 468G1r

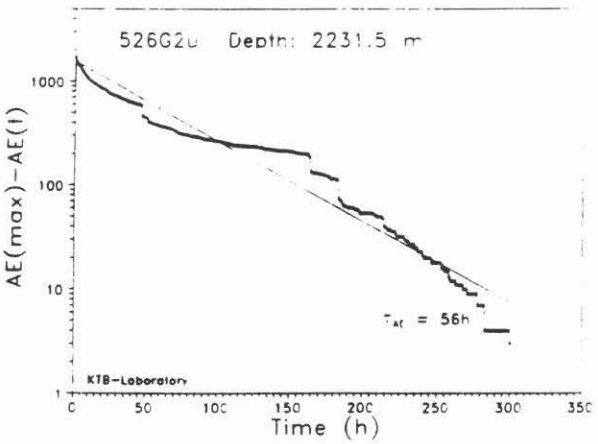

(d) Sample 526G2u

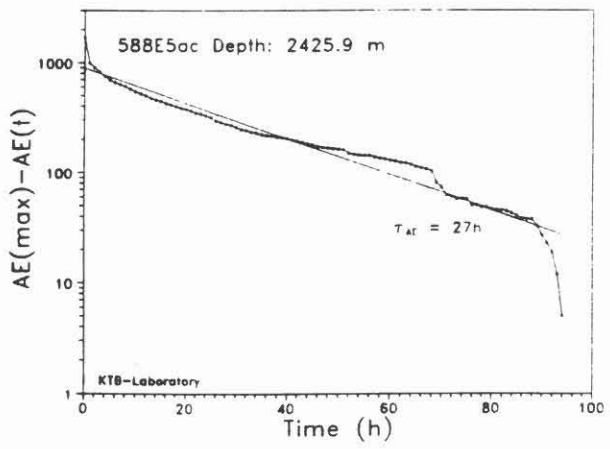

(e) Sample 588E5ac

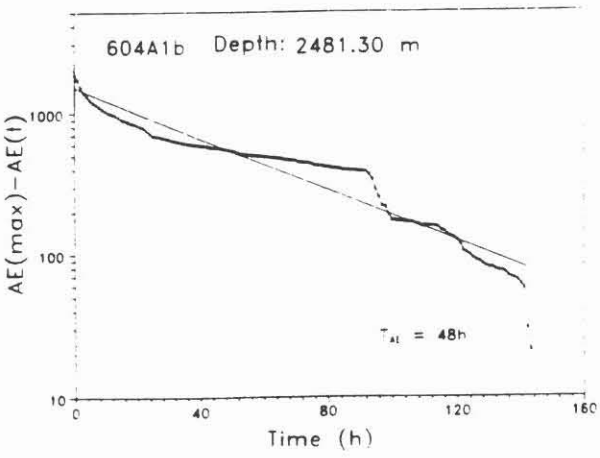

(f) Sample 604A1b

Fig. D.10.5a-f: Semilogarithmic presentations of the cumulative number of acoustic events

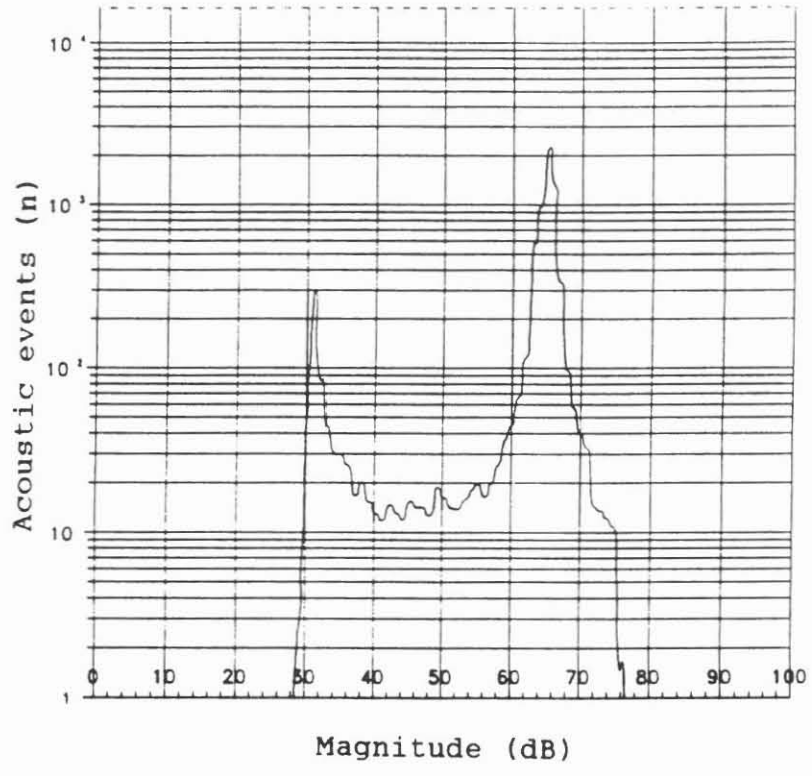

(a) Sample 588E5ac: 14107 events, 98 hours

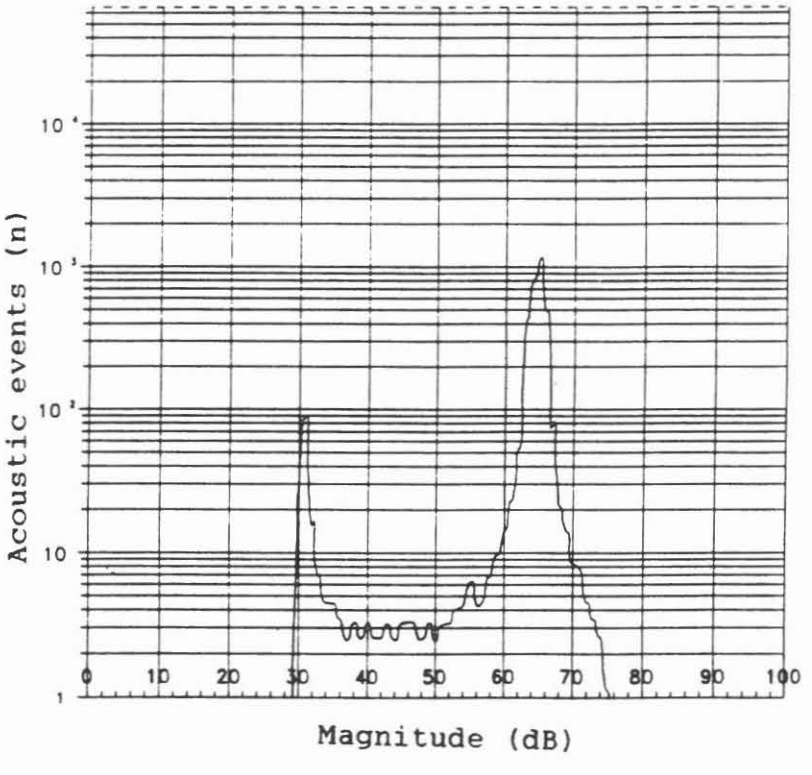

(b) Sample 604A1bk: 17818 events, 146 hours

Fig. D.10.6a and b: Distribution of the magnitude of acoustic signals

The cumulative number of acoustic events of the different core samples is shown as a function of time linearly in Figures D.10.4a-f and semilogarithmically in Figures D.10.5a-f. Some samples have nearly the same time constants (relaxation time) for acoustic emission and strain retardation. For example, core sample 464B1g has a relaxation time of 13 hours for acoustic emission and 12 hours for strain retardation. The physical association of time-dependent strain retardation and acoustic emissions is evident. Acoustic emissions are probably the expression of tensile microcracks causing volumetric expansion. The inelastic deformation (strain retardation) can, at least in part, be described by brittle fracture formation.

The magnitude of the acoustic emission signals is analyzed with the help of a distribution analyzer. Fig. D.10.6a and b give two magnitude distribution spectra of acoustic signals, recorded during the entire retardation process. Both analyses (samples 588E5ac and 604A1b) show two distinct peaks in the spectrum of the magnitude distribution at 30 and at 65 dB. Acoustic signals with lower magnitudes are dominant during the first part of the retardation process, and signals with higher magnitudes occur mainly in the second part. The reason for this phenomena is not yet clear.

D.10.4 Dependence of the retardation process on the rock properties

The dependence of the retardation process on the rock properties is demonstrated with two core samples of different lithology. Sample 526G2u (depth: 2231.5 m) is a fine-grained, non-foliated lamprophyre, with large, dark biotites (Fig. D.10.7). From microscopic inspection it appears to be homogeneous and almost isotropic.

Sample 588E5ac (depth: 2425.9 m) is a strongly foliated paragneiss. A thin section (Fig D.10.8) in the horizontal plane shows a distinct texture with well-oriented biotites and fibrolites.

The degree of anisotropy can also be measured by the azimuth dependence of the p-wave velocity at ultrasonic frequencies. The direction of the reference-line coincides with the 0°-orientation. The lamprophyre (Sample: 526G2u) is almost isotropic with respect to Vp (Fig. D.10.9a). In contrast, a distinct anisotropy is seen in the paragneiss (sample: 588E5ac, Fig. D.10.9b). The highest velocities from the paragneiss are measured in the strike of the foliation and the lowest velocities perpendicular to it.

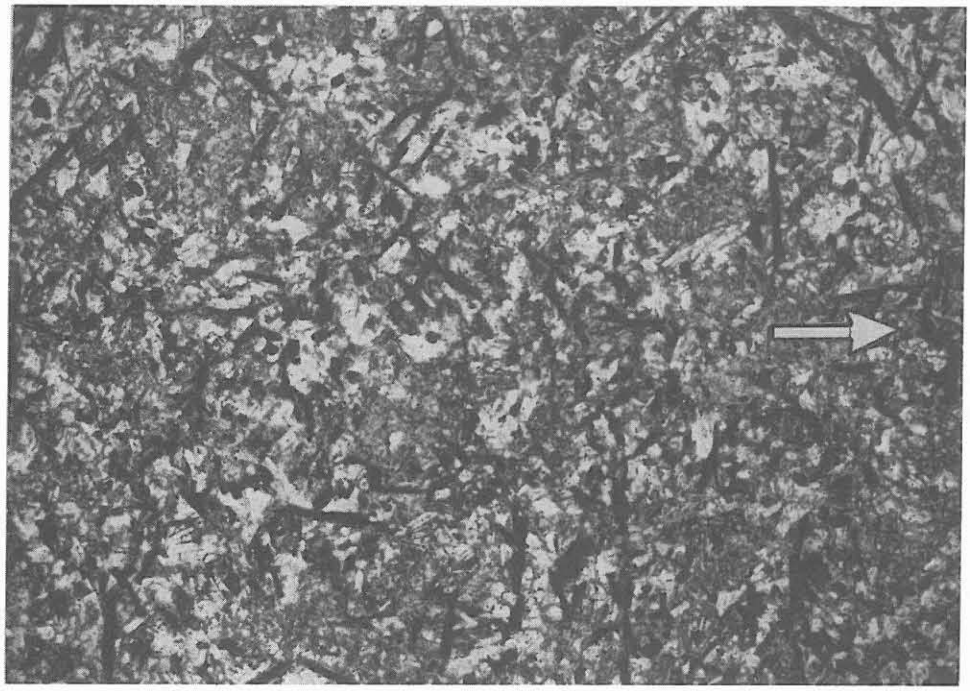

Fig. D.10.7: Fine-grained, non-foliated lamprophyre (526G2u). The arrow indicates the reference direction marked on the core. Length of the field: 6.4 mm

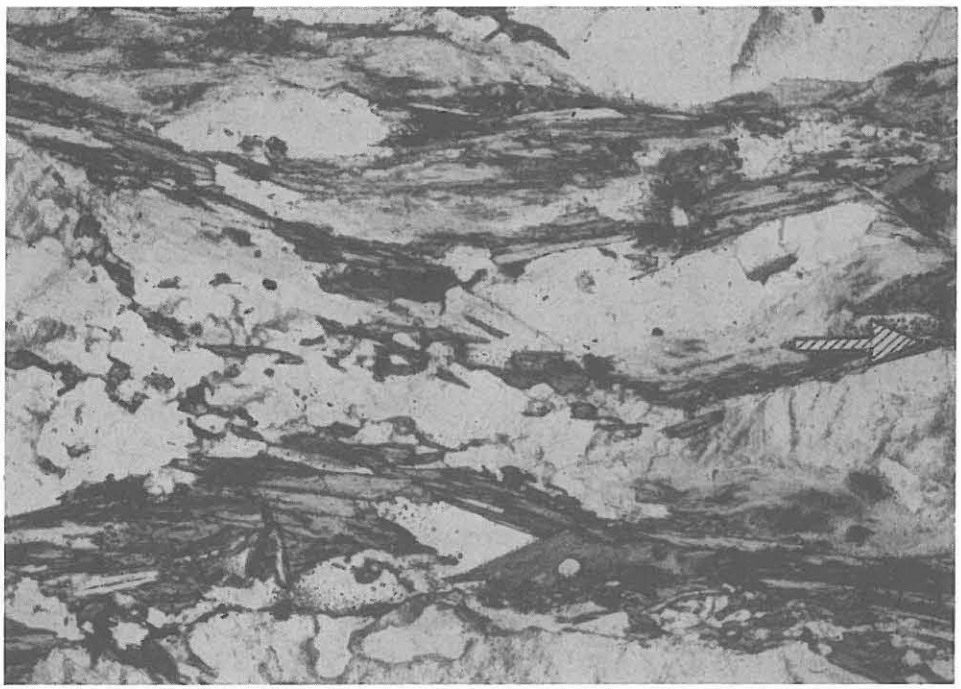

Fig. D.10.8: Foliated paragneiss with well oriented biotites and fibrolites (588E5ac). The arrow indicates the reference direction marked on the core. Length of the field: 6.4 mm.

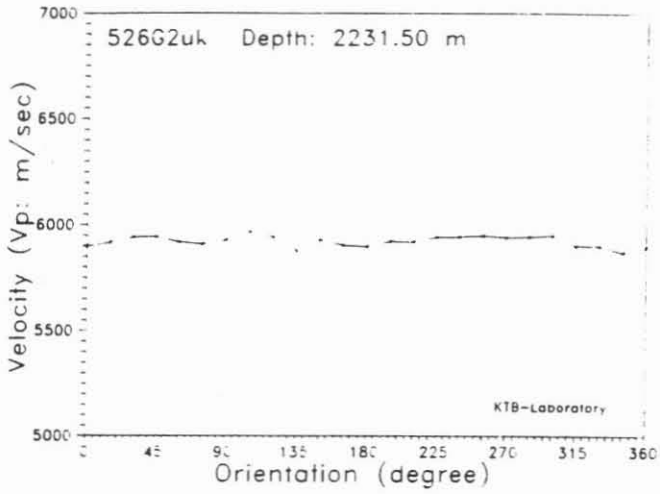

(a) Sample 526G2u: Lamprophyre

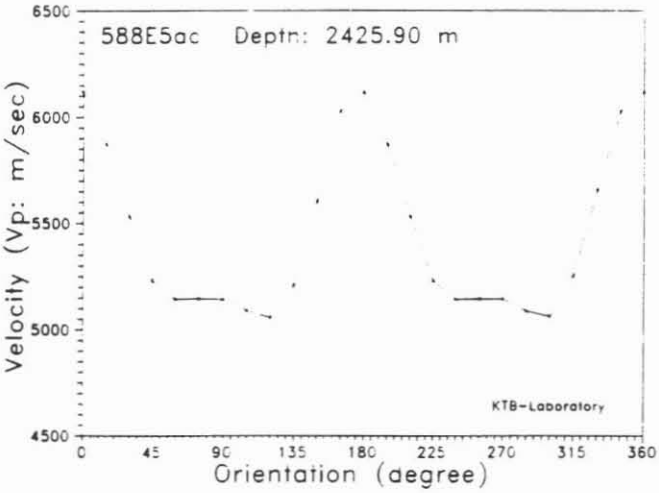

(b) Sample 588E5ac: Paragneiss

Fig. D.10.9a and b: P-wave velocity versus azimuth for two lithologically different samples.

Table D.10.4 shows the results of recovery of principal strains (e_1,e_2,e_V) and the relaxation times ($\tau\phi$,τ_{AE}) of two samples.

core	depth [m]	e_1 [µm/m]	e_2 [µm/m]	e_V [µm/m]	$\tau\phi$ [h]	τ_{AE} [h]	rock type
526G2u	2231.5	637	197	593	57	56	lamprophyre
588E5ac	2425.9	201	38	68	29	27	paragneiss

Tab. D.10.4: Results of strain recovery of two lithologically different core samples.

The magnitude of strain retardation of the lamprophyre up to 600 µm/m is about three times larger than the magnitude of strain retardation of the paragneiss, although the paragneiss comes from a depth almost 200 m deeper than the lamprophyre. There are also distinct differences of the relaxation times of the two samples.

Figures D.10.10a and b show the angle (β) of the maximum principal strain (e_1) with respect to the reference direction versus time for two samples. The orientation of e_1 is nearly stable for both samples during the entire retardation process. The reference direction coincides with the strike of the foliation of the paragneiss. The orientation of the maximum principal strain e_1 of the paragneiss is $\beta = 92°$ with respect to the reference direction. This means that the maximum principal strain is perpendicular to the foliation which is to be expected. This phenomenon has been observed in several strongly foliated core samples. The influence of the strike of foliation on the direction of retardation strain is evident.

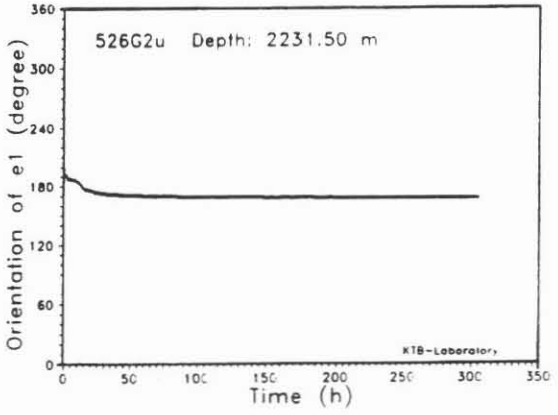

(a) Sample 526G2u: Lamprophyre

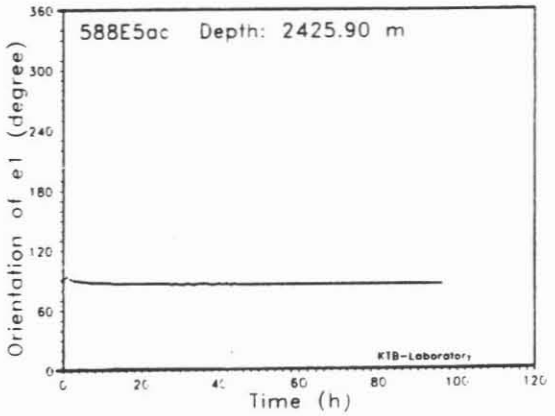

(b) Sample 588E5ac: Paragneiss

Fig. D.10.10a and b: Angle (β) of the maximum principal strain (e_1) with respect to the reference direction versus time for the two lithologically different core samples.

Rock texture appears to be a controlling factor in the retardation. Hence, the orientation of maximum principal strain retardation (e_1) of foliated rocks does not necessarily have to coincide with the orientation of the maximum horizontal stress (σ_H). On the other hand, the orientation of inelastic strain recovery in non-foliated, homogeneous and isotropic materials might well correspond to the direction of the regional stress regimes in the ground.

D.10.5 Strain and stress orientation

Evaluation of downhole "Televiewer" and "Formation Micro Scanner" logs allows us to reorient the core samples. Thus, estimates of the absolute strain directions of drill cores, and in particular cases, the directions of principal stresses can be determined. Table D.10.5 presents the orientation (Θ) of maximum horizontal principal strain of the investigated core samples.

core	depth [m]	rock type	Θ [N°E]
305D1q	1463.3	amphibolite	25° ± 10°
422G1w	1870.9	paragneiss	38° ± 10°
464B1g	2035.8	paragneiss	20° ± 10°
468G1r	2051.0	lamprophyre	172° ± 15°
526G2u	2231.5	lamprophyre	155° ± 10°
588E5ac	2425.9	paragneiss	20° ± 10°
604A1b	2481.3	metablast.gneiss	80° ± 20°

Tab. D.10.5: Orientation of maximum horizontal principal strain

The gneiss and amphibolite both have a distinct foliation, with a strike of N110°-130°E. The orientation of the maximum retarded strain is ± perpendicular to this foliation (N20°-38°E ± 10°).

If the direction of strain retardation in homogeneous and isotropic rocks corresponds to the stress direction in the ground, we can deduce the following: The direction of the maximum horizontal retarded strain of the fine-grained homogenous and nearly isotropic lamprophyre (526G2u) is identical to the direction of maximum horizontal in situ stress. This means that in the area of the drillhole, the direction of the maximum horizontal stress is NW-SE (mean value: N163°E ± 20°) at a depth of 2231 and 2426 m. This result is almost in accordance with the general maximum horizontal stress of Central Europe, which is a known NW-SE trending direction for σ_H (BAUMANN, 1981; KLEIN & BARR, 1986).

D.10.6 Calculation of the magnitude of principal stress

According to a modern viscoelastic theory (BLANTON, 1983), it is possible to calculate the magnitudes of principal in situ stresses from inelastic strain recovery. The assumptions which must be made are:

- the rock is homogeneous and linearly viscoelastic
- the rock is isotropic
- the wellbore is vertical
- the vertical stress is equal to the weight of the overburden and is a principal stress.

The magnitudes of the two principal horizontal stresses, σ_H and σ_h can be calculated from the different principal strain magnitudes (e_1, e_2, e_V), if the Poisson`s ratio (ν) and the overburden stress (σ_V) are known:

$$\sigma_H = \sigma_V \frac{(1-\nu)e_1 + \nu(e_2 + e_V)}{(1-\nu)e_V + \nu(e_1 + e_2)}$$

$$\sigma_h = \sigma_V \frac{(1-\nu)e_2 + \nu(e_1 + e_V)}{(1-\nu)e_V + \nu(e_2 + e_1)}$$

The values of strain retardation for two homogeneous lamprophyre samples (468G1r and 526G2u) are suitable for calculation of the principal stresses. Poisson`s ratio is assumed to be 0.30 and the average density of the overburden is 2.82 g/cm^3. The results of the calculated principal stresses are listed in Table D.10.6, and are presented in Figures D.10.11a and b.

core	depth [m]	σ_H [MPa]	σ_h [MPa]	σ_V [MPa]
468G1r	2051.0	73	52	57
526G2u	2231.5	63	47	61

Tab. D.10.6: Calculated principal stresses for two lamprophyre samples.

The apparent time dependence of σ reflects the deviation of the actual rheological behaviour of the two lamprophyric rocks from an ideal viscoelastic material. σ_V is the intermediate principal stress, σ_H is about 1.4 σ_h.

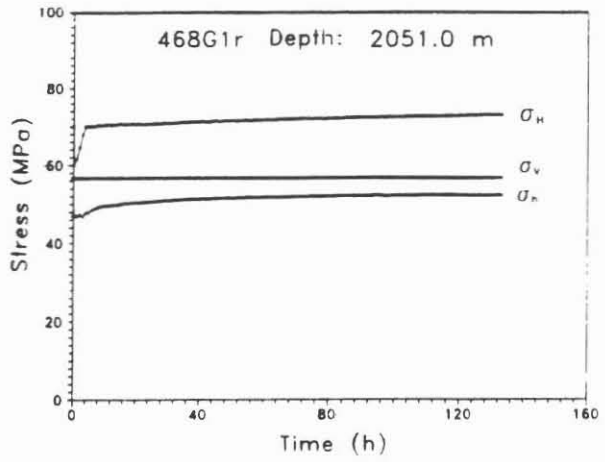

(a) Sample 468G1r

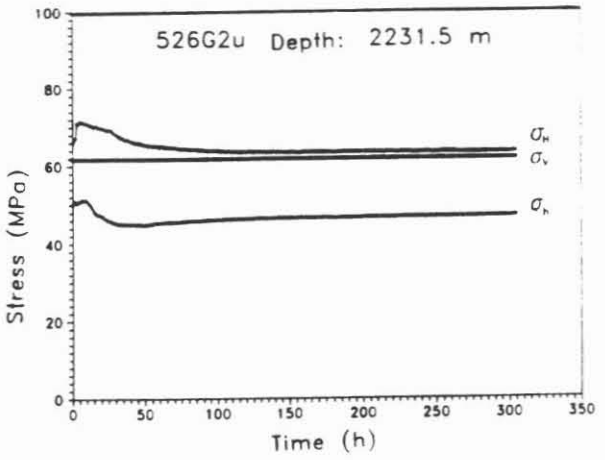

(b) Sample 526G2u

Fig. D.10.11a and b: Calculated principal stresses for two lamprophyre samples

D.10.7 Conclusions

Core samples of different lithology have distinct differences in the time-dependent strain retardation process (e.g., strain magnitude, relaxation time and characteristics of the acoustic emission). The strain rate and the occurrence of acoustic emission decreases exponentially with time. Acoustic emisssion provides clear evidence for volumetric expansion by tensile microcrack formation. If the core sample is a homogeneous, isotropic, linear viscoelastic material, then the values of recovery strain are suitable for calculation of the magnitudes and directions of in situ stresses.

D.11 Acknowledgement

We would like to thank the technicians who made most of the measurements used for the investigations: Robert Fürnrohr, Michaela Jäger, Adelheid Kick and Hubert Köstler.

Permeability measurements were done at the "Institut für Mineralogie" at the University of Bonn under Dr. G. Nover and Prof. Dr. G. Will by order of the "Niedersächsisches Landesamt für Bodenforschung".

We thank Dr. Eisenblätter (Batelle-Institut, Frankfurt) who made it possible to determine the magnitude of acoustic emissions by means of a distribution analyzer.

The authors are grateful to many other colleagues of the geophysical institutes of the universities of Berlin, Frankfurt and Munich, not mentioned here, for their support and cooperation.

We would also like to thank Prof. R. Emmermann, Dr. J. Lauterjung, Dr. H. G. Dietrich, Dr. M. Heinisch, Prof. Soffel and Th. Wöhrl for their excellent suggestions.

The authors wish to thank the Deutsche Forschungsgemeinschaft (DFG) and especially the DFG Priority Program of the Continental Deep Drilling Project and the Niedersächsisches Landesamt für Bodenforschung for financial support of our investigations.

Thanks to Prof. P. Robinson and Mrs. Horn for the excellent revising of the english text.

D.12 References

ADE-HALL, J.M. & H.P. JOHNSON (1976): Palaeomagnetism of basalts.- Leg 34, Init. Rep. Deep Sea Drill. Proj., 34: 513-532.

BADER, K. & G. STETTNER (1988): Zur Ursache der aeromagnetischen Anomalien von Windischeschenbach und Vohenstrauß (Nordost-Bayern).- Geol. Jb., E 43, (im Druck).

BAUMANN, H. (1981): Regional stress field and rifting in western Europe.- Tectonophysics, 73: 105-111, Amsterdam (Springer).

BLANTON, T.L. (1983): The relation between recovery deformation and in situ stress magnitudes. - Symp., SPE / DOE, 11624: 213-218, Denver.

BRACE, W.F., WALSH, J.B. & W.T. FRANGOS (1968): Permeability of Granite Under High Pressure. - J. Geophys. Res., 73: 2225-2236.

BÜCKER, Ch., EIGNER, K.-H., RAUCH, E., RAUEN, A., WIENAND, J. & K.E. WOLTER (1988): Tiefbohrung KTB Oberpfalz VB, Ergebnisse der geowissenschaftlichen Bohrungsbearbeitung im KTB-Feldlabor, Teufenbereich 0-480 m: D. Geophysik.- KTB-Report 88-1: D1-D42, Hannover.

BURMESTER, R.F. (1977): Origin and stability of drilling induced remanence.-Geophys. J. R. astr. Soc., 48: 1-14.

COLLINSON, D.W.(1983): Methods in Rock Magnetism and Palaeomagnetism. - 503 p., Chapman & Hall, London, New York.

DRAXLER, J. K. & R. HÄNEL (1988a): Grundlagenforschung und Bohrlochgeophysik, Bohrlochmessungen in der KTB-Oberpfalz VB, Intervall 487.5-1529.4 m. - KTB-Report 88-4, Hannover.

DRAXLER, J. K. & R. HÄNEL (1988b): Grundlagenforschung und Bohrlochgeophysik, Bohrlochmessungen in der KTB-Oberpfalz VB, Intervall 1529.4-3009.7 m. - KTB-Report 88-7, Hannover.

DUCKERT, J. (1961): Die Bestimmung der elektrischen Eigenschaften von Gesteinsproben mittels einer 4-Punkt-Methode. - Diplomarbeit, Inst. f. Allg. u. Angew. Geophysik der Universität München (unveröffentl.).

ERBAS, K. (1985): Bestimmung der Wärmeleitfähigkeit von Festkörpern mit einer Halbraum-Linien-Quellen-Apparatur - Diplomarbeit, Inst. f. Angew. Geophysik, T.U. Berlin (unveröffentl.).

GELLERT, W., KÜSTNER, H., HELLWICH, M. & H. KÄSTNER (1979): Kleine Enzyklopädie der Mathematik. - 2.Aufl., VEB-Verlag Enzyklopädie, Leipzig.

GRUBBE, K., HAENEL, R. & G. ZOTH (1983): Determination of the vertical component of thermal conductivity by line source methodes. - Zbl. Geol. Paläont. Teil I; H.1/2: 49-56, Stuttgart.

HAACK, U. (1982): Radioactivity of Rocks. In: Angenheister, G. (ed), Landolt-Börnstein, New Ser. Bd. V, p.433-481.

HEINSCHILD, H.J., HOMANN, D., KAMM, H., & H.-J. WELKER (1988): KTB Oberpfalz VB, Ergebnisse der geowissenschaftlichen Bohrungsbearbeitung im KTB-Feldlabor, Spülungsanalytik bis 480 m. - KTB-Report 88-1: C61-C73, Hannover.

HUENGES, E. (1987): Messung der Permeabilität von niedrigpermeablen Gesteinsproben unter Drücken bis 4kbar und ihre Beziehung zu Kompressibilität, Porosität und komplexen elektrischem Widerstand.- Diss., Rheinische Friedrich-Wilhelms-Universität, Bonn.

KEYSSNER, S., MASSALSKY, T., MÜLLER, H., RÖHR, CH., GRAUP, G., & W. HACKER (1988): Tiefbohrung KTB-Oberpfalz VB, Ergebnisse der geowissenschaftlichen Bohrungsbearbeitung im KTB-Feldlabor (Windischeschenbach), Teufenbereich von 992 - 1530 m. - KTB-Report 88-6: B1-B88, Hannover.

KIEFER, H. & W. KOELZER (1987): Strahlen und Strahlenschutz.- 2. Aufl.,(Springer) Berlin, Heidelberg.

KLEIN, R.J. & M.V. BARR (1986): Regional State of Stress in Western Europe. - Proc. Int. Symp. on Rock Stresses and Rock Stress Measurements / Stockholm, 1.-3.Sept. 1986: 33-44.

KÖNIG, R. (1988): Bestimmung der Anisotropie der Wärmeleitfähigkeit von Gesteinen durch Labormessungen und Modellrechnungen; Diplomarbeit, Geophysikal. Inst. der Universität Karlsruhe (unveröffentl.).

KRISTIANSEN, J. (1982): The Transient Cylindrical Probe Method for Determination of Thermal Parameters of Earth Materials. - Thesis; Department of Geology, Aarhus, Denmark.

LATHAM, A.G., HARDING, K.L., LAPOINTE, P., MORRIS, W.A. & S.J. BALCH (1989): On the lognormal distribution of oxides in igneous rocks, using magnetic susceptibility as aproxy for oxide mineral concentration.- Geophys.J., Vol. 96, No. 1.

LIPPMANN, E., HUENGES, E., BÜCKER, Ch., WIENAND, J., WOLTER, K.E. & A. RAUEN (1988): Tiefbohrung KTB Oberpfalz VB, Ergebnisse der geowissenschaftlichen Bohrungsbearbeitung im KTB-Feldlabor (Windischeschenbach), Teufenbereich von 1530 bis 2000 m: D. Geophysik. - KTB-Report 88-9: D1-D60, Hannover.

OEZDEMIR, Ö., DUNLOP, D.J., REID, B. and H. HYODO (1988): An early Proterozoic VGP from an oriented drillcore into the Precambrian basement of Southern Alberta.- Geoph. J., 95: 69-78.

PETERSEN, N. (1978): Glomar Challenger Drillings: The Magnetic Field Produced By The Drill And Drill String.- Initial Reports of the Deep Sea Drilling Project, Volume XLVI, Washington (US Government Printing Office).

POHL, J. (1989): mündliche Mitteilung, Inst. f. Allg. und Angew. Geophysik, München.

PUCHER, R. (1986): Interpretation der magnetischen Anomalie von Erbendorf (Oberpfalz) und dazugehörige gesteinsmagnetische Untersuchungen. - Geol. Jb., E 33, Hannover.

RAUEN, A., LIPPMANN, E., HUENGES, E., BÜCKER, Ch., WIENAND, J. & K.E. WOLTER (1988): Tiefbohrung KTB Oberpfalz VB, Ergebnisse der geowissenschaftlichen Bohrungsbearbeitung im KTB-Feldlabor (Windischeschenbach), Teufenbereich von 992 bis 1530 m: D. Geophysik.- KTB-Report 88-6: D1-D60, Hannover.

RYBACH, L. (1973): Wärmeproduktionsbestimmungen an Gesteinen der Schweizer Alpen.- Beitr. Geol. Schweiz, geotechn. Ser., 51: 43 pp.

RYBACH, L. (1976): Radioactive heat production, a physical property determined by the chemistry of rocks. In: R.G.J. Strens (ed.):"The Physics and Chemistry of Minerals and Rocks", Wiley & Sons, London.

SOFFEL, H.C. (1968): Die Beobachtung von Weiss'schen Bezirken auf einem Titanomagnetitkorn mit einem Durchmesser von 10 µ in einem Basalt.- Z. Geophys., 34: 175-181.

STROH, A., HEINSCHILD, H.J., HOMANN, K.D. & M.TAPFER (1988): Tiefbohrung KTB Oberpfalz VB, Ergebnisse der geowissenschaftlichen Bohrungsbearbeitung im KTB-Feldlabor (Windischeschenbach), Teufenbereich von 992 bis 1530 m: C. Geochemie.- KTB-Report 88-6: C1-C109, Hannover.

VAN SCHMUS, W. R. (1984): Radioactivity Properties of Minerals and Rocks. In: Carmichael, R.S. (ed), CRC Handbook of Physical Properties of Rocks, Vol. III, CRC Press, Boca Raton; Florida.

WESTMEIER, W. (1988): Progamm SODIGAM.- Ver. 2.11, Dr. Westmeier GmbH, Ges. f. Kernspektrometrie, 3557 Ebsdorfergrund-Mölln.

WIENAND, J., WOLTER, K.E., RAUEN, A., EIGNER, K.H. & Ch. BÜCKER (1988): Tiefbohrung KTB Oberpfalz VB, Ergebnisse der geowissenschaftlichen Bohrungsbearbeitung im KTB-Feldlabor, Teufenbereich 480-992 m: D.Geophysik. - KTB-Report 88-2: D1-D59, Hannover.

WOLTER, K.E., AULBACH, E. & H. BERCKHEMER (1988): Spannungsnachwirkungsuntersuchungen: Messung der Retardation und der akustischen Emission: D. Geophysik.- KTB-Report 88-6: D47-D60, Hannover.

WOLTER, K.E. & H. BERCKHEMER (1989): Time Dependent Strain Recovery of Cores from the KTB-Deep Drill Hole. - Rock Mech. and Rock Eng., (in press).